Actuator Disc Methods Applied to Wind Turbines

Mikkelsen, Robert Flemming

Publication date:
2004

Document Version
Publisher's PDF, also known as Version of record

MEK-FM-PHD 2003-02

Actuator Disc Methods Applied to Wind Turbines

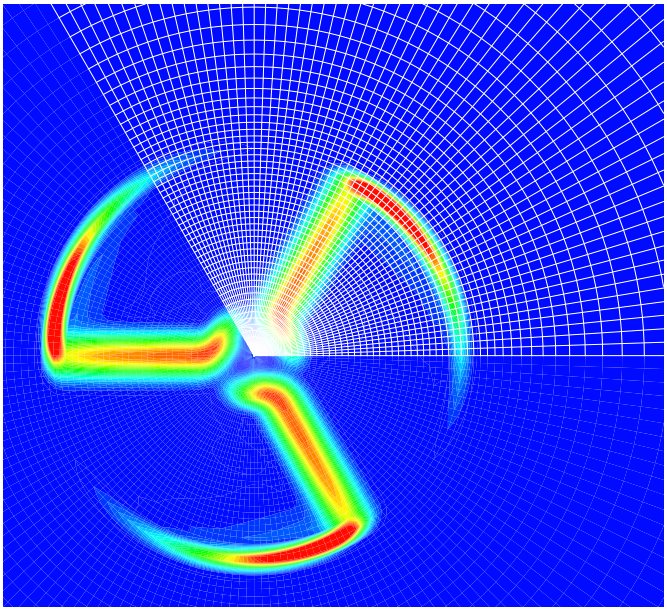

by

Robert Mikkelsen

Dissertation submitted to the Technical University of Denmark in partial fulfillment of the requirements for the degree of Doctor of Philosophy in Mechanical Engineering

Fluid Mechanics
Department of Mechanical Engineering
Technical University of Denmark
June, 2003

Fluid Mechanics
Department of Mechanical Engineering
Nils Koppels Allé, Building 403
Technical University of Denmark
DK-2800 Lyngby, Denmark

Printed in Denmark by DTU-Tryk, Lyngby

MEK-FM-PHD 2003-02 / ISBN 87-7475-296-0

This thesis has been typeset using LaTeX2e. Illustrations was drawn with XFIG, graphs were created with XMGR and MATLAB and field plots were produced using TecPlot and PostView.

Preface

This thesis is submitted in partial fulfillment of the requirements for the Ph.D. degree from the Technical University of Denmark (DTU). The research work was conducted during the period from August 1998 to April 2003 at the Department of Mechanical Engineering (MEK), Fluid Mechanics Section. I wish to express my sincere thanks to my supervisor Professor Jens Nørkær Sørensen for his ever encouraging support and for his advise and patience during our many discussions. I would also like to thank him for letting me pursue research on strange new ideas on alternative energy conversions concepts and for the fun hours during our weekly game of football.

I'd like to extend my warm thanks to Associated Professors Wen Zong Shen and Jess A. Michelsen (the Long Man) for many useful conversations and also to Associated Professor Stig Øye for valuable suggestions.

I also wish to thank my colleagues and fellow student at the section for providing a friendly environment with room for good humor and interesting discussion. Special thanks to Mac Gaunaa for the collaboration we had on wavelets, MPI, structural dynamics and fun toys.

Finally, I would thank my family and friends for their support and interest and to Laura for her love and support.

Lyngby, June 3, 2003

Robert Mikkelsen

Abstract

This thesis concerns the axisymmetric actuator disc model and its extension to a three dimensional actuator line technique which, combined with the incompressible Navier-Stokes equations, are applied to describe the aerodynamics of wind turbine rotors. The developed methods are used to investigate the aerodynamic behaviour of coned rotors, rotors exposed to yawed inflow and tunnel blockage. Miscellaneous investigations are conducted in order to analyze the consistence of some basic assumptions of the Blade Element Momentum (BEM) method, such as the influence of pressure on expanding streamtubes and the accuracy of tip correction theories. In the latter case an inverse formulation of the equations were applied.

Results for the coned rotor demonstrates that the Navier-Stokes methods, both the actuator disc and actuator line, captures the changed aerodynamic flow behaviour whereas a modified BEM method is incapable of handling flow through coned rotors. For rotors exposed to yawed inflow, the actuator disc method combined with appropriate sub models predicts structural loads with good accuracy. At high yaw angles the actuator line method capture observed effects from the root vortex, which axisymmetric methods is incapable of. Computations on rotors inserted into a tunnel show that the Navier-Stokes methods fully resolve the effects of tunnel blockage. A new solution to the inviscid axial momentum analysis on tunnel blockage by Glauert, is also presented. The new solution compares excellent with results presented for the equivalent free air speed obtained with the Navier-Stokes methods.

An analysis of pressure forces acting on expanding the streamtubes revealed that the influence of pressure forces is negligible for the velocities at the rotor disc. A new approach to solve the heavily loaded actuator disc is presented, using a new numerical technique based on solving the equations original formulated by Wu. The formulations is fast to run on computer, however, less accurate than Navier-Stokes computations. A new method for inverse determination of the tip-correction factor is believed to be correct, however, the obtained results reveal uncertainties which needs further investigations.

Dansk resumé

Den foreliggende afhandling omhandler den akse symmetriske aktuator disk og den fuldt tre-diminsionelle aktuator linie teknik kombineret med de inkompressible Navier-Stokes ligninger. De udviklede modeller er anvendt til at undersøge den aerodynamiske opførsel af rotorer udsat for koning, skæv anstrømning (yaw) og rotorer indsat i en vindtunnel. Der er foretaget særlige undersøgelser for kunne analysere validiteten af visse fundamentale antagelser for Blade Element Momentum (BEM) metoden, så som indflydelsen af trykkræfter på de ekspanderende strømrør og nøjactiheden af tip korrections teorier. I det sidste tilfælde er der anvendt en invers metode.

Resultater for den konede rotor viser, at Navier-Stokes metoderne, både aktuator disk og aktuator linie, kan håndtere det ændrede aerodynamiske flow, mens en modificeret BEM model ikke er istand til at håndtere flow gennem konede rotorer. For rotorer udsat for skæv anstrøning er aktuator disk modellen, kombineret med passende delmodeller, istand til at beregne structurelle laster med god nøjagtighed. For skæv anstrømning ved store vinkler (high yaw) fanger aktuator linie modellen målte effekter der hidrører fra rodhvirvlen, som akse-symmetriske modeller ikke kan vise. Beregninger på rotorer indsat i vindtunnel viser, at Navier-Stokes metoderne kan modellere blokerings effekter. En ny løsning til den inviskose aksiale momentum teori for tunnel blokering af Glauert, præsenteres også. Den nye løsning passer ekstremt godt med Navier-Stokes simuleringer for den equivalente hastighed i en fri strømning.

En analyse af trykkrafterne på de ekspanderede strømflader viser, at indflydelsen af tryk kræfter kan negligeres med hensyn til hastighederne gennem rotoren. En ny metode til undersøgelse til løsning af den hårdt belastede rotor er præsenteres, hvor den numeriske teknik er baseret på løsning af ligninger oprindeligt formuleret af Wu. Metoden er hurtig, men mindre nøjagtig sammelignet med Navier-Stokes modellen. En ny metode til invers bestemmelse af tip-korrektions faktoren menes at være korrekt, men de beregnede resultater afslører usikkerheder, der kræver videre undersøgelser.

List of Publications

Published in refereed journals

Mikkelsen R, Sørensen JN, Shen WZ. Modelling and analysis of the flow field around coned rotors. *Wind Energy*, 2001; **4**: 121–135.

Published in proceedings

Mikkelsen R, Sørensen JN. Yaw Analysis Using a Numerical Actuator Disc Model. Proc. 14th IEA Symp. on the *Aerodynamics of Wind Turbines*, Boulder, Col, USA, 2000; 53–59

Mikkelsen R, Sørensen JN, Shen WZ. Yaw Analysis Using a 3D Actuator Line Model. *European Wind Energy Conf.*, Copenhagen, Danmark, 2001; 478–480

Mikkelsen R, Sørensen JN. Modelling of Wind Tunnel Blockage. *Global Windpower Conf.*, Paris, France, 2002; –

Shen WZ, Mikkelsen R, Sørensen JN, Bak C. Evaluation of the Prandtl Tip Correction for Wind Turbine Computations. *Global Windpower Conf.*, Paris, France, 2002; –

Sørensen JN, Mikkelsen R. On the Validity of the Blade Element Momentum Method. *European Wind Energy Conf.*, Copenhagen, Danmark, 2001; 362–366

Contents

List of Symbols

Roman letters

a, a'	Interference factors	$[-]$
$A, \boldsymbol{A}$	Area / Coordinate matrix	$[m^2, -]$
B	Number of blades	$[-]$
c	Chord length	$[m]$
C	Tunnel area	$[m^2]$
C_T	Thrust coefficient	$[-]$
C_P	Power coefficient	$[-]$
$D, \boldsymbol{D}$	Drag force / damping matrix	$\left[\frac{N}{m}, -\right]$
$\boldsymbol{e}$	Unit vector	$[-]$
EI	Cross sectional blade stiffness	$[Nm^2]$
f	Areal loading	$\left[\frac{N}{m^2}\right]$
F	Loading / Prandtl tip loss factor	$\left[\frac{N}{m}, -\right]$
H	Pressure head/height(tower)	$\left[\frac{N}{m^2}, m\right]$
I, J	Indices	$[-]$
$K_{\theta,z}$	Relaxation parameter	$[-]$
$\boldsymbol{K}$	Stiffness matrix	$[-]$
L	Lift force, differential operator	$\left[\frac{N}{m}, -\right]$
m	Cross sectional blade mass	$\left[\frac{kg}{m}\right]$
$\dot{m}$	Mass Flow	$\left[\frac{kg}{s}\right]$
$M, \boldsymbol{M}$	Bending moment / mass matrix	$[Nm, -]$
N_b	Block size: $p2^n$	$[-]$
p, d	Distance	$[m]$
p	Pressure / structural loading	$\left[\frac{N}{m^2}, N\right]$
P	Power	$[W]$
q	Source	$\left[\frac{m^2}{s}\right]$
Q	Torque	$[Nm]$
r, θ, z	Polar coordinates	$[m, rad, m]$
R	Rotor radius	$[m]$
s, t, n	Spanwise, tangential, normal coordinates relative to blade	$[m, rad, m]$
S	Disc area	$[m^2]$
T	Thrust, shear force	$[N]$
$Tu.I$	Turbulent intensity	$[\%]$
u, V	Velocity	$\left[\frac{m}{s}\right]$
$v, \dot{v}, \ddot{v}$	Blade deflection, velocity and acceleration	$\left[m, \frac{m}{s}, \frac{m}{s^2}\right]$
W	Induced velocity	$\left[\frac{m}{s}\right]$
x, y, z	Cartesian coordinates	$[m]$
X	Stream surface pressure force	$[N]$

Greek letters

α, α_s	Area aspect ratio/wind shear exponent	$[-]$
β, B	Cone angle/matrix	$[^o]$
γ	Pitch angle	$[^o]$
Γ	Circulation	$\left[\frac{m^2}{s}\right]$
δ	Log decrement, structural damping	$[-]$
ε	Machine accuracy $\simeq 10^{-15}$	$[-]$
ϵ	Regularization parameter / error quantity	$[-]$
η	Regularization function	$[-]$
$\theta, \boldsymbol{\Theta}$	Azimuthal angle/matrix	$[^o]$
λ, λ_o	Local and global tip-speed ratio: $\frac{\Omega r}{V_o}, \frac{\Omega R}{V_o}$	$[-]$
ν	Kinematic viscosity	$\left[\frac{m^2}{s}\right]$

ξ	Structural pitch	$[^o]$
ζ	Interpolation ratio	$[^o]$
ρ	Mass density	$\left[\frac{kg}{m^3}\right]$
σ	Solidity/Area aspect ratio	$[-]$
τ	Dynamic time delay	$[-]$
ϕ	Flowangle	$[^o]$
$\phi_y, \boldsymbol{\Phi_y}$	Yaw angle / matrix	$[^o]$
$\phi_t, \boldsymbol{\Phi_t}$	Tilt angle / matrix	$[^o]$
ψ	Normal modes	$[-]$
Ψ	Stream function	$\left[\frac{m^3}{s}\right]$
ω	Vorticity / structural blade eigenfrequencies	$[s^{-1}]$
Ω	Angular rotor velocity	$\left[\frac{rad}{s}\right]$

Indices

$_{o,1}$	Free stream / far wake
$_{'}$	per volume
$_{a}$	Aerodynamic
$_{c}$	Cell center / centrifugal / convective
$_{d,}{}^{d}$	Disc / damping / diffusive
$_{f}$	Deflexion
$_{g}$	Gravity
$_{H}$	Head
$_{l}$	Linear
$_{B}$	i'th blade / actuator line
$_{p}$	Point on actuator line
$_{s}$	Stream surface
$_{t,}{}^{t}$	Tower
$_{w,}{}^{w}$	Wake
$_{\Psi}$	Stream line / stream function level
$_{acc}$	Acceleration
$_{hub}$	Hub
$_{ijkn}$	Indices
$_{kin}$	Kinetic
$_{r\theta z}$	Polar components
$_{rel}$	Relative
$_{rot}$	Rotational / rotor
$_{stn}$	Spanwise, tangential, normal components
$_{tun}$	Tunnel
$_{xyz}$	Cartesian components

Special numbers

CFL	Courant - Friedrichs - Lewy number, at center axis : $\frac{V_\theta \Delta t}{r \Delta \theta}$	$[-]$
Re	Reynolds number, Rotor: $\frac{V_o R}{\nu}$, Aerofoil: $\frac{V_o c}{\nu}$	$[-]$

Acronyms

2D,3D	Two or Three-Dimensional
AD	Actuator Disc
AL	Actuator Line
BEM	Blade Element Momentum method
CFD	Computational Fluid Dynamics
FVM	Finite Volume Method
MPI	Message Passing Interface for parallel computations
N-S	Navier-Stokes equations
$\Psi - \omega$	Stream function - swirl velocity - vorticity formulations of N-S equations

Chapter 1

Introduction

This thesis deals with numerical methods that combine the actuator disc and actuator line concept with the Navier-Stokes equations applied to wind turbine rotors.

The Development of Rotor Predictive Methods

Rotor predictive methods based on the actuator disc concept use the principle of representing rotors by equivalent forces distributed on a permeable disc of zero thickness in a flow domain. The concept was introduced by Froude [18] as a continuation of the work of Rankine [44] on momentum theory of propellers. Fundamental results were presented for the velocity at the disc position which equals one half of the sum of the upstream and far wake air speed. The analysis by Lanchester [31](1915) and Betz [3](1920) showed that the maximum extraction of energy possible from a turbine rotor is 16/27 or 59.3%, of the incoming kinetic energy. A major step forward in the modelling of flow through rotors came with the development of the generalized momentum theory and the introduction of the Blade Element Momentum BEM method by Glauert [19](1930). As the method is based on momentum balance equations for individual annular streamtubes passing through the rotor, it effectively enhance the information about spanwise distributions.

Although the BEM method is the only method used routinely by industry, a large variety of advanced rotor predictive methods have been developed. Generally, the methods can be categorized into inviscid models that demand the use of tabulated airfoil data, and viscous models based on either viscous-inviscid procedures or Navier-Stokes algorithms. The most widespread inviscid technique is the vortex wake method. In this method the shed vorticity in the wake is employed to compute the induced velocity field. The vorticity may either be distributed as vortex line elements (Miller [41], Simoes and Graham [50], Bareiss et al. [1]) or as discrete vortices (Voutsinas et al. [68]) with vortex distributions determined either as a prescribed wake or a free wake. A free wake analysis may in principle provide one with all relevant information needed to understand the physics of the wake. However, this method can be very computing costly and tends to diverge owing to intrinsic singularities of the vortex panels in the developing wake. Another inviscid method is the asymptotic acceleration potential method that was developed primarily for analyzing helicopter rotors by van Holten [66] and later adapted to cope with flows about wind turbines by van Bussel [65]. The method is based on solving a Poisson

equation for the pressure, assuming small perturbations of the mean flow. Compared to vortex wake models, the method is fast to run on a computer, but difficult to apply to general flow cases.

The generalized actuator disc method represent a straight-forward inviscid extension of the BEM technique. The main difference is that the annular independence of the BEM model is replaced by the solution of a full set of Euler or Navier-Stokes equations. Axisymmetric versions of the method have been developed and solved either by analytical / semi-analytical methods (Wu [71], Hough and Ordway [28], Greenberg, [22] and Conway [8], [9]) or by finite difference / finite volume methods (Sørensen and colleagues [55], [56], [58] and Madsen [32]). In helicopter aerodynamics a similar approach has been applied by e.g. Fejtek and Roberts [17] who solved the flow about a helicopter employing a chimera grid technique in which the rotor was modelled as an actuator disc, and Rajagopalan and Mathur [45] who modelled a helicopter rotor using time-averaged momentum source terms in the momentum equations. Whereas the finite difference / finite volume and Finite Element Method (FEM) methods, as formulated by Masson et al. [34] who solve the unsteady 3D flowfield around HAWT using FEM, facilitates natural unsteady wake development, the analytical / semi-analytical methods are generally solved for steady conditions. The actuator line concept introduced recently by Sørensen and Shen [61](2002) extends beyond the assumption of axial symmetry, where the loading is distributed along lines representing blade forces in a fully 3D flow domain. Such an approach facilitates analysis of the validity of the assumptions used in simpler methods and in general the 3D behaviour of the wake, which is part of the present investigation.

To avoid the problem of using corrected or calibrated airfoil data various viscous models have been developed to compute the full flow field about wind turbine rotors. Sørensen [54] used a quasi-simultaneous interaction technique to study the influence of rotation on the stall characteristics of a wind turbine rotor. Sankar and co-workers [2] developed a hybrid Navier-Stokes / full-potential / free wake method for predicting three-dimensional unsteady viscous flows over isolated helicopter rotors in hover and forward flight. The method has recently been extended to cope with horizontal axis wind turbines [72]. Another hybrid method is due to Hansen et al. [24] who combined a three-dimensional Navier-Stokes solver with an axisymmetric actuator disc model. Full three-dimensional computations employing the Reynolds-Averaged Navier-Stokes (RANS) equations have been carried out by e.g. Ekaterinaris [16], Duque et al. [15] and Sørensen and Michelsen [63]. Although the RANS methods are capable of capturing the pre-stall behaviour, because of inaccurate turbulence modelling and grid resolution, RANS methods still fail to capture correctly the stall behaviour.

Accuracy of Present Days Rotor Predictive Methods

Actuator disc methods have through the years proven their capability to match different types of rotor predictive methods. Rotor predictive methods are, however, no better than the foundations of the assumptions inherent or the input data supplied to them. This became clear with the NREL[1] blind code comparison, that was carried out December 2000. About 15 participants

[1]During the December 1999 through May 2000 the National Renewable Energy Laboratory, NREL, conducted thorough unsteady aerodynamic experiments on a 2 bladed (D=10m) Horizontal Axis Wind Turbine, HAWT, in the NASA Ames 24.4x36.6m wind tunnel.

from all over the world joined the comparison using various models ranging form simple Blade Element Momentum methods to full 3D Navier-Stokes formulations. Model predictions were compared at zero yaw and yawed operating conditions. Figure 1.1 depicts the participants prediction of the low speed shaft torque at zero yaw, where the line marked with diamonds represent measurements. The general results showed unexpected large margins of disagreement

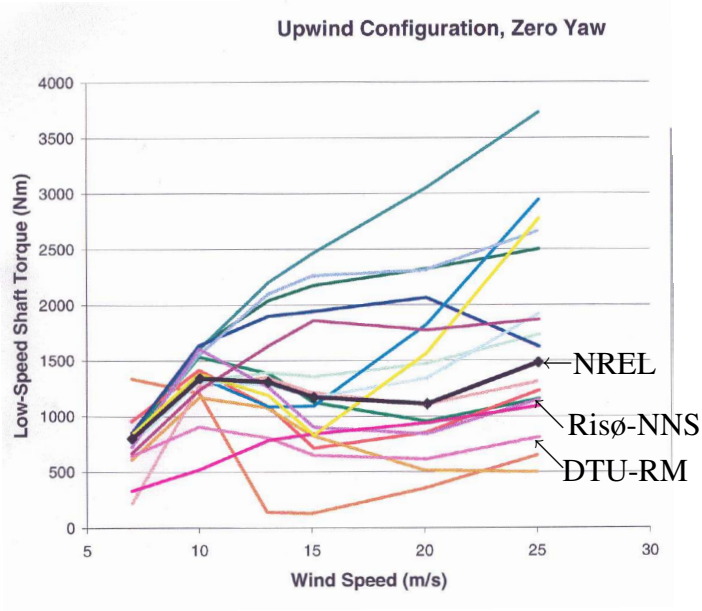

Figure 1.1: NREL experiments - blind code comparison. Predictions of low speed shaft torque, NREL: Black line with diamonds, DTU-RM: Pink, Risø-NNS: Violet

between predicted and measured data (Schreck [48]) and in addition no consistent trends were apparent regarding the magnitude or the directions of the deviations. The large discrepancies presented can only be referred to limitations in input data and insufficient modelling and model assumptions. Assumptions which apply to many used methods include axial symmetry, annular independence, empirical adjustments (tip-correction, Glauert correction), etc. Models which rely heavily on being able to tune input data, in order to accurately predict rotor performance, can only perform to the accuracy of the given data.

The prediction by Sørensen et al.[64] using the EllipSys3D RANS method combined with the $k-\omega$ SST turbulence model, which only use the blade geometry and inflow data as input, compared rather well for the low speed shaft torque. However, local predictions in the fully stall-separated regions clearly distinguished the EllipSys3D from all other codes. Turbulence modelling represent a key issue using these methods, since full DNS or LES simulations are far beyond present days computing capacity. Forced by computational limitations hybrid methods are emerging which mix conventional turbulence models with LES (see Johansen et al.[29]) referred to as Detached-Eddy Simulation or DES. Such methods include considerable more dynamics and three-dimensional flow behaviour like spanwise development of vortex structures. Although 3D Navier-Stokes methods has a promising future, computing cost will limit there influence for some time and give room for improvements of the simpler methods. Such necessary improvements of simpler methods, addressed recently by Sørensen et al.[57], range from better handling of coned rotors, rotors at high yaw angles, dynamic inflow, large tip-speed ratios,

etc., to fundamental issues like tip correction, influence of pressure forces on expanding stream-tubes, etc. The aim of this thesis is to analyze some of these aspects with respect to inherent assumptions connected to BEM methods and in general extend the capabilities of actuator disc and actuator line methods.

The Present Study

The present study deals with actuator disc methods of increasing complexity. Part A gives general description of the actuator disc principle and aerodynamic blade forces are introduced in chapter 2 together with the basic idea behind the Blade Element Momentum (BEM) method. In chapter 3 the generalized actuator disc is described followed by basic steady computations on a constant loaded rotor, and using aerofoil data from the LM19.1m blade.

Part B deal with certain applications of the generalized actuator disc method. The aerodynamic behaviour of wind turbines rotors subject to operational conditions, apart from the fundamental steady conditions previously presented, are investigated. First, the coned rotor with constant normal loading is analyzed. Next, the Tjæreborg wind turbine exposed to up and downstream coning is investigated. Rotors exposed to yawed inflow are analyzed using the axisymmetric actuator disc method combined with sub-models for tower, wind shear, dynamic stall and elastic deflection of each blade. In connection with experimental tests of turbine rotors, the effects of tunnel blockage is also investigated.

Part C present the actuator line technique combined with the full three-dimensional Navier-Stokes equation using the EllipSys3D general purpose flow solver. The method extends beyond axial symmetry and results are presented for corresponding configurations as for the generalized actuator disc.

Part D discuss miscellaneous topics connected to actuator disc methods. The heavily loaded actuator disc is approached by a new numerical technique using the equation derived by Wu and the validity of certain basic assumptions employed in most engineering models is tested by analyzing the influence of pressure forces acting on the expanding stream surfaces. The last chapter is devoted to an evaluation of tip correction theories, approached with an inverse technique combined with the actuator line method.

Part A

Actuator Disc Modelling

Chapter 2

Basic Rotor Aerodynamics

A basic description of the actuator disc concept, is presented in this section along with the axisymmetric flowfield and forces related to rotor aerodynamics of wind turbines.

2.1 The Actuator Disc Principle

The function of a wind turbine rotor is to extract the kinetic energy of the incoming flowfield by reducing the velocity abaft the rotor. Inevitably, a thrust in the direction of the incoming flowfield is produced with a magnitude directly related to the change in kinetic energy. With the rotational movement and the frictional drag of the blades, the flowfield is furthermore imparted by a torque which contributes to the change in kinetic energy. Thus, the flowfield and forces related to operating wind turbine rotors are governed by the balance between the thrust and torque on the rotor and the kinetic energy of the incoming flowfield. The behaviour of a wind turbine rotor in a flowfield may conveniently be analyzed by introducing the actuator disc principle. The basic idea of the actuator disc principle in connection with rotor aerodynamic calculations, is to replace the real rotor with a permeable disc of equivalent area where the forces from the blades are distributed on the circular disc. The distributed forces on the actuator disc alters the local velocities through the disc and in general the entire flowfield around the rotor disc. Hence, the balance between the applied forces and the changed flowfield is governed by the mass conservation law and the balance of momenta, which for a real rotor is given by the axial and tangential momentum equations. Figure 2.1 displays an actuator disc where the expanding streamlines are due to the reaction from the thrust. The classical Rankine-Froude theory considers the balance of axial-momentum far up- and downstream the rotor for a uniformly loaded actuator disc without rotation, where the thrust T and kinetic power P_{kin} in terms of the free stream V_o and far wake velocity u_1 reduces to

$$T = \dot{m}(V_o - u_1) \ , \quad P_{kin} = \tfrac{1}{2}\dot{m}(V_o^2 - u_1^2). \tag{2.1}$$

Here the mass flow through the disc is given as $\dot{m} = \rho u_1 A_1$, where A_1 is the far wake area given by the limiting streamline through the edge of the disc and ρ is the density. Using mass conservation through the disc gives that $uA = u_1 A_1$, and combining the above relations yields that the power extracted from the flowfield by the thrust equals

$$P_{kin} = \tfrac{1}{2}(V_o + u_1)T = uT \quad \Rightarrow \quad u = \tfrac{1}{2}(V_o + u_1), \tag{2.2}$$

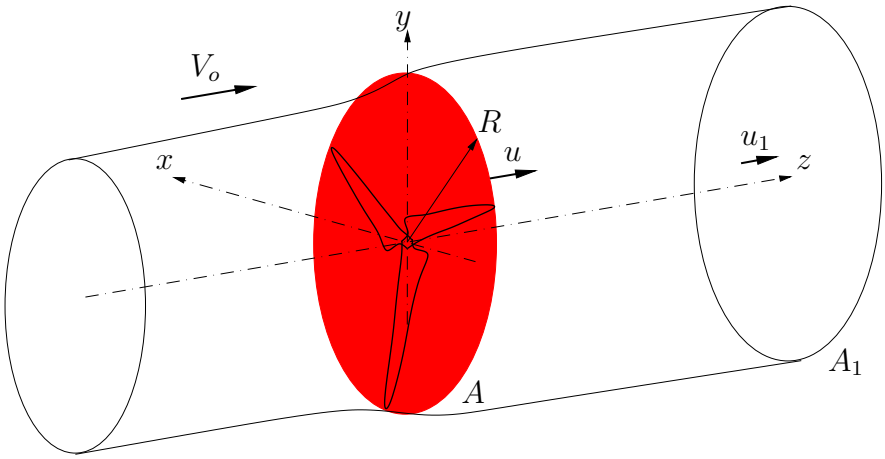

Figure 2.1: Flowfield around an actuator disc.

showing that the velocity at the disc u is the arithmetic mean of the freestream V_o and the slipstream velocity u_1. The importance of this result is seen with the evaluation of the aerodynamic blade forces. For convenience Eq.(2.1) is usually presented in non-dimensional form by introducing the axial interference factor $a = 1 - \frac{u}{V_o}$ and using the free stream dynamic pressure and rotor area. Thus, the non-dimensional thrust and power coefficients $C_T, C_{P_{kin}}$ are established as

$$C_T = \frac{\rho u A(V_o - u_1)}{\frac{1}{2}\rho V_o^2 A} = 4a(1-a), \tag{2.3}$$

$$C_{P_{kin}} = \frac{\frac{1}{2}\rho u A(V_o^2 - u_1^2)}{\frac{1}{2}\rho V_o^3 A} = 4a(1-a)^2, \tag{2.4}$$

where $u_1 = V_o(1-2a)$. The optimal conversion of energy possible is easily found from the gradient $\frac{d}{da}(C_{P_{kin}})$ of Eq.(2.4), hence, the highest output is obtained for $a = \frac{1}{3}$ for a thrust coefficient of $C_T = \frac{8}{9}$. The power coefficient $C_{P_{kin}}$ attains the maximum value of 16/27 or 59.3% usually referred to as the Betz limit.

2.1.1 Annular Streamtubes - The Blade Element Momentum method

A real rotor, however, is never uniformly loaded as assumed by the Rankine-Froude actuator disc model, and in order to analyze the radial load variation along the blades, the flowfield is subsequently divided into radially independent annular streamtubes in the classical Blade Element Momentum, (BEM) method by Glauert [19]. Figure 2.2 displays such an annular division into streamtubes passing through the rotor disc. That the annual streamtubes are independent is one the basic assumption for the classical BEM method. Other assumption, discussed in detail later, which apply to BEM methods are the lack of pressure forces on the control volume, discussed in chapter 10 and that the flow may be considered axisymmetric. Assuming that Eqs.(2.1)-(2.2) is valid for each individual streamtube, the induced velocity $W_z = V_o - u$ is introduced in the rotor plane, by which the balance of axial momentum for each annular streamtube equals

$$\Delta T = 2W_z \Delta \dot{m} \ , \tag{2.5}$$

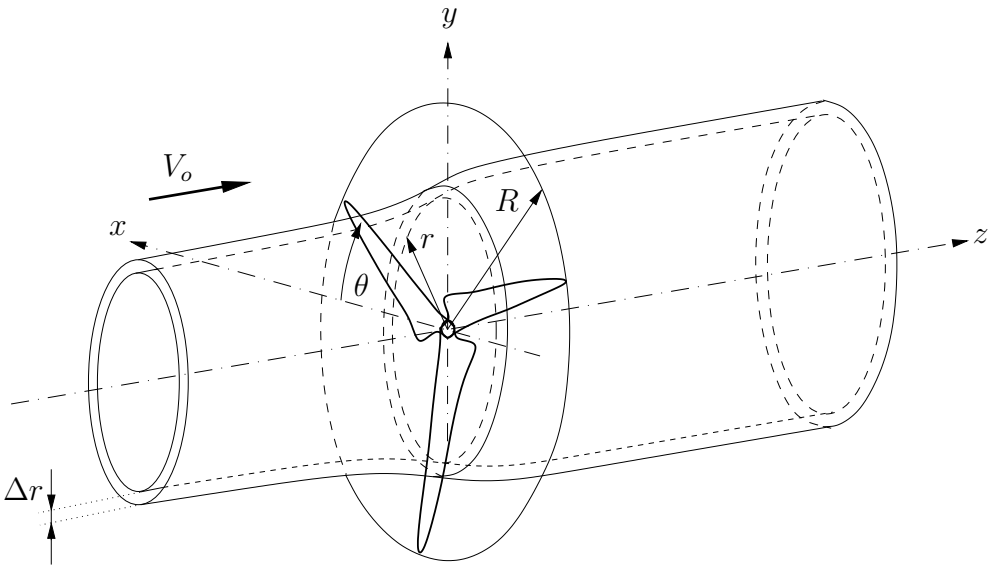

Figure 2.2: Streamtube through a three bladed rotor.

where $\Delta\dot{m} = \rho(V_o - W_z)\Delta A$. Correspondingly the angular momentum balance in terms of the induced angular velocity W_θ is given by

$$\Delta Q = 2W_\theta r \Delta\dot{m}, \tag{2.6}$$

where ΔQ is the resulting torque on each element. Although W_θ is zero infront of the disc, the angular velocity on the disc equals $-W_\theta$ and just after the disc $-2W_\theta$. In the wake the angular velocity along each streamsurface is preserved as $rW_\theta = r_s W_{\theta s}$ where r_s is the streamsurface radii.

2.1.2 Aerodynamic Blade Forces

The momentum changes given by the two previous equations are balanced with aerodynamic forces on the blades which may be analyzed by considering an unfolded streamsurface at a given radial position. A cascade of aerofoil elements emerges on the surface where each aerofoil element appears as in figure 2.3. The figure shows a cross-sectional aerofoil element at radius r in the (θ, z) plane. The aerodynamic forces acting on the rotor are governed by the local velocities and determined with the use of 2-D aerofoil characteristics. The relative velocity to the aerofoil element is determined from the velocity triangle as $V_{rel}^2 = (V_o - W_z)^2 + (\Omega r + W_\theta)^2$, where Ω is the angular velocity and the flowangle, ϕ, between V_{rel} and the rotor plane, is given by

$$\phi = \tan^{-1}\left(\frac{V_o - W_z}{\Omega r + W_\theta}\right). \tag{2.7}$$

Locally the angle of attack is given by $\alpha = \phi - \gamma$, where γ is the local pitch angle. Lift and drag forces per spanwise length are found from tabulated airfoil data as

$$(\boldsymbol{L}, \boldsymbol{D}) = \tfrac{1}{2}\rho V_{rel}^2 cB\left(C_L \boldsymbol{e}_L,\ C_D \boldsymbol{e}_D\right), \tag{2.8}$$

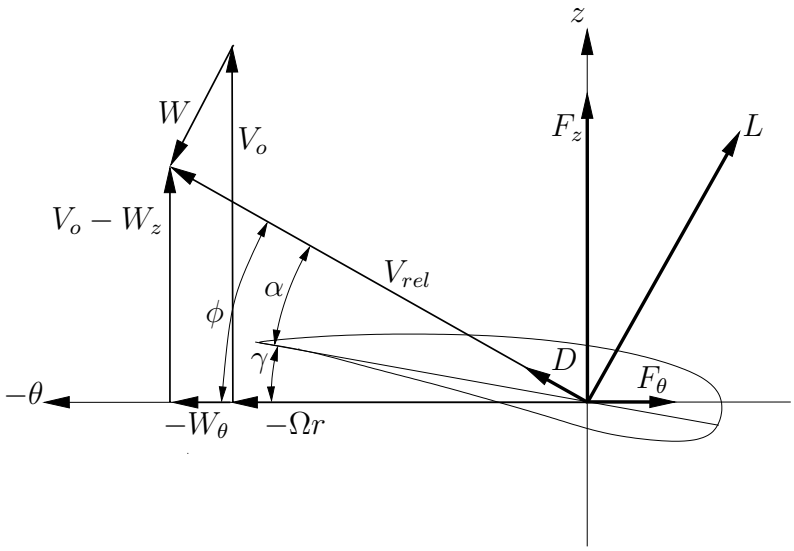

Figure 2.3: Cross-sectional airfoil element showing velocity and force vectors

where $C_L(\alpha, \mathrm{Re})$ and $C_D(\alpha, \mathrm{Re})$ are the lift and drag coefficients, respectively, and Re is the Reynolds number based on relative velocity and chord length. The directions of lift and drag are governed by the unit vectors $\boldsymbol{e}_L$ and $\boldsymbol{e}_D$, respectively, B denotes the number of blades and c is the chord length. The force per span wise unit length is written as the vector sum $\boldsymbol{F} = \boldsymbol{L} + \boldsymbol{D}$. Projection in the axial and the tangential direction to the rotor gives the force components

$$F_z = L\cos\phi + D\sin\phi\ , \quad F_\theta = L\sin\phi - D\cos\phi\ . \tag{2.9}$$

These are the blade forces which balance the momentum changes in the axial and tangential directions, respectively. Thus,

$$\Delta T = F_z \Delta r\ , \quad \Delta Q = F_\theta r \Delta r, \tag{2.10}$$

and by equating with Eqs.(2.5)-(2.6) relations for the "standard" BEM method are established from which the induced velocities and blade forces may be found using an iterative solution procedure. The division of the flow domain into annular streamtubes effectively enhances the knowledge about the spanwise load variation on the blades. The BEM method, however, rely on inherent assumptions which include axial symmetry, inviscid flow, annular division into radially independent streamtubes, the influence of pressure forces on expanding streamtubes is negligible, the induced velocity on the disc equals one half the induced velocity in the far wake and conservation of circulation can be ignored. Some of these assumptions are overcome with the more advanced methods and will be addressed in the proceeding chapters with the introduction of the generalized actuator disc and actuator line methods.

Chapter 3

The Generalized Actuator Disc Model

The generalized actuator disc model is based on solving the Euler or Navier-Stokes equation. Axisymmetric versions have been developed and solved with analytical/semi-analytical methods (Wu [71], Hough and Ordway [28], Greenberg, [22] and Conway [8], [9]) or using finite difference/finite volume methods (Sørensen and colleagues [55], [56], [58] and Madsen [32]). Here the finite difference method by Sørensen and Myken [55] of the generalized actuator disc is presented.

3.1 The $\Psi - \omega$ Formulation of the Navier-Stokes Equations

The present formulation of the generalized actuator disc was originally developed by Sørensen and Myken [55] and further refined by Sørensen and co-workers. The method (referred to as the $(\Psi - \omega)$ method) is based on the actuator disc concept combined with a finite difference discretization of the incompressible, axisymmetric Navier-Stokes equations. The equations are formulated in vorticity-swirl velocity-stream function $(\omega - V_\theta - \Psi)$ variables. The loading of the rotor is represented by body forces, $\boldsymbol{f'} = (f'_r, f'_\theta, f'_z)$. Due to axial symmetry, the calculation domain is restricted to a (r, z)-plane with $(r, z) \in [0 : L_r, 0 : L_z]$. Here (L_r, L_z) are the outer domain limits and the disc is placed at $z = z_d$. The stream function is introduced as

$$V_r = -\frac{1}{r}\frac{\partial \Psi}{\partial z}\,, \quad V_z = \frac{1}{r}\frac{\partial \Psi}{\partial r}, \tag{3.1}$$

which satisfies the continuity equation $\boldsymbol{\nabla} \cdot \boldsymbol{V} = 0$ identically. Transport of vorticity and swirl velocity are formulated through the two equations

$$\frac{\partial \omega}{\partial t} + \frac{\partial}{\partial r}(V_r \omega) + \frac{\partial}{\partial z}(V_z \omega) - \frac{\partial}{\partial z}\left(\frac{V_\theta^2}{r}\right) = \frac{\partial f'_r}{\partial z} - \frac{\partial f'_z}{\partial r} + \frac{1}{\mathrm{Re}}\left[\frac{\partial}{\partial r}\left(\frac{1}{r}\frac{\partial r\omega}{\partial r}\right) + \frac{\partial^2 \omega}{\partial z^2}\right], \tag{3.2}$$

$$\frac{\partial V_\theta}{\partial t} + \frac{\partial}{\partial r}(V_r V_\theta) + \frac{\partial}{\partial z}(V_z V_\theta) + \frac{2 V_r V_\theta}{r} = f'_\theta + \frac{1}{\mathrm{Re}}\left[\frac{\partial}{\partial r}\left(\frac{1}{r}\frac{\partial r V_\theta}{\partial r}\right) + \frac{\partial^2 V_\theta}{\partial z^2}\right], \tag{3.3}$$

where the equations are put into non-dimensional form by R and V_o, hence an effective Reynolds number [58] is defined as Re=$V_o R/\nu$. It is important to note that the Reynolds number is introduced only to stabilize the solution without significantly changing it. Previous investigations by Sørensen et al. [56, 58] showed that the Reynolds number only displays a limited influence on the solution, provided that it assumes a certain minimum value. The influence of

the Reynolds number will be analyzed later. The velocity field in the (r, z)-plane is determined through a Poisson equation for the stream function

$$\frac{\partial^2 \Psi}{\partial r^2} - \frac{1}{r}\frac{\partial \Psi}{\partial r} + \frac{\partial^2 \Psi}{\partial z^2} = -r\omega, \tag{3.4}$$

where $\omega = \boldsymbol{e}_\theta \cdot \boldsymbol{\nabla} \times V = \frac{\partial V_r}{\partial z} - \frac{\partial V_z}{\partial r}$ is the azimuthal component of the vorticity vector. A detailed deduction of the governing equations for the actuator disc is given in Appendix A. The boundary conditions for the calculation domain are defined on the four boundaries (See Sørensen and Kock [56]). Here the case with a turbine in an infinite domain is considered and summarized as

- At the axis of symmetry, r=0, the radial derivative of the axial velocity is zero and all other variables vanish i.e.

$$V_r = V_\theta = \Psi = \omega = 0\,, \;\; \frac{\partial V_z}{\partial r} = 0 \;\; \Rightarrow \;\; \frac{\partial^2 \Psi}{\partial r^2} - \frac{1}{r}\frac{\partial \Psi}{\partial r} = 0. \tag{3.5}$$

- The axial inflow is assumed uniform on the inlet boundary and all other variables equal zero,

$$V_r = V_\theta = \omega = 0\,, \;\; V_z = V_o \;\; \Rightarrow \;\; \Psi = \frac{V_o r^2}{2}. \tag{3.6}$$

- At the outlet boundary the wake behind the rotor and the generated swirl and vorticity is convected out, thus

$$\frac{\partial V_\theta}{\partial z} = 0\,, \;\; \frac{\partial \omega}{\partial t} + V_z \frac{\partial \omega}{\partial z} = 0\,, \;\; \frac{\partial V_r}{\partial z} = 0 \;\; \Rightarrow \;\; \frac{\partial^2 \Psi}{\partial z^2} = 0. \tag{3.7}$$

- The lateral boundary governs the condition for the infinite domain, hence, allowing expansion across the boundary. Thus

$$V_\theta = \omega = \frac{\partial V_z}{\partial r} = 0\,, \;\; \frac{\partial r V_r}{\partial r} = 0 \;\; \Rightarrow \;\; \frac{\partial \Psi}{\partial r} = 0. \tag{3.8}$$

In order to apply forces from the rotor an annular area of differential size is considered, $dA = 2\pi r dr$. Then the loading is given by

$$\boldsymbol{f} = \frac{\boldsymbol{F}(r)dr}{2\pi r dr}\,, \quad \boldsymbol{f'} = \frac{\boldsymbol{f}}{dz}, \tag{3.9}$$

where the force components of $\boldsymbol{F}$ are determined from Eqs.(2.7)- (2.9). The generalized actuator disc solves the entire axisymmetric flowfield and as such the induced velocity is naturally included into the formulation i.e. the relative velocity and flowangle are determined from

$$\phi = \tan^{-1}\left(\frac{V_z}{\Omega r - V_\theta}\right)\,, \quad V_{rel}^2 = V_z^2 + (\Omega r - V_\theta)^2, \tag{3.10}$$

where $V_z = V_o - W_z$ and $V_\theta = -W_\theta$ are measured on the disc. The interference factors a and a' may conveniently be introduced as

$$a = 1 - \frac{V_z}{V_o} = \frac{W_z}{V_o}\,, \quad a' = \frac{-V_\theta}{\Omega r} = \frac{W_\theta}{\Omega r}. \tag{3.11}$$

The main resemblance between the blade element momentum method and the generalized actuator disc is the determination of the aerodynamic forces but for the generalized actuator disc they are based on measured local velocities.

3.1.1 Numerical Implementation

The equations are solved on a staggered grid, in which the vorticity and swirl velocity are defined at the cell center and the stream function at vertices. The Poisson equation is discretized on a non-uniform grid using a second order central difference scheme and solved with the Alternating-Direction-Implicit (ADI) technique of Wachspress [69]. The Poisson equation is solved for the perturbation stream function ψ by introducing

$$\Psi(r,z) = \Psi_o(r) + \psi(r,z), \tag{3.12}$$

where $\Psi_o(r) = \frac{1}{2}r^2$. As the flow is dominated by the axial flow component, a fast solution is obtained by parabolizing the two transport equations. This is done by marching in axial direction, hence solving for each radial plane, using an implicit line solver with a second order upwinding scheme for convective terms and central difference schemes for the remaining terms. Figure 3.1 depicts the calculation domain with a schematic figure of the three point second order upwinding scheme used for the convective terms. The time integration is carried out

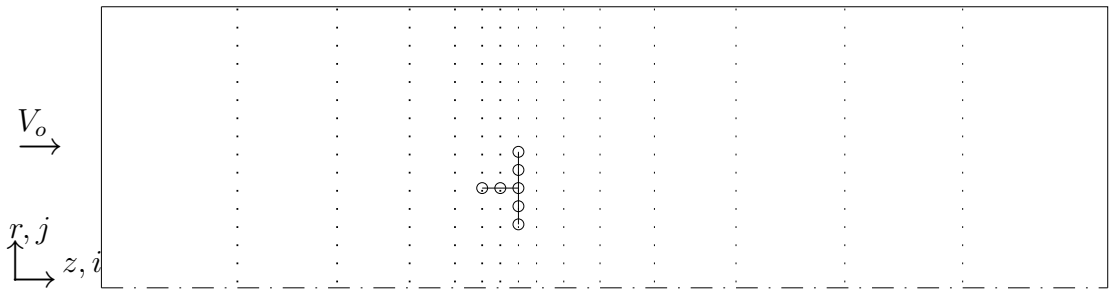

Figure 3.1: Calculation domain, three point second order upwinding scheme.

with a Crank-Nicolson type scheme for the convective and diffusive terms and with an explicit Adams-Bashfort extrapolation of the velocities V_r, V_z. Letting L_c and L_d be the convective and diffusive differential operator, respectively, the two transport equations (3.2) and (3.3) may be written in discretized form as (with $f'_r = 0$)

$$\omega_{ij}^{n+1} + \tfrac{1}{2}\Delta t[L_c - L_d](\omega_{ij}^{n+1}) = \omega_{ij}^{n} - \Delta t \frac{\Delta f'_z}{\Delta r}\bigg|_{ij}^{n+1/2} + \tfrac{1}{2}\Delta t[L_d - L_c](\omega_{ij}^{n}), \tag{3.13}$$

$$V_{\theta ij}^{n+1} + \tfrac{1}{2}\Delta t[L_c - L_d](V_{\theta ij}^{n+1}) = V_{\theta ij}^{n} + \Delta t f'^{n+1/2}_{\theta ij} + \tfrac{1}{2}\Delta t[L_d - L_c](V_{\theta ij}^{n}), \tag{3.14}$$

where $t^{n+1} = t^n + \Delta t$ and the aerodynamic forces are based on the velocity field $\boldsymbol{V}^{n+1/2}$. The forces are modelled as cell-centered sources evaluated using a second order central difference approximation, and applied at a single column in the computational domain defining the actuator disc. As with the evaluation of the aerodynamic forces, the convective operator L_c uses $\boldsymbol{V}^{n+1/2}$ to convect the vorticity and swirl velocity. Thus, the two transport equations are solved in a time true manner. As the method possess excellent stability properties, steady solution may be obtained relatively fast since large time steps can be performed. The limitations of the implementation is given by the thrust level since the wake region is bound to separate for values above $C_T \sim 1$, hence, violating the assumption that the flow may be parabolized. The limit is partly dependent on the Reynolds number Re which is investigated later.

3.2 The Constant Loaded Rotor Disc

The constant loaded rotor disc represents an ideal test case since an exact one-dimensional solution exist. It is moreover a challenge for many advanced numerical methods, since the edge of the disc is singular. From the initially presented axial momentum theory in the previous chapter, the relation between the thrust coefficient and axial interference factor $a = \frac{W_z}{V_o}$ equals $C_T = 4a(1-a)$, where the kinetic power coefficient is given by $C_{Pkin} = 4a(1-a)^2$. Hence, the highest output is obtained for $a = \frac{1}{3}$ at a thrust coefficient of $C_T = \frac{8}{9}$. The geometry of actual rotors don't enter the generalized actuator disc formulation, only equivalent forces and therefore the method is validated against the constant loaded rotor disc at various thrust levels and at the optimal condition of Betz.

3.2.1 Numerical Results

Figure 3.2 displays a part of the numerical solution using a domain extending 10 rotor radii upstream, 20 radii downstream and 10 radii in the radial direction. The rotor is resolved with 81 equidistantly distributed grid points where the total amount of grid points is 241 and 161 in the radial and axial directions, respectively. On the left figure, tip vorticity is shed downstream from the edge of the disc, and to the right the expanding streamlines through the rotor are displayed. The thrust coefficient is set to $C_T = 1.0$ and the effect of diffusion is seen en terms of a slight radial smearing of the vorticity. The Reynolds number is set to Re=5000

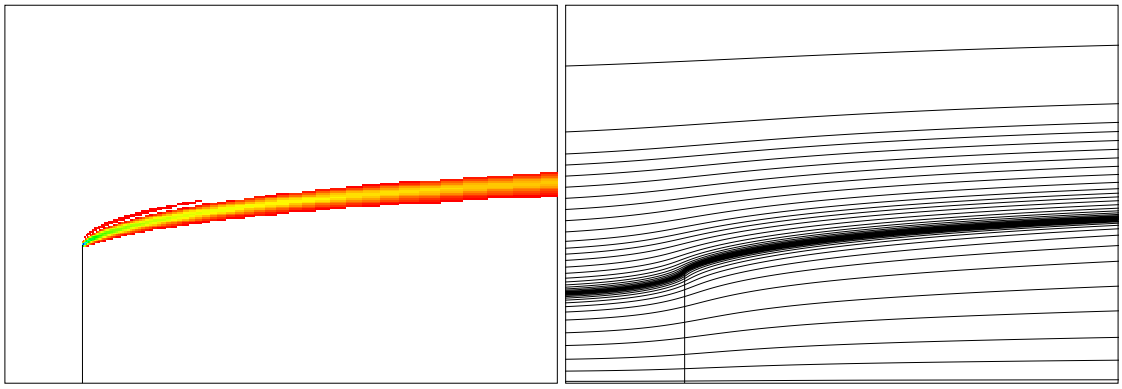

Figure 3.2: Tip-vorticity (left) and streamlines (right) for a constantly loaded rotor disc, $C_T = 1.0$. The disc is inferred as a straight line

in the above simulations. The general behaviour of the flowfield with increasing thrust level is a corresponding increased expansion of the wake region. Increasing the thrust level above $C_T \simeq 1$ results in a change in the flow regime towards an unsteady wake region. The transition to unsteady flow is mainly governed by the thrust level and the Reynolds number. Steady and unsteady solutions may be obtained for C_T values between 0.89-1.15 by lowering the Reynolds number from about 50.000 to 100. For much higher C_T values, separated regions emerges in the wake. Looking at the axial development of the different quantities, figure 3.3(left) displays the total head H, static pressure normalized with the pressure jump (see App.A.5) and V_z along the center axis for the constant loaded rotor. Furthermore the radius of the limiting streamline through the tip r_Ψ/R together with the radial velocity along the streamline is shown. Figure 3.3(right) displays the corresponding axial development along a streamline ($\Psi_{r=0.7R}$ on disc)

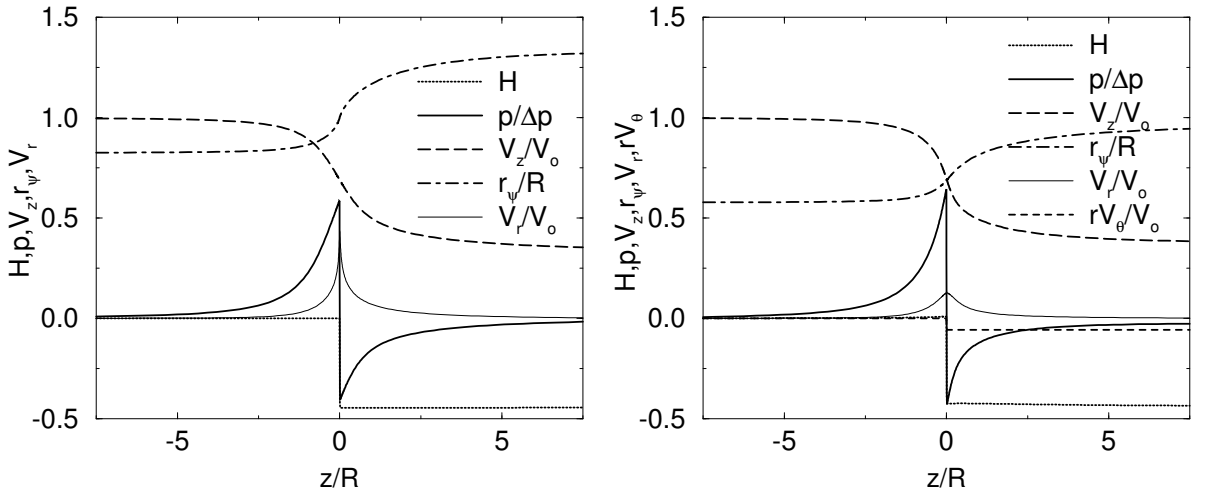

Figure 3.3: Axial development of the head, static pressure, axial velocity, limiting streamline radii and radial velocity for C_T=0.89(left). Correspondingly, axial development along a streamline ($\Psi_{r=0.7R}$ on disc) for a real rotor (right) including tangential velocity.

for a real rotor including the tangential velocity, which is presented in section 3.3. In terms of the axial induction along the rotor disc for the constant loaded rotor, figure 3.4 (left) depicts the interference factor a for the thrust levels C_T=0.4, 0.8, 0.89 and 1.0. The trends compare well

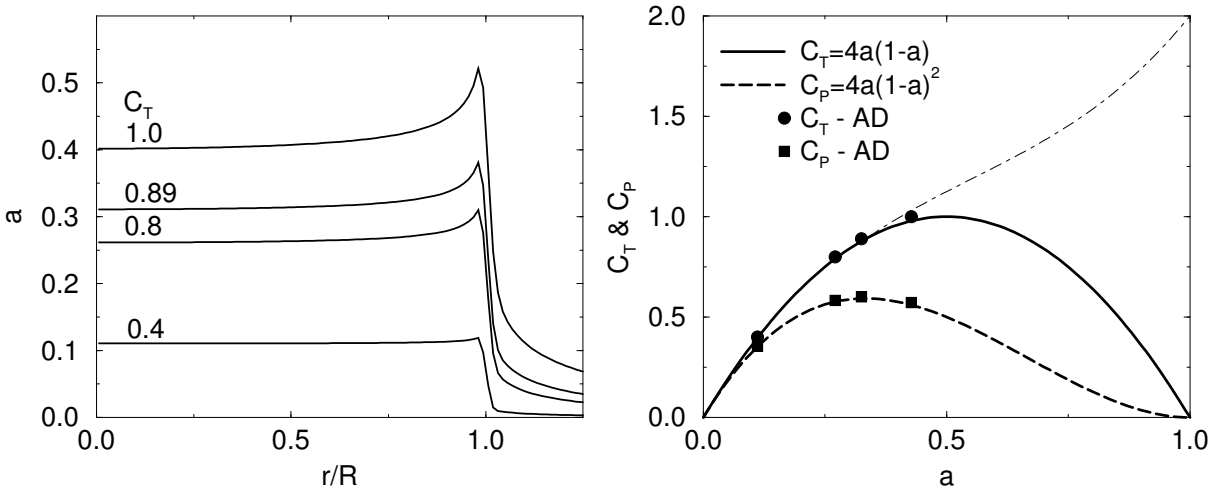

Figure 3.4: Axial flow interference factor $a(r)$ along the disc (left) and thrust and power coefficients $C_T(a), C_P(a)$ (right) for thrust levels C_T=0.4, 0.8, 0.89 and 1.0.

with the findings by Madsen [32] and Sørensen et al.[58] although the integrated a-level for $C_T = 1.0$ was found to about a=0.39 in [58] and here is determined to about a=0.43. Figure 3.4 (right) shows the integrated quantities $C_T(a), C_P(a)$ (see Appendix C) compared with one-dimensional momentum theory. Inferred with a thin line is the Glauert empirical correlation for higher C_T-values. The results compare extremely well with one-dimensional momentum theory up C_T=0.89, but for $C_T = 1.0$ the trend deviates towards experimental observations quantified with the Glauert empirical correlation.

3.2.2 Grid Sensitivity

To further validate the numerical algorithm the influence of grid density and Reynolds number, Re, has been analyzed for an actuator disc with a constant loading, C_T=0.89. The outcome is shown in figure 3.5 that depicts the power coefficient C_P (see Appendix C) as a function of Re for 4 different grids. First, it is important to note that the final solution always will exhibit an

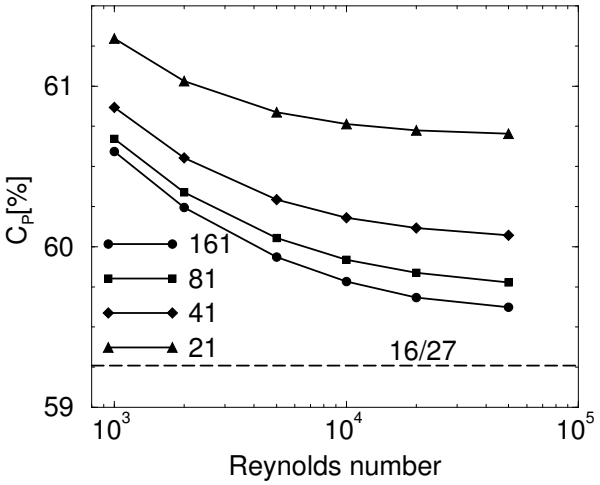

Figure 3.5: The influence of Reynolds number and grid size on C_P for C_T=0.89. The rotor is resolved by 21, 41, 81 and 161 grid points, respectively, for grids (A), (B), (C) and (D)

influence of grid size and Re, but what is important from a grid sensitivity study is to quantify the error committed. Next, it shall be emphasized that the flow in principle is inviscid, but, in order to stabilize the solution, diffusive terms are retained. Thus, since vorticity is only produced in the plane of the rotor disc, with the forces acting on the rotor computed from airfoil data, the actual value of the Reynolds number is not important. It is known from flows past bluff bodies that the drag coefficient and the essential flow behaviour do not depend on the Reynolds number, provided that it has reached a certain minimum value. This is illustrated in figure 3.5 where it is shown that a change in Reynolds number from 1,000 to 50,000 results in a change in C_P of about 1% point. To capture the gradients of the flowfield, grid points are concentrated at the rotor and stretched in the radial and axial direction. In the grid sensitivity study, the following four grids are considered, (A) 61x41, (B) 121x81, (C) 241x161 and (D) 481x321 points in $r - z$ direction, respectively. The rotor itself is represented by 1/3 of the radial points and the number of grid points is doubled in each direction when going from one grid level to the next. From figure 3.5 the dependency of the grid is found to decay exponentially. By extrapolation in Re and grid size, an estimated Re- and grid-independent solution results in a C_P-value of 59.5% which is about 0.2% point higher than the Betz limit.

3.3 Simulation on Real Rotors - Tip Correction

Real rotors, in contrast to the axially loaded rotor, includes angular velocities. Furthermore, real rotors have finite number of blades which produce a system of distinct tip vorticity structures in the wake. Thus, a different vortex wake is produced by a rotor with infinite number of blades as compared with one with a finite number of blades. Prandtl [43] derived a formula for the tip-correction, quantified by the factor F, in order to compensate for the finite number of blades. In order to include tip-correction effects with the generalized actuator disc model, the aerodynamic force components given by Eqs.(2.8)-(2.9) are corrected using the Prandtl tip-correction factor F given by the formula

$$F = \frac{2}{\pi}\cos^{-1}\left[\exp\left(-\frac{B}{2}\frac{R-r}{r\sin\phi}\right)\right]. \tag{3.15}$$

For the Navier-Stokes methods a different approach is needed as compared to BEM methods when applying the Prandtl tip correction formula. In the BEM method [19], the tip correction is employed to the axial and angular momentum equations, leading to two equations for a and a'

$$\frac{a}{1-a} = \frac{\sigma C_n}{4\sin^2\phi} = \frac{F\tilde{a}}{1-\tilde{a}}\,, \quad \frac{a'}{1+a'} = \frac{\sigma C_\theta}{4\sin\phi\cos\phi} = \frac{F\tilde{a}'}{1+\tilde{a}'}, \tag{3.16}$$

where $\tilde{a}$ and $\tilde{a}'$ are corrected interference factors and F is the tip loss factor. With a BEM method a and a' (or $\tilde{a}$ and $\tilde{a}'$) are found directly from Eq.(3.16), but with a Navier-Stokes model the flowfield is given and the loading has to be modified, hence Eq.(3.16) is rearranged to

$$\tilde{a} = \frac{a}{F(1-a)+a}\,, \quad \tilde{a}' = \frac{a'}{F(1+a')-a'}, \tag{3.17}$$

where F serves as a relaxation parameter in the iterative solution process. With these values a corrected set of $\tilde{V}_z$ and $\tilde{V}_\theta$ are determined from Eq.(3.11). The modified loading is then determined through the corrected values for $\tilde{\phi}$, $\tilde{V}_{rel}$, $\tilde{L}$ and $\tilde{D}$ found from Eqs.(2.7) and (2.8).

3.3.1 Computation using LM 19.1m Blade Data

In order to display the capabilities of the generalized actuator disc model on real rotors, the Nordtank NTK 500/41 stall regulated wind turbine with LM 19.1m blades is analyzed. The blade sections consist of NACA 63-4xx aerofoils in the outer half of the blade and FFA-W3-xxx aerofoils at the inner part of the blade. The aerofoil characteristics (Hansen [26]) are corrected for 3-D effects by preserving values within the measuring range and in post stall and deep stall applying a smooth and somewhat experienced guess, combined with data tuning in order to get the measured power curve using a "standard" BEM method. The turbine has three blades, a diameter of 41m and it rotates at 27.1 rpm. Applying the (C)-grid and a Reynolds number of Re=5000, figure 3.6 (left) shows the axial interference at two different wind speeds, 7 m/s and 10 m/s. The computations predicts an increasing axial induction towards the tip at both wind speeds, with a level at 7 m/s that indicates a reasonable high thrust coefficient. Corresponding calculation without the Prandtl tip-correction i.e. $F = 1$, shows that the influence of the tip-correction may be neglected for the LM 19.1m blade. This behaviour is explained with the

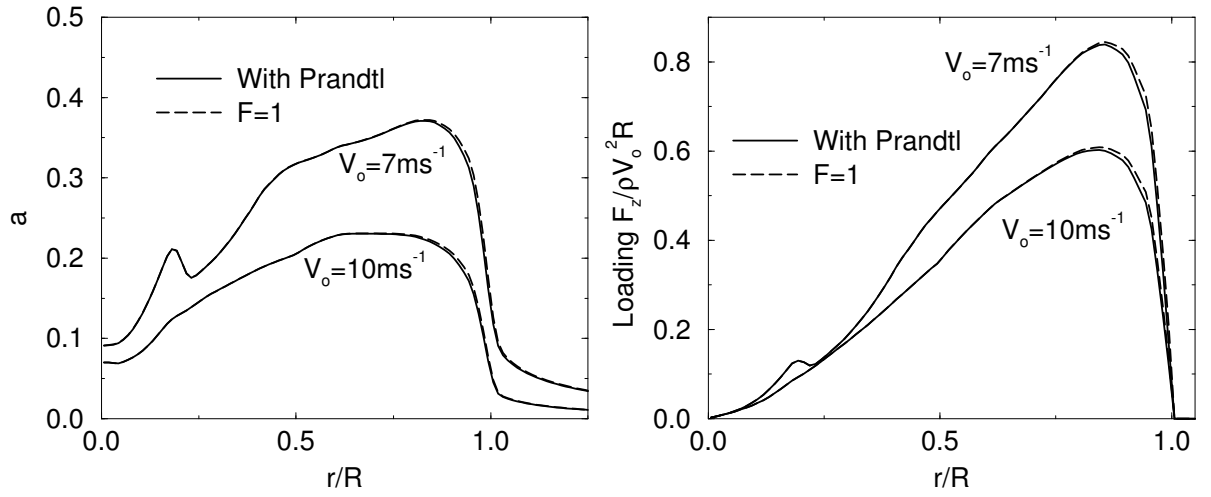

Figure 3.6: Distribution of axial interference (left) and non-dimensional loading (right) for the LM 19.1m blade at 7m/s and 10m/s.

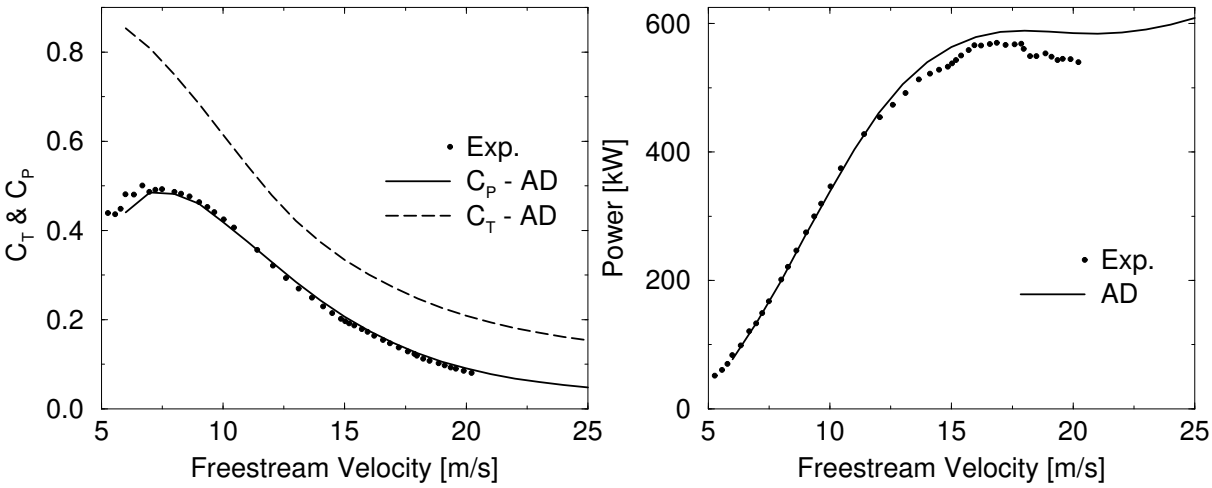

Figure 3.7: C_T, C_P (left) and power distribution (right) for the Nordtank NTK 500/41 wind turbine with LM 19.1m blades.

chord distribution for the blade which decreases continuously all the way to the tip, thereby including a "natural" decay in loading towards the tip. Looking at the non-dimensional loading, figure 3.6 (right) shows corresponding tendencies in the tip region, to that obtained for the induced velocities. Letting the freestream velocity vary from 5 to 25 m/s results in the C_T, C_P and power distribution presented in figure 3.7. The power curve, measured by Poulsen at Risø [42], is seen to compare within an accuracy of 1-3% through the velocity range, although at higher velocities > 18m/s an increased deviation is observed. Thus, the steady computations compares well with the experimental measurements. At very low wind speeds the thrust coefficient increases rapidly thereby approaching the unsteady regime. Looking at the convergence rate depicted in figure 3.8 the trend is towards less iterations with increasing wind speed i.e. decreasing thrust-coefficient. At 6m/s the converged solution gives a $C_T = 0.86$ using a non-dimensional time step of 0.1, which may be increased to 0.25 at 9m/s and 0.6 at 12m/s. The magnitude of the non-dimensional time step govern the stability of the convergence and the maximum value for obtaining steady converged solutions, mainly depends on the thrust coefficient i.e $\Delta t_{max} = \Delta t(C_T)$. The maximum values of Δt_{max} are found more or less arbitrarily.

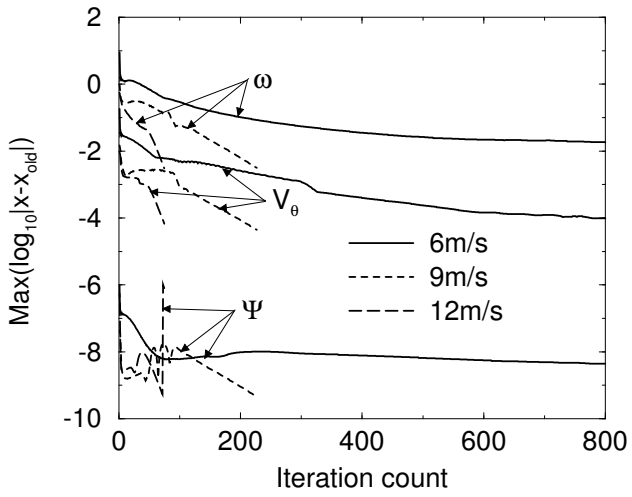

Figure 3.8: Numerical convergence of the vorticity, swirl-velocity and stream function at three different wind speeds.

To summarize, the calculations on the axially loaded rotor and a real rotor using data for the Nordtank 500/41 wind turbine have demonstrated that a good accuracy may be obtained by solving the Navier-Stokes equations. The steady solutions are found efficiently with good convergence rate using large time steps.

Part B

Application of the Generalized Actuator Disc Model

Chapter 4

The Coned Rotor

This part presents topics beyond the standard steady computations for wind turbine rotors performed with the generalized actuator disc. First, the coned rotor is analyzed and next the unsteady behaviour of the yawed rotor is approached with new contribution. Finally, in connection with experimental investigations effects of tunnel blockage is analyzed.

4.1 Coned Rotors

The trend in the development of modern wind turbines tends towards larger and more structural flexible rotor blades. As a consequence, large blade deflections are anticipated and as a first step in the understanding of the aerodynamics of rotors subject to large blade deflections, the influence of coning is investigated. When considering rotors with substantial coning or blade deflections, the radial flow component has an influence on the loading and induced velocities. For upstream coning the expansion of streamlines tends to make the flow orthogonal to the rotor, whereas the opposite happens for downstream coning. This results in different performance characteristics for the two cases. As the standard BEM method (Glauert [19]) does not predict the radial flow component this difference is difficult to incorporate into a BEM method. Madsen and Rasmussen [33] investigated the induction from a constantly loaded actuator disc with downstream coning and large blade deflection using a numerical actuator disc model. Here the $(\Psi-\omega)$ formulation, as well as a modified BEM method, is used to analyze a rotor with constant normal loading and a real rotor exposed to up- and downstream coning.

4.1.1 Geometry and Kinematics - Velocity Triangle

Considering a coned rotor in a polar coordinate system (r, θ, z), the axisymmetric flowfield around the turbine is described by the velocity components $\boldsymbol{V} = (V_r, V_\theta, V_z)$. In figure 4.1 a rotor is sketched in the (r, z)-plane at a coning angle β. A local coordinate system, (s, n), is applied, where s is the spanwise coordinate and n is the direction normal to the blade. With the full flowfield given, the velocity components normal to the rotor are (V_n, V_θ), where V_n is determined as

$$V_n = V_z \cos\beta + V_r \sin\beta, \tag{4.1}$$

and both V_z and V_r are known from the numerical actuator disc computation. The BEM model, however, is not capable of handling the radial flow component. As it is based on momentum

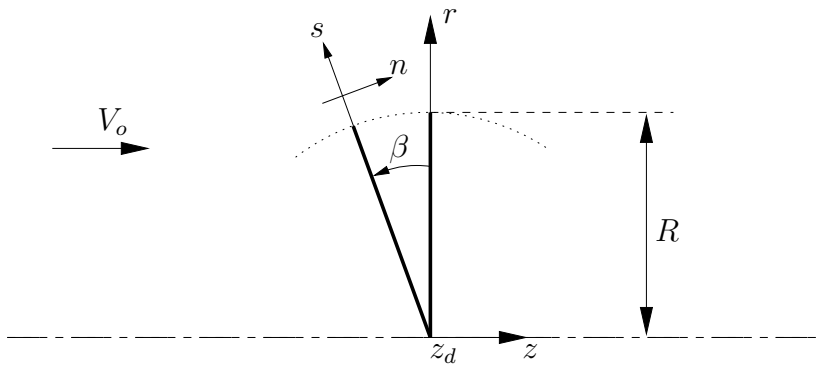

Figure 4.1: Rotor with coning angle β

considerations far upstream and downstream of the rotor, it does not contain any information about the radial flow component on the rotor. Figure 4.2 shows the local velocity triangle of a coned rotor in the (s, z)-plane. Letting W_n denote the induced velocity in the direction normal

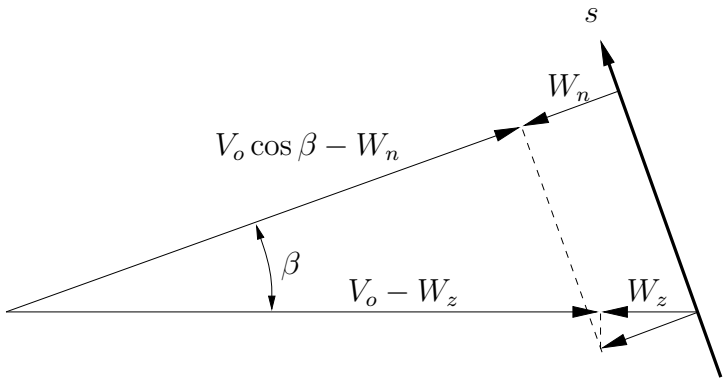

Figure 4.2: Velocity triangle in the (s, z)-plane

to the rotor from the BEM method, the normal velocity is given by

$$V_n = V_o \cos\beta - W_n, \tag{4.2}$$

which only contains the first term in Eq.(4.1). The corresponding axial velocity component acting on the rotor is equal to $V_o - W_n \cos\beta$. An important limitation of neglecting the radial influence is that a distinction between up- and down-stream coning is not possible.

4.1.2 Blade Forces

The aerodynamic lift and drag forces acting on the coned rotor are determined from Eq.(2.8), however, the local velocity triangle is somewhat altered by the cone angle. Figure 4.3 shows the equivalent cross-sectional airfoil element presented in figure 2.3 for the coned rotor at radius s in the (θ, n) plane. The relative velocity is determined from $V_{rel}^2 = V_n^2 + (\Omega s \cos\beta - V_\theta)^2$, where Ω is the angular velocity and the angle, ϕ, between V_{rel} and the rotor plane, is given as

$$\phi = \tan^{-1}\left(\frac{V_n}{\Omega s \cos\beta - V_\theta}\right). \tag{4.3}$$

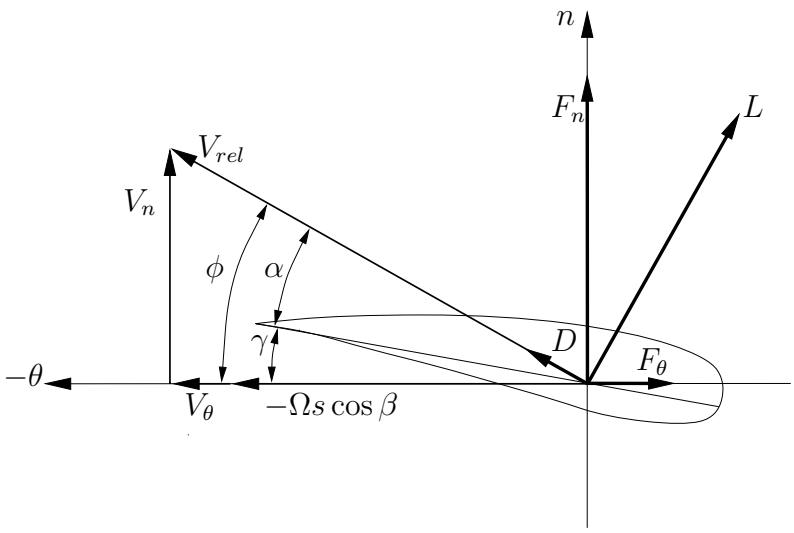

Figure 4.3: Cross-sectional airfoil element showing velocity and force vectors

As seen from Eqs. (4.1) and (4.3), when the rotor is coned, V_r contributes to the relative velocity and alters the angle of attack. Projection of the lift and drag forces given by Eq.(2.8) in the normal and the tangential direction to the rotor gives the force components

$$F_n = L\cos\phi + D\sin\phi\ , \quad F_\theta = L\sin\phi - D\cos\phi\ . \tag{4.4}$$

The normal force is decomposed into axial and radial direction as

$$F_z = F_n\cos\beta\ , \quad F_r = F_n\sin\beta. \tag{4.5}$$

4.2 Aerodynamic Modelling - Momentum Balance

The aerodynamic behavior of coned rotors is investigated using two different models. To check the utility of employing the BEM technique for rotors subject to coning, the consequences of modelling coned rotors is analyzed using simple momentum consideration, hence, neglecting the radial flow component. Next, the generalized actuator disc is employed where considerations for the applied forces are presented.

4.2.1 A Modified BEM Method

The classical BEM method by Glauert [19] presented in section (2.1.1) considers the axial and tangential balance of momenta for a number of individual annular stream tubes passing through the rotor from $-\infty$ to $+\infty$. Here the analysis is extended to include effects of coning. Considering the coned rotor on figure 4.2, the local normal thrust, ΔT_n, and torque, ΔQ, acting on a blade element, are equal to the change in normal and angular momentum, respectively. It is, however, still a purely axial momentum balance which govern the momentum for the coned rotor. Denoting the induced velocities in the rotor plane by W_n, W_θ the normal thrust and torque reads

$$\Delta T_n\cos\beta = 2W_n\cos\beta\Delta\dot{m}\ , \quad \Delta Q = 2W_\theta\Delta\dot{m}s\cos\beta, \tag{4.6}$$

where $\cos\beta$ is included on both sides of the first equation in order to emphasize the axial projection. The equation is immediately reduced to $\Delta T_n = 2W_n\Delta\dot{m}$, but as the induced velocity in the far wake has a purely axial direction and not normal to the rotor plane, presenting the reduced equation could be misleading with respect to the far wake boundary. Furthermore, the induced velocity in the tangential direction, W_θ, is equal to $-V_\theta$. Considering the axial induced velocity, $W_z = W_n\cos\beta$, the mass flow through each element is given by,

$$\Delta\dot{m} = \rho(V_o - W_n\cos\beta)2\pi s\Delta s\cos^2\beta, \tag{4.7}$$

where the tip radius is constant and the projected area is reduced with $\cos^2\beta$. In terms of induced velocities, interference factors are introduced for the normal, axial and tangential direction, respectively, as

$$a_n = \frac{W_n}{V_o\cos\beta}\,, \quad a_z = \frac{W_z}{V_o}\,, \quad a' = \frac{W_\theta}{\Omega s\cos\beta}. \tag{4.8}$$

Combining Eqs. (4.6) and (4.7), and normalizing the thrust with the projected area (see Appendix C), gives the axial thrust coefficient $C_T = 4a_z(1-a_z)$, which is the same as for the straight rotor. This shows that the axial induction along the blade only depends on the thrust and is independent of the radial position or coning angle. The relation between a_n and a_z is found to

$$a_n = \frac{a_z}{\cos^2\beta}. \tag{4.9}$$

The normal and tangential forces generated by the blades give a normal thrust and torque from each element that is equal to

$$\Delta T_n = F_n\Delta s\,, \quad \Delta Q = F_\theta s\Delta s\cos\beta, \tag{4.10}$$

where F_n and F_θ are given by Eq.(4.4). Tip correction F is included by using the Prandtl tip loss factor as described in [19] and given by

$$F = \frac{2}{\pi}\cos^{-1}\left[\exp\left(-\frac{B}{2}\frac{R-r}{r\sin\phi}\right)\right]. \tag{4.11}$$

In order to handle high values of a the empirical Glauert correction given by Spera [53] is applied

$$C_T = \begin{cases} 4a_z(1-a_z)F & a_z \le a_c, \\ 4[a_c^2 + (1-2a_c)a_z]F & a_z > a_c, \end{cases} \tag{4.12}$$

where $a_c = 0.2$ (which seems low). By equating Eqs.(4.6) and (4.10), with V_{rel} and ϕ given by Eq.(4.3) and introducing $\sigma = cB/2\pi s\cos\beta$, the induced velocities are found from the expressions

$$4W_z(V_o - W_z)F = V_{rel}^2\sigma C_n\,, \tag{4.13}$$

$$4W_\theta(V_o - W_z)F\cos\beta = V_{rel}^2\sigma C_t\,, \tag{4.14}$$

where C_n, C_t are the normal and tangential projection of the lift and drag coefficient, respectively

$$C_n = C_L\cos\phi + C_D\sin\phi\,, \quad C_t = C_L\sin\phi - C_D\cos\phi\,. \tag{4.15}$$

In terms of interference factors a, a', Eqs.(4.13)-(4.14) are normalized and rewritten as follows

$$4a_z(1-a_z)F = \frac{V_{rel}^2 \sigma C_n}{V_o^2} \Rightarrow a_z = \frac{1}{2}\left(1 - \sqrt{\frac{V_{rel}^2 \sigma C_n}{V_o^2 F}}\right),\ a_z \leq a_c, \tag{4.16}$$

$$4[a_c^2 + (1-2a_c)a_z]F = \frac{V_{rel}^2 \sigma C_n}{V_o^2} \Rightarrow a_z = \left(\frac{V_{rel}^2 \sigma C_n}{4V_o^2 F} - a_c^2\right)\frac{1}{1-2a_c},\ a_z > a_c, \tag{4.17}$$

$$a' = \frac{V_{rel}^2 \sigma C_t}{V_o^2 \cos^2\beta}\frac{1}{4(1-a_z)F}\frac{V_o}{\Omega s}. \tag{4.18}$$

In the BEM method the equations are solved iteratively and the procedure is summarized in the following steps: Initial values : $a = a' = 0$ or $W_z = W_\theta = 0$,

- Find ϕ from Eq.(4.3)
- Angle of attack, $\alpha = \phi - \gamma$
- Relative velocity, $V_{rel}^2 = (V_o - W_n)^2 + (\Omega s \cos\beta + W_\theta)^2$
- Normal and tangential coefficients C_n, C_t from table and projection, Eq.(4.15)
- The induced velocities W_z, W_θ or interference factors a, a' from Eqs.(4.13-4.14) or Eqs.(4.16-4.18)

The sequence is repeated until a, a' or W_z, W_θ fulfill some convergency criteria.

4.2.2 The Actuator Disc Model - Applying Forces

The $(\Psi - \omega)$ formulation presented previously is a sufficient formulation for capturing the true axisymmetric behaviour of the flow through coned rotors. However, the applied forces in the formulation needs some special considerations in order to cope coned rotors. The rest of the formulation as well as the computational domain used to evaluate the flowfield around coned rotors, is preserved from the previous sections. In order to apply forces from a coned rotor, a coned annular area of differential size is considered, $dA_n = 2\pi s \cos\beta ds$. Then the loading is given by

$$\boldsymbol{f} = \frac{\boldsymbol{F}(s)ds}{2\pi s \cos\beta ds}, \quad \boldsymbol{f'} = \frac{\boldsymbol{f}}{dz}. \tag{4.19}$$

The resulting body force, $\boldsymbol{f}'_\epsilon$, is then formed by taking the convolution of the computed load, $\boldsymbol{f}'$, and a regularization kernel, η_ϵ, as shown below

$$\boldsymbol{f}'_\epsilon = \boldsymbol{f}' \otimes \eta_\epsilon, \quad \eta_\epsilon(p) = \frac{1}{\epsilon^3 \pi^{3/2}} \exp\left[-(p/\epsilon)^2\right]. \tag{4.20}$$

Here ϵ is a constant that serves to adjust the concentration of the regularized load and p is the distance between the measured point and the initial force points on the actuator disc. In the case of a coned rotor, the regularized force becomes

$$\boldsymbol{f}'_\epsilon(r,z) = \int_0^R \int_0^{2\pi} \frac{\boldsymbol{F}(s)}{2\pi\epsilon^3\pi^{3/2}} \exp\left[-(p/\epsilon)^2\right] d\theta ds. \tag{4.21}$$

The parameter ϵ is here set equal to $\epsilon = \epsilon_i \Delta z$ where ϵ_i is of the order $1 \lesssim \epsilon_i \lesssim 4$ and Δz is the cell size in axial direction. Eq.(4.21) may be integrated in the θ-direction and reduced[1] to

$$\boldsymbol{f}'_\epsilon(r,z) = \int_0^R \frac{\boldsymbol{F}(s)}{\epsilon^3 \pi^{3/2}} \exp\left(-\frac{d^2 + 2rs\sin\beta}{\epsilon^2}\right) I_o\left(\frac{2rs\sin\beta}{\epsilon^2}\right) ds. \tag{4.22}$$

The distance $d^2 = (r - s\cos\beta)^2 + [(z - z_d) + s\sin\beta]^2$ is the distance between the measured point and the initial force points in the axisymmetric plane and I_o is the modified Bessel function of the first kind of order 0. The approach ensures that the integrated loading is conserved and that singular behavior is avoided as the loading is distributed smoothly on several mesh points in a 3D Gaussian manner away from each point on the disc. As the actuator disc appears as a one-dimensional line in the axisymmetric plane, suggest that a 1D Gaussian approach also may be applied to smear the forces away from the line. Hence, the forces are proposed to be distributed or smeared in the normal direction away from the rotor disc using the convolution

$$\boldsymbol{f}'_\epsilon = \boldsymbol{f}' \otimes \eta_\epsilon^{1D}, \quad \eta_\epsilon^{1D}(p) = \frac{1}{\epsilon\sqrt{\pi}} \exp\left[-(p/\epsilon)^2\right]. \tag{4.23}$$

Inserting gives the distributed force

$$\boldsymbol{f}'_\epsilon(r,z) = \int_{-\infty}^{+\infty} \frac{\boldsymbol{f}'(s)}{\epsilon\sqrt{\pi}} \exp\left[-(p/\epsilon)^2\right] dn. \tag{4.24}$$

The normal distance p between any point in the (r,z) plane and the rotor disc is given by

$$p = \frac{(z_d - z) - r\tan\beta}{\sqrt{1 + \tan^2\beta}}, \tag{4.25}$$

and the point on the rotor disc s_p which is normal to the field point (r,z) is determined as

$$s_p = \frac{r + p\sin\beta}{\cos\beta}. \tag{4.26}$$

The function of the smearing proposed by the two methods, is basically to distribute loading along any line on a regular mesh. Furthermore, the smearing prevents spatial oscillations in the vicinity of the applied forces, although it should be noted that solutions without oscillations have been obtained by not using smearing for the straight rotor. As pointed out by Masson et al.[34] who applied forces as pressure discontinuities, explicit treatment of the applied forces is needed to prevent spatial oscillations in the vicinity of the applied forces. Whereas the curl operator is applied to the $(\Psi - \omega)$ formulation, methods formulated in primitive variables depend on accurate handling of the divergence operator applied to the body force vector when solving the pressure equation. The oscillations or wiggles observed by Sørensen and Kock [56] on the axial interference factor are completely removed with the regularization and with suitable choice of grid resolution. The two distribution methods both apply as smearing function, however, the 3D Gaussian tends to smear beyond the edge of the disc whereby the intended spanwise load distribution near the tip, is slightly chanced.

4.3 Numerical Results for the Coned Rotor

To give an impression of the computational domain and the structure of the grid, a part of the grid is shown in figure 4.4. In the figure, a rotor coned -20^o is inferred as a straight

[1] In [37] Eq.(20) should be corrected with $\sin\beta$ instead of $\cos\beta$.

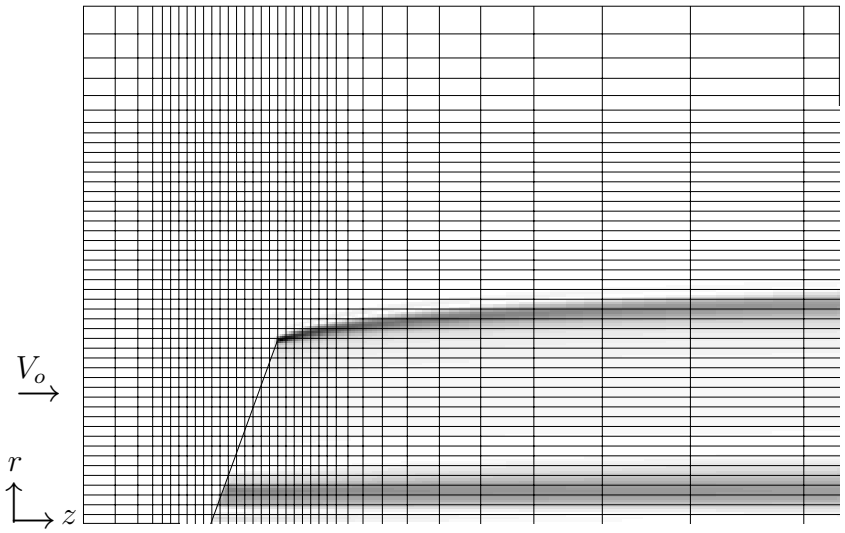

Figure 4.4: Vorticity contours and grid (only every fourth grid line is shown), $\beta = -20^o$. The vorticity is produced in the plane of the rotor and shed downstream

line. The flow enters from left and azimuthal vorticity, produced along the actuator disc and shed downstream, is shown as iso-contours. The smearing functions η_ϵ and η_ϵ^{1D} both preserve the applied loading, however, with increasing ϵ_i the 3D smearing function produces smooth solutions in the tip region, beyond what is desired from a smearing. Similar tendencies were found in [58] and the effect is readily explained as an effect of the radial smearing which alters the original span wise load distribution. The 1D approach is less sensitive to the higher values of ϵ_i and for $\epsilon_i < 1.5$ the two methods give nearly the same distribution. The smearing function will be discussed in further details with the introduction of the actuator line method. Returning to the obtained solution the normal, axial and tangential flow interference factors are defined as, respectively,

$$a_n = 1 - \frac{V_n}{V_o \cos\beta}\,, \quad a_z = 1 - \frac{V_z}{V_o}\,, \quad a' = \frac{-V_\theta}{\Omega s \cos\beta}, \tag{4.27}$$

measured along the actuator disc using a linear interpolation scheme.

4.3.1 The Constant Loaded Rotor

In figure 4.5 normal and axial interference factors are plotted for the constant loading of C_T=0.89 at cone angles 0^o,-20^o and 20^o. For a coned actuator disc with constant normal loading, the BEM model degenerates to a 1-dimensional momentum balance, resulting in constant a_n and a_z values along the disc. However, comparing computed full field results for the coned rotor with results for a straight rotor shows that coning introduces considerable changes along the blade axis. For positive coning, both a_n and a_z are higher at the center axis, gradually decreasing towards the tip. For negative coning the opposite is seen, albeit with a higher a_n near the tip. Similar tendencies are found by Madsen and Rasmussen [33], but with higher levels. When considering the axial induction in the z-constant plane through the tip, displayed in figure 4.6 (left), approximately the same distribution is found, hence, C_P based on the projected area is basically the same for all three cases. This behavior is readily explained by considering the

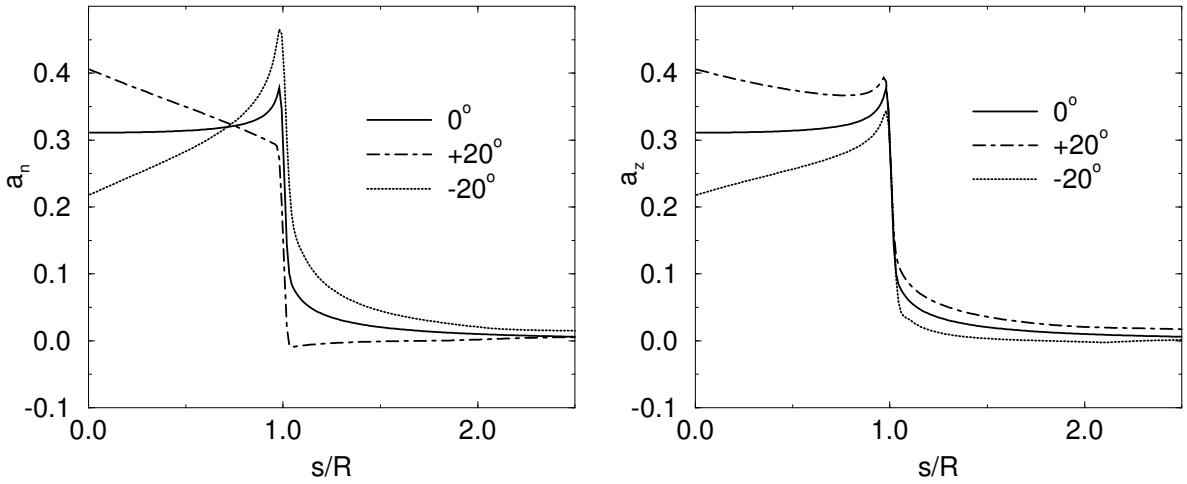

Figure 4.5: Normal and axial interference factors along the radius of the disc for C_T=0.89

body forces in Eq.(3.2). These appear as vorticity sources given by the general expression

$$\boldsymbol{\nabla} \times \boldsymbol{f'} \cdot \boldsymbol{e}_\theta = \frac{\partial f'_s}{\partial n} - \frac{\partial f'_n}{\partial s} = -\frac{\partial f'_n}{\partial s}, \tag{4.28}$$

since $f'_s = 0$ for any rotor. From this expression it is seen that finite source terms only appear at positions where the normal loading is varied. For a rotor with constant normal loading, the source term is zero everywhere except at the edge (or tip) of the actuator disc. Furthermore, the value of the source term depends only on the magnitude of the normal loading and not on the shape of the rotor. Whether the rotor is coned or not, the same source term at the edge of the disc and therefore the same system of trailing vortices, measured from the location of the source term. Schmidt and Sparenberg [52] derived the same result, by considering the pressure field divided into active regions. The induced velocities on the disc are, however, no longer the same as the position of the rotor with respect to the trailing vortex system has changed. With the BEM model in mind this suggests that the axial induction found by the BEM model is not located along the blade but in the plane through the tip. For comparison the level found in Ref. [33], also shown figure 4.6, is seen to be about 5% higher. The radial velocity along the disc, shown in figure 4.6 (right), is virtually unaffected by changes in cone angle, although a small effect is seen near the tip. The power coefficients are presented in Table 4.1 for the three cases and should ideally be exactly the same. There are, however, small variations within 0.3% point, which is attributed to the accuracy of the numerical method. The

C_P	0^o	-20^o	$+20^o$
Present	0.601	0.601	0.604
Ref. [33]	0.573	0.571	-

Table 4.1: Power coefficient for a constant loaded actuator disc at C_T=0.89 and cone angles β = 0^o, -20^o and $+20^o$.

values found by Madsen and Rasmussen are somewhat lower. The power coefficients presented here are seen to exceed slightly the Betz limit. Van Kuik [67] argues that a higher value is related to the behavior of the tip vortex, but as figure 3.5 shows, the added diffusion tends to

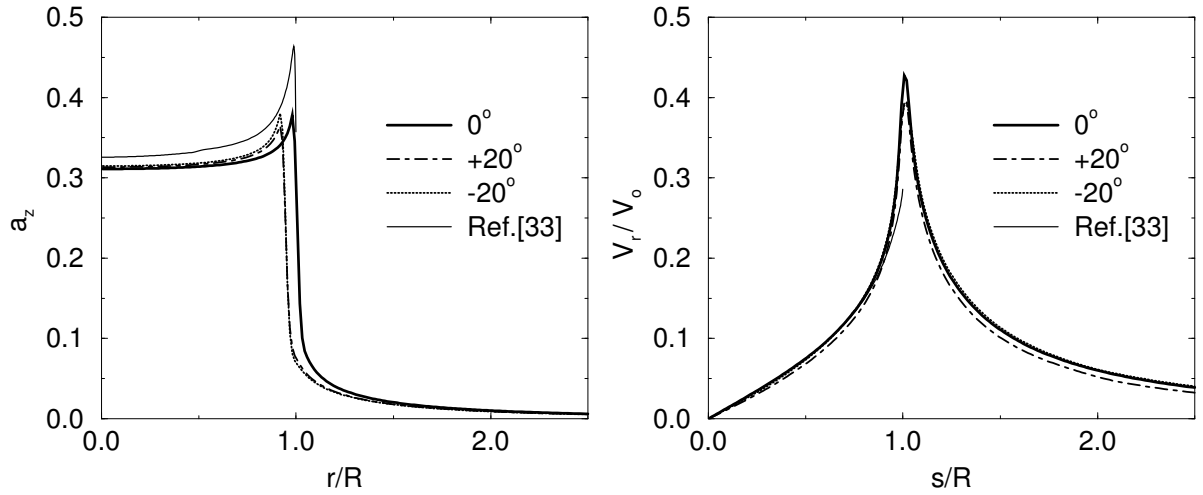

Figure 4.6: Axial interference factor in the radial plane through the tip and radial velocity along the radius of the disc for C_T=0.89

over predict C_P as compared to the Betz limit. A steady solution could not be obtained for higher Reynolds numbers (Re$\geq$100,000), suggesting that $C_T = 0.89$ is close to a stability limit at which the solution becomes unsteady. The diffusion can not be completely removed since artificial diffusion always is added to the flow, due to the numerics.

4.3.2 Simulation of the Tjæreborg Wind Turbine

In order to investigate the influence of coning for a real rotor, calculations have been performed with aerofoil data from the 2MW Tjæreborg wind turbine, although it has zero coning. The blade radius of the turbine is 30.5 m and it rotates at 22.1 RPM, corresponding to a tip speed of 70.7 m/s. The blade sections consist of NACA 44xx airfoils with a chord length of 0.9 m at the tip, increasing linearly to 3.3 m at hub radius 6 m. The blades are linearly twisted 1^o per 3 m. Further technical details can be found in [77]. In figure 4.7 the normal and axial interference factors for cone angles 0^o,$\pm$ 10^o and $\pm$ 20^o, computed by the Navier-Stokes algorithm,

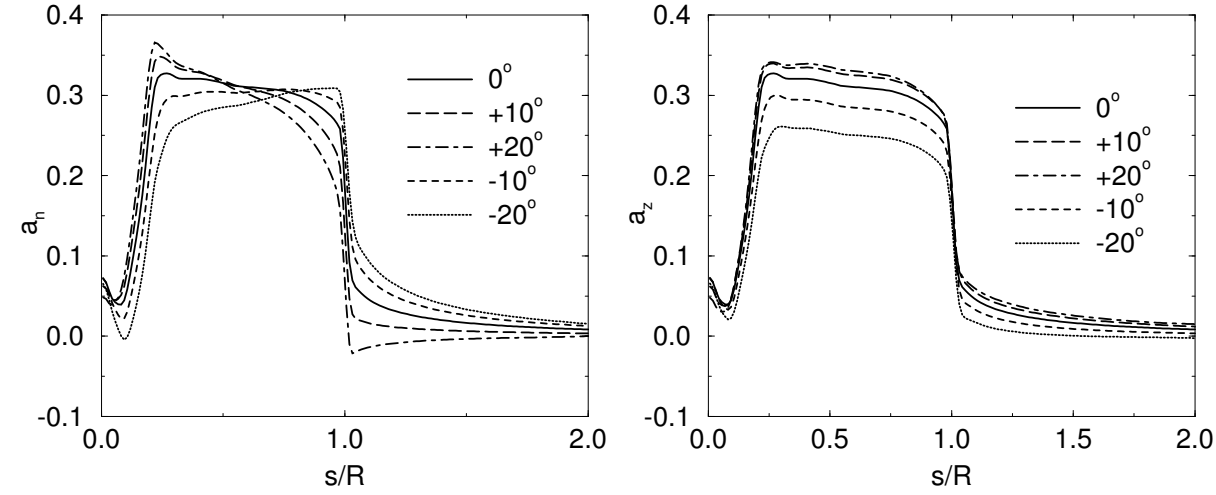

Figure 4.7: Normal and axial interference factors along the blade of the Tjæreborg wind turbine at V_o=10 m/s

are shown. The tip speed ratio is $\lambda = 7.07$, corresponding to V_o=10 m/s. Tip-correction is compensated for with Eq.(3.17) and setting $a = a_n$. The loading of the Tjæreborg wind turbine is nearly constant over most of the rotor and the computed a_n shows the same pattern as for the constant loaded actuator disc in figure 4.5. For $\beta = +20^o$, a_n attains its highest value near the hub after which it decreases continuously towards the tip. For $\beta = -20^o$, a_n is lower at the hub, increasing towards the tip to a level above the obtained level for $\beta = 0^o$. For a_z, however, the level is reduced about 20% for $\beta = -20^o$, as compared to that of $\beta = 0^o$. For upstream coning of 10^o and 20^o, the axial induction is found to be almost the same and about 5% higher than at $\beta = 0^o$. The rotational power coefficient, defined by Eq.(C.5) in App. A, is in figure 4.8 (left) compared with experimental data. The power coefficient is consistently defined with respect to the projected area for all considered rotors, since C_P is invariant to coning for the constant loaded rotor. For $\beta = 0^o$ the calculated C_P-value is found to be within 1-3% point of the experimental results. The velocity at which maximum C_P occurs is seen to agree well with the measured data. Coning of the rotor displays only a minor effect on C_P through the considered

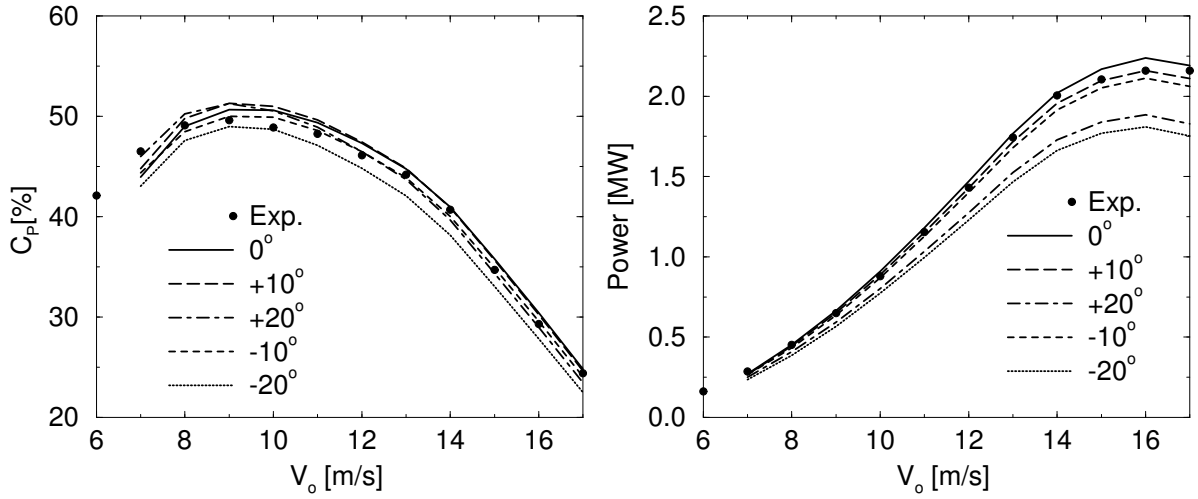

Figure 4.8: C_P and power distribution for the Tjæreborg wind turbine

velocity range, with the highest value appearing at upstream coning, where $C_{P_{max}}$ for $\beta = 20^o$ is increased with about 1% point as compared with $\beta = 0^o$. For downstream coning C_P is reduced about 1-2% point through the velocity range, which is partly explained by the decrease in relative velocity, as the streamlines are less orthogonal to the rotor plane. When looking at the power production, figure 4.8 (right), the highest output is obtained at 0^o which primarily is due to the reduced projected area when coning. At velocities above 13 m/s the pitch angle is regulated in order to keep a constant electrical power output of 2 MW and the calculated power is based on an averaged measured pitch angle. The structural load on each blade, based on aerodynamic forces only, is shown in figure 4.9, which depicts the normal load distribution and the shear force. For upstream coning, the changes in loading are a nearly constant reduction over the entire span, whereas for downstream coning the changes take place mostly in the outer part of the blade. Correspondingly, both the shear force (figure 4.9 right) and flap wise bending moment (not shown) are reduced with an increasing cone angle. Although upstream coning gives a slightly higher shear force at the root section, as compared to the corresponding downstream coning, the differences are found to be negligible. Thus, even though the difference in induced velocities between up- and downstream coning is considerable, the impact on integrated parameters is more moderate.

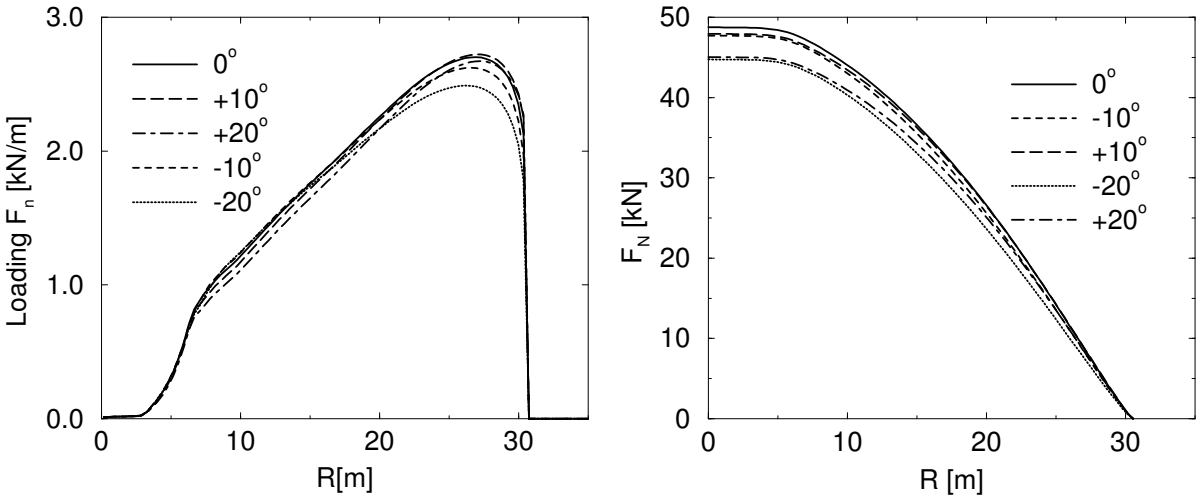

Figure 4.9: Distribution of aerodynamic load and shear force along the blade at V_o=10m/s

4.3.3 Comparison with the BEM Method for the Tjæreborg Wind Turbine

In figure 4.10 a a_n-distribution computed by the numerical actuator disc model is compared with results from the BEM method. It is observed that the agreement between the two methods generally is very good at $\beta = 0^o$, although deviations are seen near the tip. This is not the

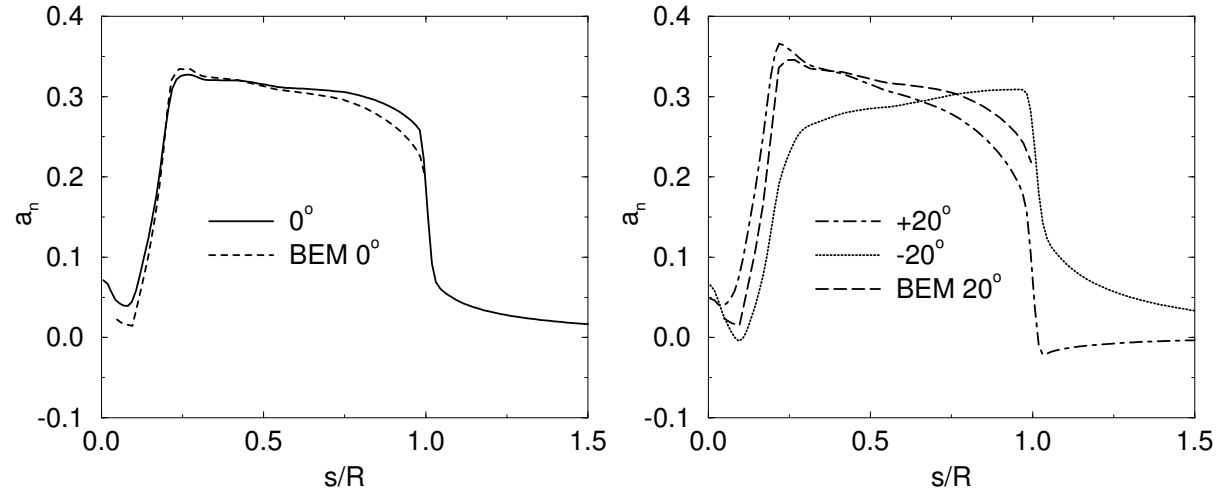

Figure 4.10: Normal interference factor calculated with the BEM and the Navier-Stokes method for the Tjæreborg wind turbine at V_o=10 m/s

case at $\beta = \pm 20^o$, however, where the a_n-distribution predicted by BEM has a higher level than at $\beta = 0^o$. The comparison with the Navier-Stokes method shows some agreement for $\beta = +20^o$, but at $\beta = -20^o$ the BEM method fails to capture the a_n-distribution. A simple estimate of the influence of coning would be to assume that the root shear force, F_N, is reduced according to the reduction of the projected area, i.e. it follows a $\cos^2\beta$ distribution. In figure 4.11 the computed $F_N = F_N(\beta)$ distributions are compared to a $F_N = F_N(\beta = 0^o)\cos^2\beta$ distribution at $V_o = 10m/s$. The comparison shows that the BEM method predicts a F_N-distribution which is just below the $\cos^2\beta$ dependency. In contrast to this, the distribution by the Navier-Stokes algorithm is everywhere higher and the error committed by the BEM method

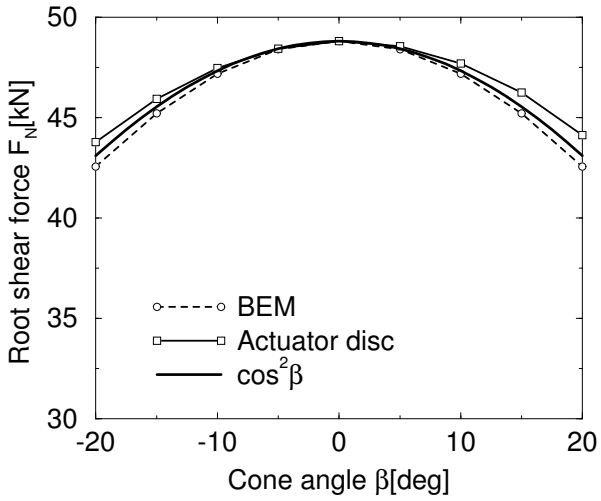

Figure 4.11: Shear force at the root section for V_o=10m/s, as a function of cone angle β

at $\beta = \pm 20^o$ amounts to about 3-4%. The same tendencies are found at higher freestream velocities. In figure 4.12, the difference in power coefficient, $\Delta C_P = C_P(\beta) - C_P(\beta = 0^o)$, between a straight and a $\pm 20^o$ coned rotor is shown as function of freestream velocity for the two methods. The results show a different behavior between the two models. The Navier-

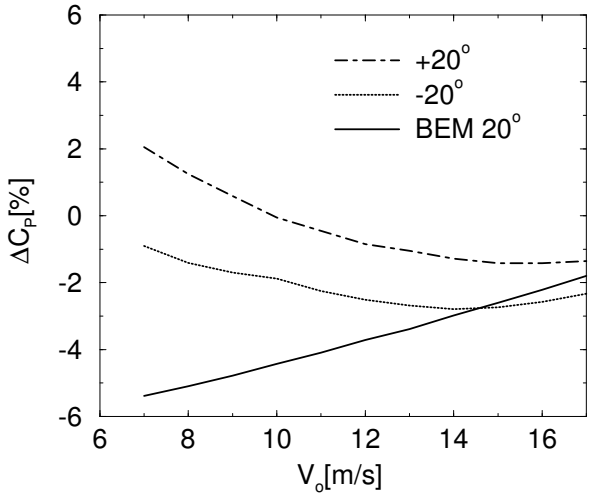

Figure 4.12: Difference in C_P as function of freestream velocity for $\beta = \pm 20^o$

Stokes computations demonstrate a decreasing tendency for an increasing freestream velocity, with a difference between up- and downstream coning that decreases from about 3 to 1% point over the considered velocity range. The opposite behavior is observed for the BEM method which underpredicts ΔC_P by up to 7% point at $\beta = +20^o$ and up to 4% point at $\beta = -20^o$, as compared with the numerical actuator disc model. Through the velocity range the two methods approach each other with a difference of about $\pm 0.5\%$ point at $V_o = 17m/s$.

4.4 Summary

The generalized actuator disc model and a modified BEM method for flows through coned rotors have been developed and tested for an actuator disc with constant load and a real rotor at

various coning angles. For the coned actuator disc with constant normal loading, the calculated interference factors a_n and a_z are found to change considerable along the radius of the disc. The BEM method can not reproduce this and there seems no easy way to model it, without violating the radial independence of the annular streamtubes. The calculated C_P for a constant loading of C_T=0.89 shows to be independent of coning, in accordance with theoretical considerations. The general trend of the results compares well with the findings of Madsen and Rasmussen [33]. Calculations of the Tjæreborg wind turbine display similar tendencies for the interference factors as for those of the constant normal loading. Thus, considerable changes in a_n and a_z were obtained in both cases with varying coning angle. The main explanation for this is the changed position of the rotor with respect to the trailing vortex system. A marginal increase in C_{Pmax} of about 1% point was obtained for an upstream coning of 20^o. Hence, coning leads to an overall power production that is reduced due to the reduction of the projected area. Comparing the structural loads calculated by the two models shows that the BEM method underpredicts the loads when increasing the cone angle. The predicted root shear force by the Navier-Stokes computations results only in minor differences between up- and downstream coning. Comparisons with BEM results at $\beta = \pm 20^o$ show that the BEM method underestimates the root shear force by about 3-4$\%$ and both methods follows a reduction that is proportional to the reduced projected area. The difference between the power coefficients computed at $\beta = 0^o$ and at $\beta = \pm 20^o$, ΔC_P, shows opposite tendencies between the two models. Where the Navier-Stokes method predicts a decreasing ΔC_P with increasing freestream velocity, the BEM method predicts an increasing ΔC_P with increasing freestream velocity. Furthermore, the BEM method underestimates C_P with up to 7$\%$ point at lower velocities. As a consequence, the BEM method may introduce significant errors when applied to rotors with substantial coning or large blade deflections.

Chapter 5

The Yawed Rotor

Although the flow through a rotor operating at yaw-misaligned conditions exhibit full 3D behaviour, yawed rotors are generally analyzed using axisymmetric methods. Here the generalized actuator disc model is used in combination with various sub models.

5.1 Yaw Modelling

Yaw modelling of wind turbine rotors is an important and difficult task to undertake owing to the unsteady nature of the inflow and the skewed wake geometry. In the past years a lot of effort has been put into providing accurate experimental data to improve engineering models predicting loads of wind turbine rotors at yawed conditions. In the European JOULE project "Dynamic Inflow: Yawed Conditions and Partial Span Pitch Control" [47] various yaw models were developed and incorporated into blade element momentum codes. In some validation cases, the refined models led to considerable improvements as compared to the original model, whereas they in some other cases showed to be in rather poor agreement with experimental data. Using the $(\Psi - \omega)$ finite difference formulation of the Navier-Stokes equations facilitates time true simulation of the dynamic wake. Here the method are used in combination with sub models for tower, wind shear, dynamic stall and elastic deflection.

5.1.1 3D Geometry and Kinematics

When considering rotors subjected to tilted or yawed inflow of substantial magnitude, axisymmetric assumptions are no longer sufficient, which calls for a full 3D projection of forces and velocities. The impact of a yawed rotor on the flow is a skewed wake which axisymmetric methods are incapable of capturing. However, with the axisymmetric $(\Psi - \omega)$ method it is proposed to use the 3D axisymmetric velocity vector extracted on the disc as inflow velocity to each blade. The disc velocities are then projected onto the normal and tangential directions of each individual blade, where, in case of yawed inflow, the radial velocity results in contributions which change sign depending upon whether the blade is moving upstream or downstream. Loading and related quantities are then determined for each individual blade at its circumferential position but the applied aerodynamic forces on the actuator disc are given as the span wise average of each blade.

5.1.2 Projection of Velocities

The velocities provided by the $(\Psi - \omega)$ model are given in a cylindrical polar frame, $\boldsymbol{V}_{r\theta z} = (V_r, V_\theta, V_z)$ where $\theta = \Omega t$. Locally, however, the span wise, normal and tangential velocity components are given by $\boldsymbol{V}_{stn} = (V_s, V_t, V_n)$. The local velocities are obtained through a series of coordinate transformations with respect to yaw, tilt, coning and flap wise deflection. Figure

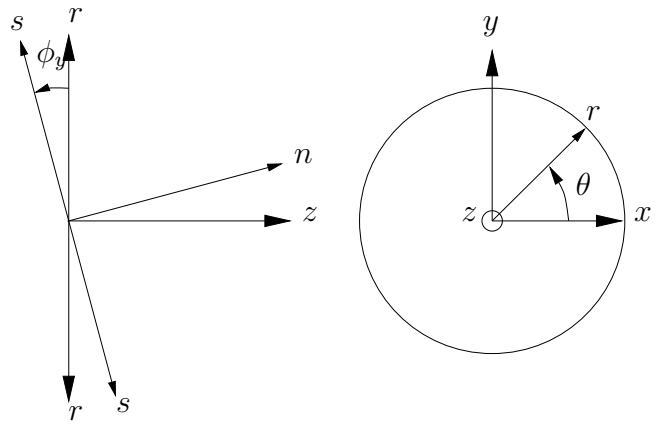

Figure 5.1: Yaw transformation seen from above and behind the rotor.

5.1 shows yaw and azimuthal angles, ϕ_y and θ, respectively. The yaw, tilt and azimuthal angles are defined positive using the right hand rule i.e. tilt as rotation about the x-axis, yaw about the y-axis and azimuth about the z-axis. The cone angle is defined positive as upstream coning as in the previous chapter. The polar velocities are first transformed to Cartesian components through the transformation matrix, $\boldsymbol{\Theta}$,

$$\boldsymbol{V}_{xyz} = \boldsymbol{\Theta}\boldsymbol{V}_{r\theta z}\ , \quad \boldsymbol{\Theta} = \begin{bmatrix} \mathrm{c} & -\mathrm{s} & 0 \\ \mathrm{s} & \mathrm{c} & 0 \\ 0 & 0 & 1 \end{bmatrix}, \tag{5.1}$$

where $\mathrm{s} = \sin\theta$ and $\mathrm{c} = \cos\theta$. Yaw, $\boldsymbol{\Phi_y}$, tilt, $\boldsymbol{\Phi_t}$, and coning/deflection, B, transformations from Cartesian to spanwise, tangential and normal components are found using

$$\boldsymbol{\Phi_y} = \begin{bmatrix} \mathrm{c} & 0 & -\mathrm{s} \\ 0 & 1 & 0 \\ \mathrm{s} & 0 & \mathrm{c} \end{bmatrix}, \quad \boldsymbol{\Phi_t} = \begin{bmatrix} 1 & 0 & 0 \\ 0 & \mathrm{c} & \mathrm{s} \\ 0 & -\mathrm{s} & \mathrm{c} \end{bmatrix}, \quad \mathrm{B} = \begin{bmatrix} \mathrm{c} & 0 & -\mathrm{s} \\ 0 & 1 & 0 \\ \mathrm{s} & 0 & \mathrm{c} \end{bmatrix}. \tag{5.2}$$

Whereas $\boldsymbol{\Phi_y}$ and $\boldsymbol{\Phi_t}$ transform a Cartesian vector to Cartesian, B transform from polar to spanwise, tangential and normal components i.e. before compensating for the influence of coning and deflection, as shown in Figure 5.2, the velocity vector is transformed back to polar components with $\boldsymbol{\Theta}^T$, hence, the full transformation is obtained by multiplying the matrices as follows

$$\boldsymbol{V}_{stn} = \mathrm{B}\boldsymbol{\Theta}^T\boldsymbol{\Phi}_t\boldsymbol{\Phi}_y\boldsymbol{V}_{xyz} = \mathrm{A}\boldsymbol{V}_{r\theta z}. \tag{5.3}$$

For most rotors, however, tilt and coning angles are small and in this case a reduced transformation which only include effects for rotors operating in yawed inflow, reduces to

$$\left\{ \begin{array}{c} V_t \\ V_n \end{array} \right\} = \left[\begin{array}{c|c|c} \cos\theta\sin\theta(1-\cos\phi_y) & \cos^2\theta + \sin^2\theta\cos\phi_y & \sin\theta\sin\phi_y \\ \cos\theta\sin\phi_y & \sin\theta\sin\phi_y & \cos\phi_y \end{array} \right] \cdot \left\{ \begin{array}{c} V_r \\ V_\theta \\ V_z \end{array} \right\}. \tag{5.4}$$

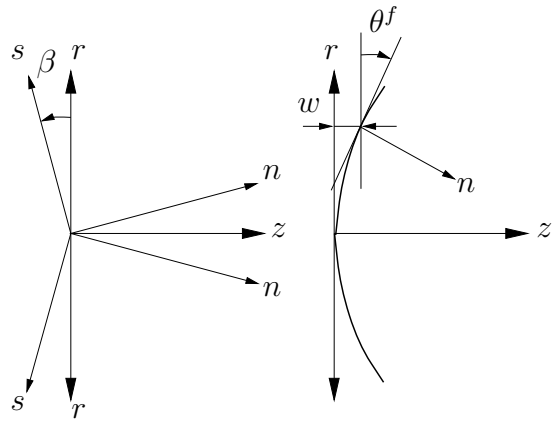

Figure 5.2: Coning and deflection of the blade seen from above, $\beta_f = \beta - \theta^f$.

The reduced transformation shows that radial velocity contributes to the unsteady loading, with increasing yaw angle ϕ_y, an effect which many methods neglect. The local flow angle and relative velocity along each blade are, apart from the flowfield velocities, affected by the influence from tower, elastic vibration of the blade, wind shear and turbulence. These effect are included in many different ways and will be introduced later. Using Eq.(5.3) the local flow angle and relative velocity are defined as $\phi = \tan^{-1}\left(\frac{V'_n}{-V'_t}\right)$ and $V^2_{rel} = V'^2_n + V'^2_t$ with

$$\boldsymbol{V}'_{stn} = \boldsymbol{V}_{stn} - \boldsymbol{e}_t \Omega s \cos\beta + \boldsymbol{V}^{\text{Tower}}_{stn} + \dot{\boldsymbol{v}}_{stn} + \boldsymbol{V}^{\text{Turb}}_{stn} \tag{5.5}$$

where $\dot{\boldsymbol{v}}_{stn}$ denote the velocity of the vibrating blade. It should be noted that wind shear is included by correcting the axial velocity component before the stn-projection of the field and tower influence is made.

5.1.3 Blade Forces

Given the local relative velocity vector $\boldsymbol{V}'_{stn}$ the flowangle $\phi = \tan^{-1}\left(\frac{V'_n}{-V'_t}\right)$ and relative velocity $V_{rel} = \sqrt{V'^2_n + V'^2_t}$ are used to determined the aerodynamic blade forces $\boldsymbol{F}_{stn}$ found from Eqs.(2.8) and (4.4).

5.1.4 Sub Models

The measured response on an operating wind turbine blade consist of many individual contribution, which should be added to the incoming mean wind speed. For the wind field alone such effects include the atmospheric boundary layer, turbulence and terrain topology. Here four different sub models are considered in order to make a more realistic comparisons with experimental data. First of all, a wind turbine is a structure that consists of many different parts with certain dynamic characteristics. As the main focus of this work concerns the rotor alone, the elastic analysis is restricted to the dynamic response of the blades. In this respect, the tower has an aerodynamic effect on the loading of each blade which is experienced as a rapid change in aerodynamic load and corresponding blade deflections as it passes the tower. The tower is included as a dipole and a source, as described by Björck [4]. Unsteady loading in connection with yaw-misalignment, wind shear or turbulence which changes the angle of attack may be

included with a dynamic stall model. Wind shear is included by a curve fitted power law. In the present work turbulence is not included. To summarize the used models are as follows:

- Elastic modal method, Appendices B.1-B.1.2
- Tower model - dipole and source, Appendix B.2
- Dynamic stall - Øye model, Appendix B.3
- Boundary layer or wind shear - power law, Appendix B.4

The elastic model of the blades is a standard modal method, where the two lowest modes in the flap and chord wise directions are included, hence torsion is neglected.

5.2 Numerical Results for the Yawed Rotor

The present investigation concerns the Tjæreborg wind turbine in yawed inflow at conditions presented in Table 5.1.

ϕ_y	V_o [m/s]	α_s	Tu. I [%]
32^o	8.5	0.31	8
54^o	7.8	0.30	2
-51^o	8.3	0.27	11
-3^o	8.6	0.17	very low

Table 5.1: Conditions for the measurements on the Tjæreborg wind turbine in yawed inflow, $\Omega = 22.0$ rpm, pitch: 0.5^o. From [47]. Wind shear coefficient : α_s (See Appendix B.4), Turbulent intensity : Tu. I[%].

The structural data for the Tjæreborg blade, which may be found in Øye [76] or Hansen [25], are used to establish a basis of eigenmodes representing the relevant deflection shapes of the blades. The modes are obtained with an iterative method described by Hansen [25] and the first few eigenfrequencies found using 40 elements are given in table 5.2. The results compare well with experimental observations [76].

Eigenfreq.[Hz]	Flap	Chord	Torsion	Exp.Flap[76]	Exp.Chord
1'st	1.198	2.357	-	1.17	2.30
2'nd	3.434	7.944	-	-	-

Table 5.2: Obtained eigen-frequencies for the Tjæreborg blade using 40 points.

Using the actuator disc the influence of including projections of the radial flow component was investigated in [38]. Although the method is axisymmetric and thereby assumes an even magnitude of radial velocity for all the blades, the projection of the radial velocity is justified with figure 5.3. The figure displays a computed radial velocity profile for the Tjæreborg turbine at $V_o = 8.6m/s$ and $\phi_y = -3^o$, which shows that the outward radial flow component increases continuously towards tip to a maximum of about 35% of the free stream velocity.

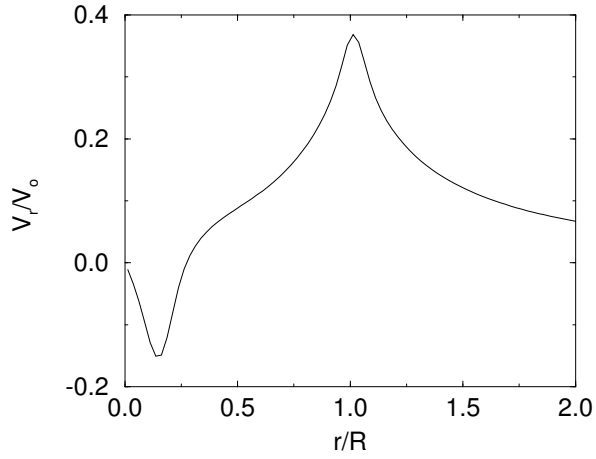

Figure 5.3: Computed radial velocity for the Tjæreborg turbine, $V_o = 8.6m/s$, $\phi_y = -3^o$.

In the hub region the lack of axial thrust results in an inward flow towards the center axis. This is, however, of limited importance as the area of this region is about 5% of the total disc area. The result presented in [38] revealed significant changes by including effects of the radial flow component, towards improved predictions of the flapwise bending moment. Important effects from wind shear and dynamic stall were, however, not included which is presented in the following.

In Figure 5.4 predictions for the root bending moments, Eq.(B.28), at yaw angles -3^o and $+32^o$ are compared with bin averaged experimental data from [47] and a case with uniform inflow, presented in [39]. The tower is placed at an angular position of 270^o and the drag coefficient is

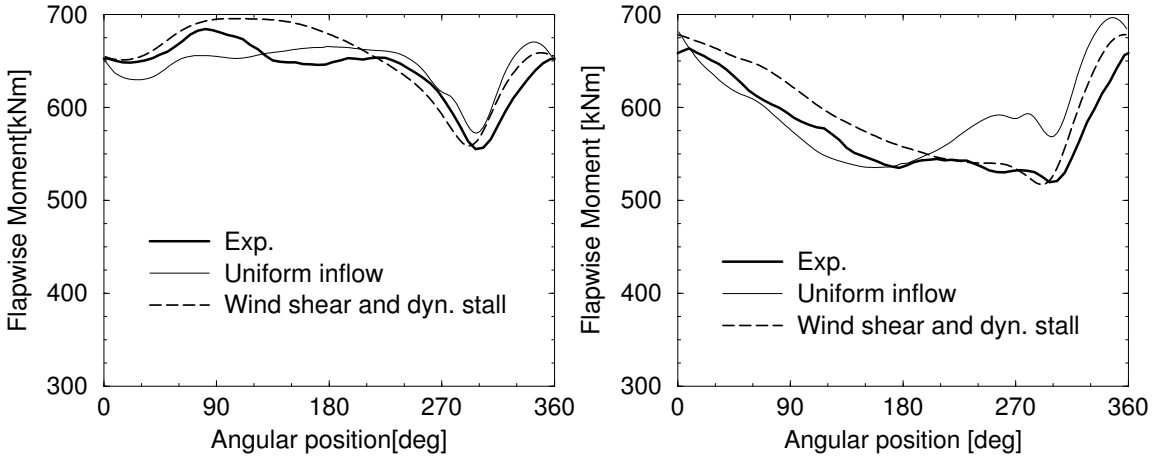

Figure 5.4: Flap wise moment at the root section (r=2.75m) of the Tjæreborg turbine at yaw angles -3°(left) and +32°(right)

set to $C_D = 0.7$. For the yawed case of $\phi_y = -3^o$ both predictions are in excellent agreement with measurements although the tendency from wind shear shows a slightly better trend. In the tower region the huge peak match well for both computations. At a yaw angle of $\phi_y = +32^o$ the prediction for the uniform inflow is in good agreement for the main part but some deviations still exist in the tower region. Including wind shear improves the prediction to a nearly perfect

match in the tower region. Computations presented in figure 5.5 shows the two other cases with high yaw angles, $\phi_y = -51^o$ and $\phi_y = +54^o$. At $\phi_y = -51^o$ the full projection gives clearly

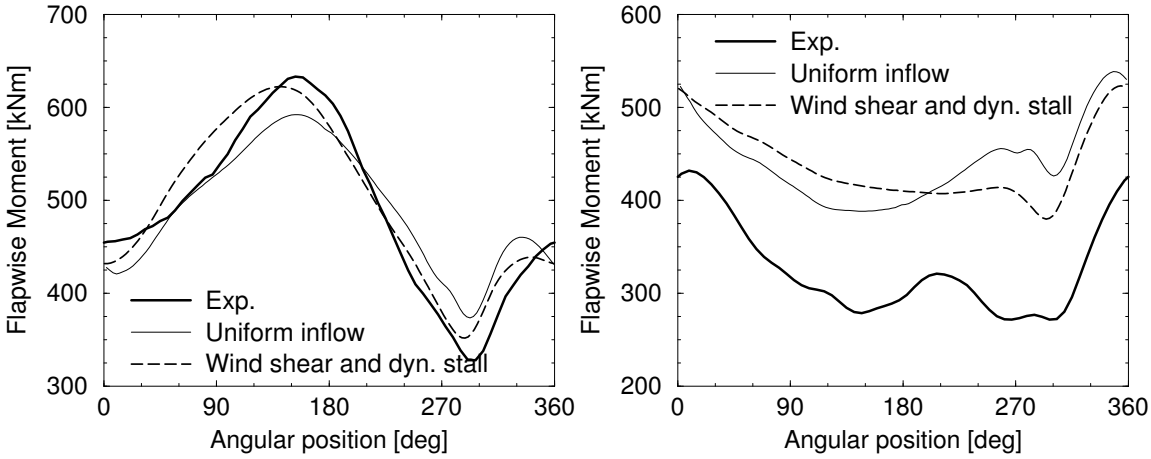

Figure 5.5: Flap wise moment at the root section of the Tjæreborg turbine for yaw angles $\phi_y = -51^o$ (left) and $\phi_y = +54^o$ (right).

the best result. However, at $\phi_y = +54^o$ both computations over predict the flap wise moment with up to 40%, although the general trend is reasonable predicted. The likely explanation for this deviation is the assumptions of axisymmetry which the actuator disc model is founded on. Finally, it should be noted that the accuracy of the bin averaged measurements is believed to be good, although Øye has stated that the offset error could be of the order $\pm$100kNm. To some degree, this could explain the rather bad prediction at $\phi_y = +54^o$

5.3 Summary

The computations carried out on the Tjæreborg wind turbine subjected to yawed inflow conditions, have demonstrated that the combined models capture the behaviour of the structural loads with a good accuracy. Including wind shear and dynamic stall models, result in clear improvements as compared with uniform inflow, but at $\phi_y = +54^o$ the computed predictions does not show convincing accuracy. Although the model is axisymmetric, the dynamic wake behind the rotor is developed in a fully unsteady manner and the modelling is throughout based on projection of the full axisymmetric velocity vector. The lack of a skewed wake is, however, one of the major limitations of the method.

Chapter 6

Modelling of Tunnel Blockage

Experimental investigations on rotors has in the past mainly been focused on propellers, however, recently large scale tests on wind turbine rotors were conducted by NREL and similar test are in preparations within the European community. A spin-off in connections with the recent and proposed test is a renewed interest in the effects of tunnel blockage. Wind tunnel blockage in connection with experimental tests of propellers was treated by Glauert (1934) for a constant loaded rotor disc in a tunnel with a constant cross sectional area. Recently Hackett et al. (1998) discussed the accuracy of representing the expansion or contraction of the wake of a turbine or propeller by sources or sinks, respectively, which increases the generality of tunnel correction. Mikkelsen and Sørensen [40](2002) used the generalized actuator disc method modified to cope with the influence of tunnel walls, to analyze the effect of tunnel blockage. The method is presented in the following as well as a new solution to the inviscid momentum analysis by Glauert. Computed results are presented for a constant loaded rotor disc and for the LM 19.1m blade using the generalized actuator disc model.

6.1 Axial Momentum Theory

The direct effect of the tunnel walls is to constrain the flow, thereby changing the resulting loading and induced velocities. This interference may be represented by an equivalent free air speed V'. Considering a uniform inflow V_o through a wind tunnel with a rotor disc inserted, as shown in figure 6.1, and assume the flow to be incompressible, continuity through and outside the rotor disc yields that

$$u_1 S_1 = uS \,, \tag{6.1}$$

$$u_2(C - S_1) = V_o C - uS \,, \tag{6.2}$$

where u is the velocity at the rotor disc, u_1, u_2 are velocities in the far wake inside and outside, respectively, of the stream tube passing through the rotor disc. The disc area is given by S, C is the total tunnel area and S_1 is the slipstream area in the far wake found as the limiting streamline through the edge of the disc. Outside the slipstream the total pressure head remains constant, i.e. $p_o + \frac{1}{2}\rho V_o^2 = p_2 + \frac{1}{2}\rho u_2^2$. Inside, the decrease in total head equals the decrease in pressure through the disc, $p_o + \frac{1}{2}\rho V_o^2 + p'_+ = p'_- + p_1 + \frac{1}{2}\rho u_1^2$, where $p_1 = p_2$. Immediately in front and after the rotor disc, we have (p'_+, p'_-) representing the pressure jump across the disc which is

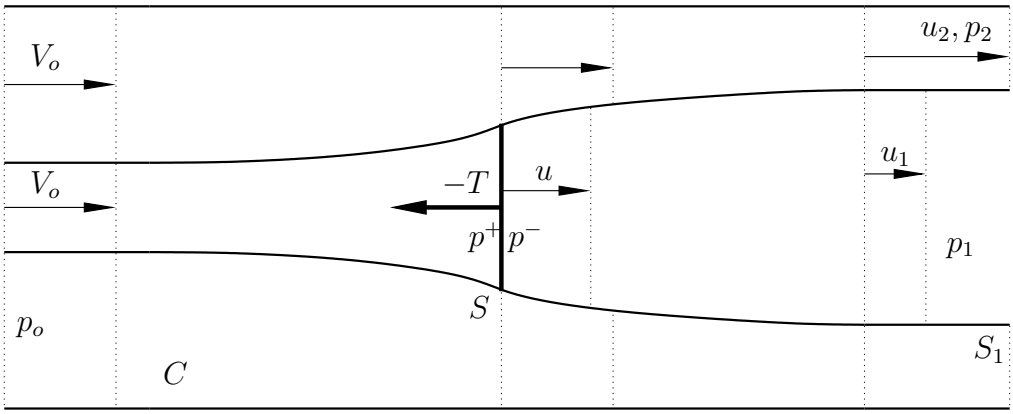

Figure 6.1: A rotor disc inserted into a wind tunnel where V_o, u are velocities, C, S, S_1 are areas for tunnel, disc and far wake expansion and p is the pressure.

directly proportional to the thrust, $T/S = p'_+ - p'_-$. Hence, the thrust and pressure jump yields

$$T = \tfrac{1}{2}\rho S(u_1^2 - u_2^2)\ , \tag{6.3}$$

$$\Delta p = p_1 - p_o = \tfrac{1}{2}\rho(V_o^2 - u_2^2)\ . \tag{6.4}$$

Finally, applying the momentum equation on the whole tunnel, we get

$$\begin{aligned} T - (p_1 - p_o)C &= \rho u_1 S_1(u_1 - V_o) \\ &\quad -\rho u_2(C - S_1)(V_o - u_2)\ . \end{aligned} \tag{6.5}$$

Thus, five equations with five unknowns, u, u_1, u_2, S_1, p_1 is obtained. Introducing the following non-dimensional quantities

$$\sigma = \frac{S_1}{S},\ \alpha = \frac{S}{C},\ u = \frac{u}{V_o},\ u_1 = \frac{u_1}{V_o},\ u_2 = \frac{u_2}{V_o}, \tag{6.6}$$

the set of equations is rewritten as

$$u_1\sigma = u, \tag{6.7}$$

$$u_2(1 - \alpha\sigma) = 1 - \alpha u, \tag{6.8}$$

$$C_T = u_1^2 - u_2^2, \tag{6.9}$$

$$C_p = \frac{\Delta p}{\frac{1}{2}\rho V_o^2} = 1 - u_2^2, \tag{6.10}$$

$$\begin{aligned} \alpha C_T - C_p &= 2u_1\sigma\alpha(u_1 - 1) \\ &\quad -2u_2(1 - \alpha\sigma)(1 - u_2)\ , \end{aligned} \tag{6.11}$$

where $C_T = T/\frac{1}{2}\rho V_o^2 S$ is the thrust coefficient. Inserting Eqs.(6.7)-(6.10) into Eq.(6.11) leads to a 2nd order polynomium for u in terms of σ and α, where the sign on the solution is controlled by the direction of the thrust. It is, however, possible to reduce the polynomium to an explicit expression for the solution that gives an unique relation of u in terms of σ and α

$$u = \frac{\sigma(\alpha\sigma^2 - 1)}{\sigma\alpha(3\sigma - 2) - 2\sigma + 1}\ , \tag{6.12}$$

This solution is by no means obvious, but may be deduced with the use of formula manipulation software. The range in which α and σ may vary can at first be set to $\alpha \equiv \frac{S}{C} \leq 1$, $\sigma \equiv \frac{S_1}{S} \in [1, \frac{1}{\alpha}]$. With u determined, u_1, u_2 and C_T are obtained from Eqs.(6.7)-(6.9) and the power coefficient C_P as

$$C_P = C_T u = u(u_1^2 - u_2^2) \; . \tag{6.13}$$

The range at which the solution can be considered valid in terms of α and σ is not entirely given by the range stated above. At least for a turbine some upper C_T limit will exist as the flow is bound to separate with increasing C_T. Defining the equivalent free air speed V' as the speed that gives the same thrust T for a corresponding disc velocity u from Eq.(6.12), we have in free air that $C_T = 4u(u - V'/V_o)$, hence

$$V'/V_o = u - \frac{1}{4}\frac{C_T}{u} \; . \tag{6.14}$$

Glauert derived the approximate relation

$$V'/V_o = 1 - \frac{1}{4}\frac{R_{rot}^2}{R_{tun}^2}\frac{C_T}{\sqrt{1+C_T}} \; , \tag{6.15}$$

where the thrust coefficient is restricted to $-1 < C_T \leq 0$ for the wind turbine. As pointed out by Hackett et al. [23], Glauert did not discuss the potential of applying the correction to wind turbine flow, but Eq.(6.15) is also valid for negative values of C_T, although it becomes singular for $C_T = -1$. This is not the case with Eq.(6.14). Equation (6.15) has, however, the advantage of only depending on C_T and the aspect ratio and not on the expansion ratio σ.

6.1.1 Actuator Disc Method

With the generalized actuator disc method formulated in vorticity - swirl velocity - stream function variables, axisymmetric tunnel walls are conveniently introduced with a slip condition applied to the outer lateral boundary. The slip condition is introduced by keeping a constant stream function level i.e.

$$V_r = 0 \;\; \Rightarrow \;\; \Psi = \frac{V_o r^2}{2}, \tag{6.16}$$

thus restricting the expansion of the streamlines. Although the tunnel walls are considered inviscid, hence neglecting viscous boundary layer growth from the walls, the main effects from the changed static pressure field is naturally included.

6.2 Navier-Stokes Computations

In order to compare axial momentum theory with Navier-Stokes computations the constant loaded rotor for $C_T = 0.8$ is considered. The effect of tunnel walls on a real rotor is simulated using data for the LM 19.1m blade. Simulations using the numerical actuator disc model gives the solution of the axisymmetric velocity and vorticity field. During post processing an additional pressure equation is solved for the total pressure head to give the static pressure (see Appendix A.5.

6.2.1 The Constant Loaded Rotor

The static pressure field for a constantly loaded rotor $C_T = 0.8$ in an infinite domain and $R_{tun}/R_{rot} = 2.5$ is shown in figure 6.2. Restricting the tunnel size to $R_{tun}/R_{rot} = 2.5$ gives

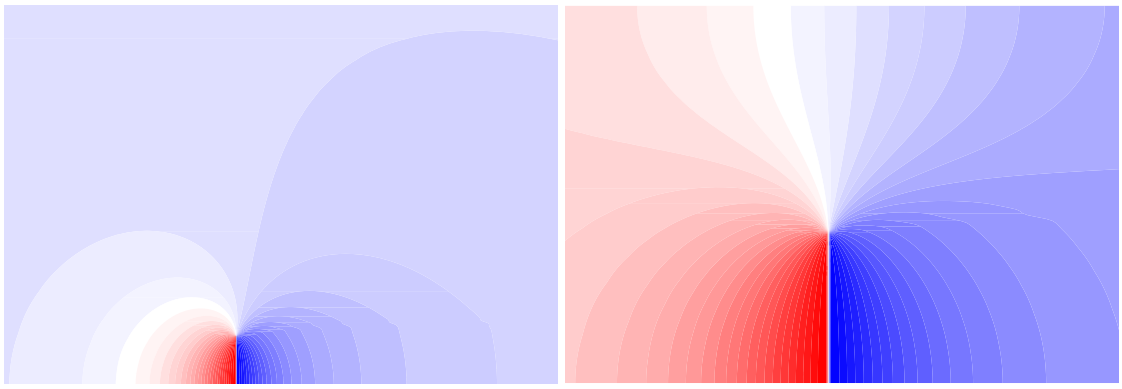

Figure 6.2: Static pressure field around a constant loaded rotor, $C_T = 0.8$, $R_{tun}/R_{rot} \rightarrow \infty$ (left) and $R_{tun}/R_{rot} = 2.5$ (right). The high pressure region infront of the disc is red and the low pressure region behind is blue.

a pronounced effect which is clearly seen in terms of a global decrease in static pressure between the inlet and exit of the tunnel. Across the vorticity shed the static pressure is virtually unaffected. The axial velocity profile $V_z(r)$ in the plane of the rotor is shown in figure 6.3(left) which shows the speed up in the flow outside the rotor with decreasing aspect ratio; hence an expected velocity increase through the rotor. The equivalent free air speed V'/V_o, determined by

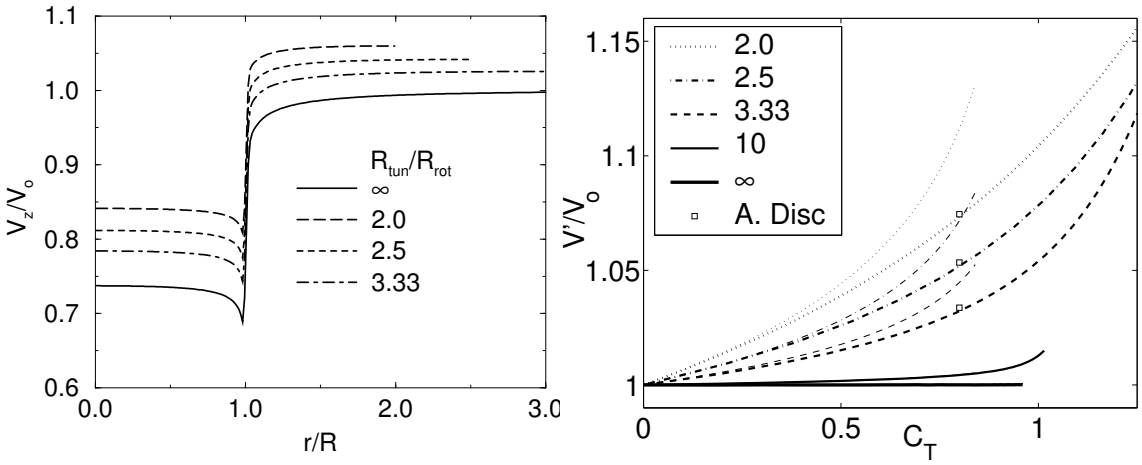

Figure 6.3: Velocity distribution for the constant loaded rotor, $C_T = 0.8$ (left) and correction velocity (right) V'/V_o for the present model and the actuator disc model, compared with the approximate expression by Glauert(thin lines).

the approximate formula given by Eq.(6.15) and by the exact solution, Eq.(6.14), is presented in figure 6.3(right). The result obtained with the actuator disc model for $C_T = 0.8$, marked into the plot, shows a nearly perfect match compared to the exact solution. As mentioned earlier, Eq.(6.15) is singular at $C_T = 1$ which results in an error of about 2-4% point for $C_T = 0.8$ as

compared to the actuator disc. Table 6.1 shows the numerical values obtained for $C_T = 0.8$. The values are based on Eq.(6.14) and the mean axial velocity profile

R_{tun}/R_{rot}	Eq.(6.15)	Eq.(6.14)	Actuator Disc
∞	1	1	1
10.0	1.004	1.004	-
3.33	1.045	1.032	1.034
2.5	1.072	1.052	1.053
2.0	1.112	1.073	1.075

Table 6.1: The correction on equivalent free air speed V'/V_o for a constant loaded rotor, $C_T = 0.8$.

$$u = \frac{1}{S}\int_0^R \frac{V_z(r)}{V_o} 2\pi r dr \ . \tag{6.17}$$

For the propeller, Glauert states that the error using the approximate expression is less than 1% for $C_T = 6$ at an aspect ratio of 2. This shows that Eq.(6.15) is valid for the propeller within this range, but for the turbine the error increases faster as the thrust increases, due to the singular behaviour.

6.2.2 Simulation of the LM 19.1m Blade

Figure 6.4 displays equivalent static pressure fields for the LM 19.1m blade for $V_o = 7$m/s. Inevitably, the flow through real rotors results in added tangential velocities in the wake. From

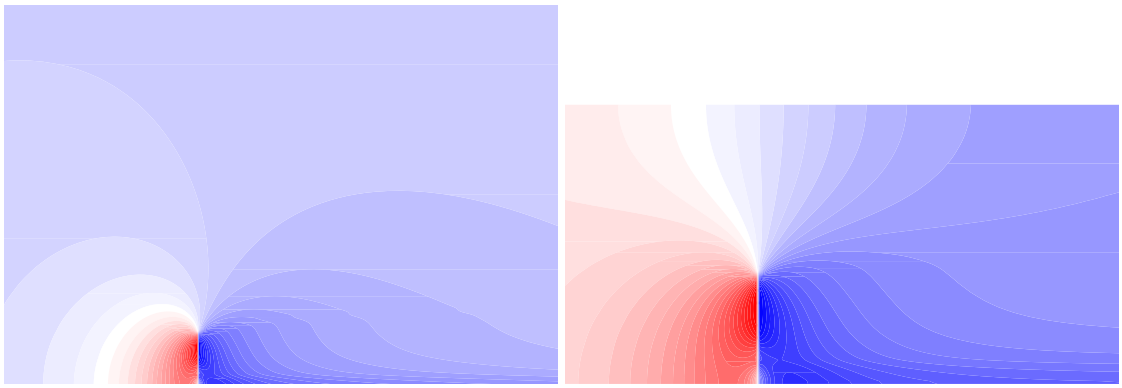

Figure 6.4: Pressure field using LM 19.5 aerofoil data, $V_o = 7$m/s, $R_{tun}/R_{rot} \rightarrow \infty$, and $R_{tun}/R_{rot} = 2.5$.

the figure it is seen that the added circulation to the flowfield results in a preserved static low pressure region along the center axis in the far wake due to the centrifugal forces. Figure 6.5 shows the axial velocity profile obtained with a inflow tunnel speed of 7m/s and 10m/s, respectively. Computations on the LM 19.1m blade displays the same trends as observed for the constant loaded rotor, although the profile is far from constant. Increasing the velocity to $V_o = 10$m/s and $V_o = 14$m/s, thus reducing the thrust coefficient, results in a reduction of the

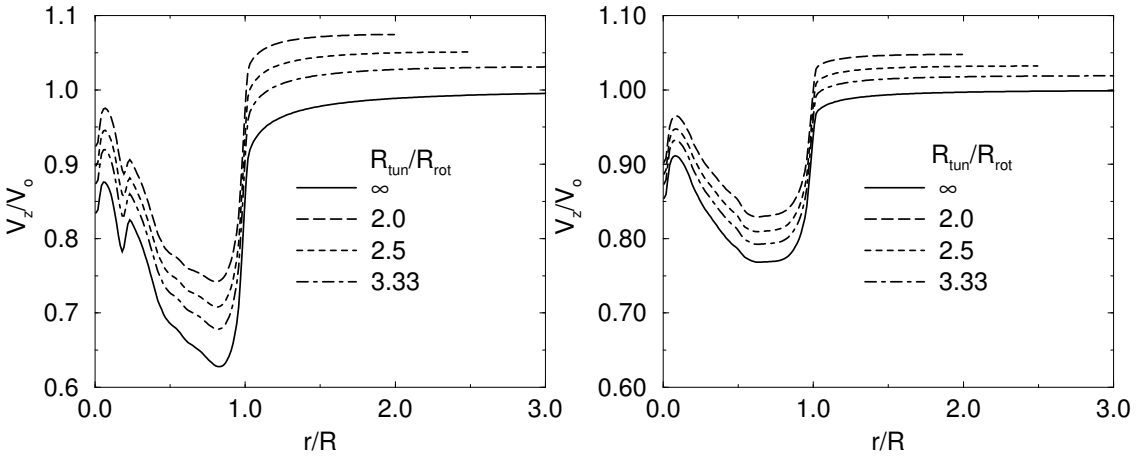

Figure 6.5: Velocity distribution for the LM 19.1m blade at $V_o = 7$m/s and $V_o = 10$m/s.

effect of tunnel walls, but not completely. Even at $V_o = 14$m/s there is a noticeable effect. In table 6.2, corresponding to table 6.1, the equivalent free air speed for the LM19.1m blade at 7, 10 and 14 m/s is presented. At 7m/s the thrust coefficient is close to 1 which result in corrections

R_{tun}/R_{rot}	7.0 m/s	10.0 m/s	14.0 m/s
∞	1	1	1
10.0	1.004	1.004	1.004
3.33	1.041	1.027	1.015
2.5	1.069	1.043	1.023
2.0	1.101	1.062	1.033

Table 6.2: The correction on equivalent free air speed V'/V_o for the LM19.1m blade

of the order 4-10 % point on the equivalent free air speed.

6.3 Summary

The generalized actuator disc effectively models the effects of tunnel blockage by changing the outer lateral boundary condition. The solutions compares excellent with the exact solution derived from axial momentum balance for the constant loaded rotor. Calculations on the LM19.1m blade predicts comparable trends to that of the constant loaded rotor. The equivalent free air speed at high loadings may in some cases need correction of up to 10 % point.

Part C

Actuator Line Modelling

Chapter 7

The Actuator Line Model

Whereas axisymmetric methods are limited to averaged values of azimuthal variations the axisymmetric assumptions are put a side with the actuator line method. The method, introduced recently by Sørensen and Shen [61], combines the three-dimensional Navier-Stokes equations with a technique where body forces are distributed along lines representing each blade. Their analysis demonstrated a good agreement with a measured power curve for the three-bladed 500 kW Nordtank wind turbine. Useful information about the wake structures and the azimuthal distribution of the induced velocities in the rotor plane were also obtained. The present work is focused on extending the concept to include yaw misalignment, tower effect and elastic behaviour of each blade. Furthermore, an investigations of the tip correction for the optimal rotor (Betz) is conducted.

7.1 The Flow Solver - EllipSys3D

The first formulation of the actuator line concept [61] was formulated in vorticity-velocity $(\boldsymbol{\omega} - \boldsymbol{V})$ variables. In the present work the method is combined with EllipSys3D, a general purpose 3D flow solver developed by Sørensen [62] and Michelsen [35, 36]. The flow solver is a multi block, finite volume discretization of the Navier-Stokes equations in general curvilinear coordinates. The code is formulated in primitive variables (i.e. pressure-velocity variables, polar or Cartesian) in a collocated storage arrangement and Rhie / Chow interpolation is used to avoid odd / even pressure decoupling. The main differences between the two formulations[1] are the absence of pressure in the first formulation and vorticity in the last. Furthermore, body forces appear in the $(\boldsymbol{\omega} - \boldsymbol{V})$ formulation by applying the curl operator to the force vector whereas the divergence is applied when solving the pressure equation in the last formulation. In both formulations the forces appear as distributed source terms, however, the numerical formulations are very different and therefore sensitivity to grid resolution, and distribution of force deviates between the two methods, although they are formulated to the same numerical order.

[1] Whereas the EllipSys3D code runs on parallel machines with distributed memory using MPI, the $(\boldsymbol{\omega} - \boldsymbol{V})$ formulation was implemented as a one-block vectorized code. Presently, however, access to vector machines are not available.

7.2 Numerical Formulation

The calculation domain is a regular axisymmetric polar grid, divided into a number of blocks with an equal amount of points in each direction. In the vicinity of the actuator lines, referred to as the near domain, grid points are concentrated in order to capture gradients. Within the near domain points are distributed equidistantly in each direction, $1R$ up- and downstream and $1R$ in radial direction. Outside the near domain, the grid points are stretched away towards the outer boundaries, about $10R$ upstream, $20R$ downstream and $10R$ in radial direction. In essence the grid is first distributed in axial and radial direction and then rotated equidistantly in the circumferential direction. One block per actuator line is used in the circumferential direction. When considering the flowfield around yawed rotors in a fixed computational domain given by (r, θ, z) and equivalent velocities, the calculation may be approached in two ways:(I) The rotor is yawed relative to the inflow which is chosen parallel with the z-axis or:(II) The direction of the inflow, governed by inflow boundary conditions, is yawed relative to the orientation of the domain or grid. The advantaged of the first approach is that the wake behind the rotor is better preserved, however, the evaluation of velocities and distribution of forces is somewhat more complicated than with the second approach. In the following both methods are considered.

7.2.1 Blade Forces and Tip Correction

Given the local flow angle and relative velocity the aerodynamic forces $\boldsymbol{F}_{stn}$ are found from Eqs.(2.8)-(4.4). In terms of applying the forces onto a flow domain given in a polar frame (r, θ, z), the local forces are reprojected

$$\boldsymbol{F}_{r\theta z} = \boldsymbol{\Theta}^T \boldsymbol{\Phi}_y^T \boldsymbol{\Phi}_t^T \boldsymbol{\Theta} \mathrm{B}^T \boldsymbol{F}_{stn} = \mathrm{A}^{-1} \boldsymbol{F}_{stn}, \tag{7.1}$$

where the span wise component $F_s = 0$. With respect to tip correction the theories developed by Prandtl [43] and Goldstein [21] are introduced into BEM and actuator disc methods to compensate for the finite number of blades. As the actuator line method in principle is fully three dimensional and naturally includes the number of blades, no correction method, such as the one by Prandtl is needed. This issue will be addressed in detail later.

7.3 Determinations of Velocities

First, the actuator lines are considered to be straight and rotate in a fixed plane that might be coned, yawed or tilted in any direction relative to the inflow direction (chosen parallel with the z-axis). The blade coordinates are given by the span wise direction along the blade, tangential direction within the rotational plane and the normal direction with respect to the rotational plane, denoted (s, t, n). Preserving the definitions of the yaw, tilt and cone angle previous introduced, the coordinate transformations presented in section (5.1.1) are used to define the relation between blade $\boldsymbol{x}_{stn}$ and Cartesian grid coordinates $\boldsymbol{x}_{xyz}$, i.e.

$$\boldsymbol{x}_{xyz} = \boldsymbol{\Phi}_{\boldsymbol{y}}^{\boldsymbol{T}} \boldsymbol{\Phi}_{\boldsymbol{t}}^{\boldsymbol{T}} \boldsymbol{\Theta} \boldsymbol{B}^{\boldsymbol{T}} \boldsymbol{x}_{stn}, \tag{7.2}$$

and with polar coordinates

$$\boldsymbol{x}_{r\theta z} = \boldsymbol{\Theta}_1^{-1} \boldsymbol{x}_{xyz} = \boldsymbol{A}_1^{-1} \boldsymbol{x}_{stn}. \tag{7.3}$$

Here the polar positions coordinates $\boldsymbol{x}_{r\theta z} = (r, \theta, z)$ are found by resolving[2] $\boldsymbol{\Theta}_1^{-1}$ as

$$\begin{aligned} r &= \sqrt{x^2 + y^2}\,, \quad z = z \\ \theta_1 = \tan_2^{-1}\left(\frac{y}{x}\right)\,, \quad \theta &= \theta_1 - \pi\left(\frac{\theta_1 + \varepsilon}{|\theta_1 + \varepsilon|} - 1\right)\,, \quad \theta \in [0, 2\pi[, \quad \varepsilon \approx 10^{-15}. \end{aligned} \tag{7.4}$$

With the blade coordinates $\boldsymbol{x}_{stn}^{i_B} = (1, t + 2\pi\frac{i_B - 1}{B}, 0)$ a unit vector $\boldsymbol{e}_{r\theta z}$ is determined for each blade as

$$\boldsymbol{e}_{xyz}^{i_B} = \boldsymbol{\Phi}_{\boldsymbol{y}}^{\boldsymbol{T}}\boldsymbol{\Phi}_{\boldsymbol{t}}^{\boldsymbol{T}}\boldsymbol{\Theta}\boldsymbol{B}^{\boldsymbol{T}}\boldsymbol{x}_{stn}^{i_B}\,, \quad \boldsymbol{e}_{r\theta z}^{i_B} = \boldsymbol{\Theta}_1^{-1}\boldsymbol{e}_{xyz}^{i_B} = \boldsymbol{A}_1^{-1}\boldsymbol{x}_{stn}^{i_B}\,, \quad i_B = 1, B. \tag{7.5}$$

In the computational domain the resolution of each line is chosen equal to the grid resolution in the near domain i.e. $\Delta s = \Delta r$, and as the lines move in the regular grid, cells which contain line points are identified by means of a truncation procedure. The velocities at predefined line points is then found using linear interpolation between the surrounding cell-centered values in all three directions. Figure 7.1 depicts a part of the grid structure with an actuator line inserted.

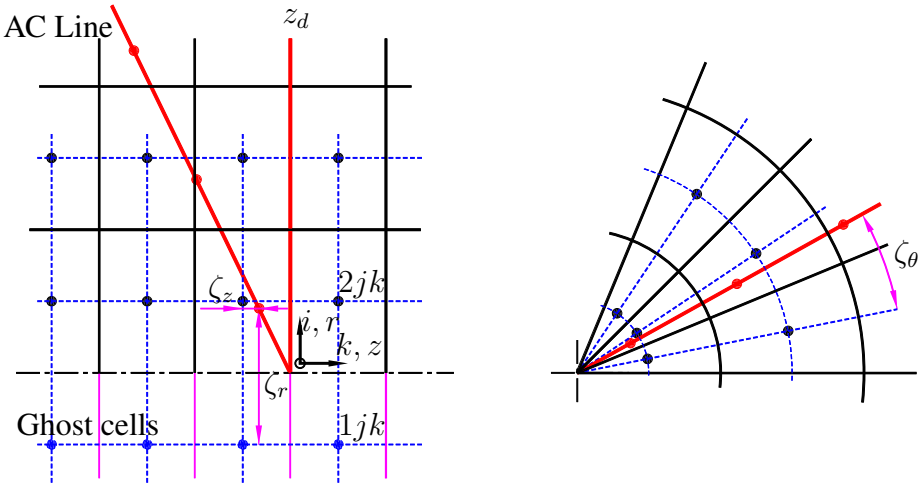

Figure 7.1: Grid structure and numbering. Velocities and pressures at points marked with red is found using linear interpolation between surrounding cell-centered values(black points).

The indices to the surrounding cell-centered points are found by first calculating

$$\boldsymbol{J}_j^{i_B} = \left[(j - \tfrac{1}{2}),\ \frac{\mathrm{N}_b \cdot B}{2\pi},\ (j - \tfrac{1}{2}) \cdot \frac{\Delta r}{\Delta z}\right] \cdot \boldsymbol{e}_{r\theta z}^{i_B} + \frac{1}{2}, \tag{7.6}$$

whereby the indices are found from

$$\boldsymbol{I}_j^{i_B} = [I_r,\ I_\theta,\ I_z] = \text{Truncate}\left[\boldsymbol{J}_j^{i_B} - \varepsilon\right] + 1. \tag{7.7}$$

Here $j = 1, J_{rot}$ and $J_{rot} = \frac{1}{\Delta r}$ is the grid point resolution of the blade in the span wise direction and N_b is the number of cells in each direction of a block , i.e. the total number of cells in each block equals N_b^3. As the EllipSys3D use a multi block technique and MPI, the lines move across

[2]The function $\tan_2^{-1}$ is within FORTRAN,atan2(y,x) defined between $]-\pi, \pi]$.

block boundaries and from processor to processor. The block and processor indices are equally identified by truncation of the interpolation indices. Using linear interpolation to find velocities along the blade $\boldsymbol{V}_j^{r\theta z}$ within each cell, the combined scheme in all three directions yields

$$\begin{array}{rll} \boldsymbol{V}_j^{r\theta z} = & \boldsymbol{V}^{r\theta z}_{I_r,I_\theta,I_z}(1-\zeta_r)(1-\zeta_\theta)(1-\zeta_z) & +\boldsymbol{V}^{r\theta z}_{I_r+1,I_\theta,I_z}\zeta_r(1-\zeta_\theta)(1-\zeta_z) \\ & +\boldsymbol{V}^{r\theta z}_{I_r,I_\theta+1,I_z}(1-\zeta_r)\zeta_\theta(1-\zeta_z) & +\boldsymbol{V}^{r\theta z}_{I_r,I_\theta,I_z+1}(1-\zeta_r)(1-\zeta_\theta)\zeta_z \\ & +\boldsymbol{V}^{r\theta z}_{I_r+1,I_\theta+1,I_z}\zeta_r\zeta_\theta(1-\zeta_z) & +\boldsymbol{V}^{r\theta z}_{I_r+1,I_\theta,I_z+1}\zeta_r(1-\zeta_\theta)\zeta_z \\ & +\boldsymbol{V}^{r\theta z}_{I_r,I_\theta+1,I_z+1}(1-\zeta_r)\zeta_\theta\zeta_z & +\boldsymbol{V}^{r\theta z}_{I_r+1,I_\theta+1,I_z+1}\zeta_r\zeta_\theta\zeta_z, \end{array} \tag{7.8}$$

where the ratios in each direction are calculated as

$$\boldsymbol{\zeta}_j^{i_B} = (\zeta_r, \zeta_\theta, \zeta_z) = \boldsymbol{J}_j^{i_B} - \text{Truncate}\left[\boldsymbol{J}_j^{i_B} - \varepsilon\right]. \tag{7.9}$$

The interpolation scheme is founded on velocities at cell centered values, in compliance with the applied flow solver the EllipSys3D code, which is a block structured FVM formulation with cell-centered velocities and pressures. The local field velocities with respect to the blades $\boldsymbol{V}_j^{stn}$ are found through the transformations

$$\boldsymbol{V}^{stn}_{j,i_B} = \boldsymbol{B\Theta^T\Phi_t\Phi_y\Theta V}^{r\theta z}_{j,i_B} = \boldsymbol{A}_{i_B}\boldsymbol{V}^{r\theta z}_{j,i_B}. \tag{7.10}$$

The combined relative velocity is given by Eq.(5.5) and the aerodynamic blade forces are calculated from Eq.(2.8) and reprojected using Eqs.(2.9) and (7.1). As mentioned, the inflow boundary conditions may be used to govern yawed inflow. Assuming that the cone angle is zero, results in $\boldsymbol{V}^{stn}_{i_B} = \boldsymbol{V}^{r\theta z}_{i_B}$ and the line positions are restricted to a plane which follow the grid structure. Although the evaluation of velocities is simplified, converged solutions are much more difficult to obtain due to the size of the grid cells at the center axis. Since $r\Delta\theta/\Delta z << 1$ for a regular grid at the center axis and the main flow direction has to be resolved here as well, time-steps have to be unrealistic small in order to obtain solutions. Skewed inflow boundary conditions have therefore not been used for simulation of yaw misalignment.

7.4 Distribution of Forces

The aerodynamic blade forces are distributed along and away from the actuator lines by forming the resulting body force by taking the convolution of the computed load $\boldsymbol{f}^{i_B}_{r\theta z}$ and the regularization kernel as described in section (3.1). Using Eq.(4.20) yields,

$$\boldsymbol{f}^{i_B}_{\epsilon} = \boldsymbol{f}^{i_B}_{r\theta z} \otimes \eta_\epsilon\,, \quad \eta_\epsilon(p) = \frac{1}{\epsilon^3\pi^{3/2}}\exp\left[-(p/\epsilon)^2\right], \tag{7.11}$$

hence, the regularized force becomes

$$\boldsymbol{f}_\epsilon(\boldsymbol{x}) = \sum_{i_B=1}^{B}\int_0^R \boldsymbol{F}^{i_B}(s)\eta_\epsilon\left(|\boldsymbol{x} - s\boldsymbol{e}^{i_B}|\right)ds. \tag{7.12}$$

The distance p^{i_B} between cell centered grid points and points on the i_B'th actuator line is given by

$$p^{i_B} = |\boldsymbol{x} - s\boldsymbol{e}^{i_B}| = \sqrt{(r\cos\theta - r_o^{i_B}\cos\theta_o^{i_B})^2 + (r\sin\theta - r_o^{i_B}\sin\theta_o^{i_B})^2 + (z - z_o^{i_B})^2}, \tag{7.13}$$

where $(r_o^{i_B}, \theta_o^{i_B}, z_o^{i_B})$ represent line coordinates. The advantages of using the convolution was explained in section (3.1). However, using the 3D Gaussian smoothing results in inconsistencies near the tip region. This may be illustrated by considering an actuator line with constant normal loading. Since the forces are distributed evenly in all three directions, forces are distributed beyond the limits of the actual tip i.e. in the tip region a constant axially loaded actuator line is represented by a span wise decreasing regularized force. In relation to investigation of the tip flow behaviour, a 2D Gaussian distribution is proposed where force is distributed in the directions normal to each line as depicted in figure 7.2. The regularized force then reads

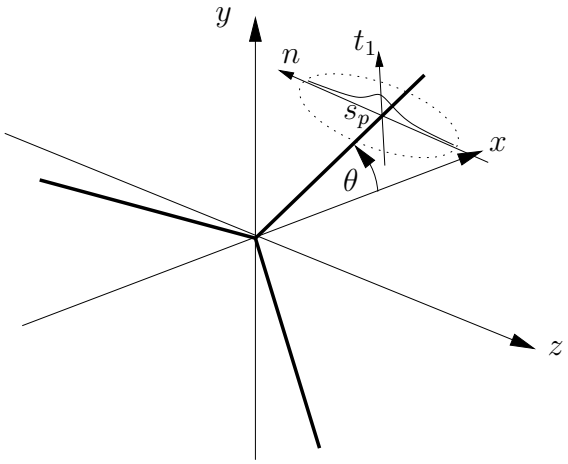

Figure 7.2: 2D Gaussian distribution of forces in a plane normal to each actuator line

$$\boldsymbol{f}_\epsilon^{i_B} = \boldsymbol{f}_{r\theta z}^{i_B} \otimes \eta_\epsilon^{2D} \,, \quad \eta_\epsilon^{2D}(p) = \frac{1}{\epsilon^2 \pi} \exp\left[-(p/\epsilon)^2\right], \tag{7.14}$$

where

$$\boldsymbol{f}_\epsilon(\boldsymbol{x}) = \sum_{i_B=1}^{B} \int_{-\infty}^{+\infty} \int_{-\infty}^{+\infty} \boldsymbol{F}^{i_B}(s) \eta_\epsilon^{2D}\left(p^{i_B}\right) dn dt_1 ds. \tag{7.15}$$

The strategy is to apply loading to all grid points having normal points s_p on the lines which may be identified from the dot product $s_p = (\boldsymbol{x}_{xyz} - \boldsymbol{x}_o) \cdot \boldsymbol{e}_{xyz}^{i_B}$. Only at points $\boldsymbol{x}$ where the value of s_p is within the range $0 \leq s_p \leq R$ is applied a regularized loading. The distance p^{i_B} between $\boldsymbol{x}$ and s_p is found as the normal distance between a point and a straight line as

$$p^{i_B}(\boldsymbol{x}) = |(\boldsymbol{x}_{xyz} - \boldsymbol{x}_o) \times \boldsymbol{e}_{xyz}^{i_B}|, \tag{7.16}$$

where $\boldsymbol{x}_o = (0, 0, z_o)$ is the position of the root center. With each line having an equidistant resolution with a distance of Δs between points and J_{rot} points, the index j is identified by truncation of $s_p/\Delta s$ and the applied forces at point $\boldsymbol{x}$ is found by linear interpolation from

$$\zeta = s_p/\Delta s - j \,, \quad \boldsymbol{F}^{i_B}(s_p) = \left[(1-\zeta)\boldsymbol{F}_j^{i_B} + \zeta \boldsymbol{F}_{j+1}^{i_B}\right]. \tag{7.17}$$

The same linear interpolation method is also applied to the 1D Gaussian distribution presented in section (3.1) for the axisymmetric Navier-Stokes method. The proposed 2D distribution is

only slightly more complicated to use than the 3D distribution. There is, however, a price to pay in terms of the discontinuity in the span wise direction which will produce numerical wiggles in the vicinity of the tip. The wiggles are partly avoided with suitable choice of ϵ. A detailed studied of the influence of the parameter ϵ is presented in Sørensen et al. [58] for the axisymmetric case, i.e. an actuator disc. Here ϵ is chosen to be of the order

$$\epsilon = \epsilon_i \sqrt{(R\Delta\theta)^2 + \Delta r^2 + \Delta z^2}, \tag{7.18}$$

and $1 \lesssim \epsilon_i \lesssim 4$.

Chapter 8

3D Simulations - Numerical Results

Whereas useful information were found by comparing results from the numerical actuator disc model with one dimensional axial momentum theory, such comparisons for the actuator line model do not provide any new information. Instead the flowfield around the Tjæreborg turbine using 2D aerofoil data is investigated as well as the optimal distribution of axial and tangential loading by Betz.

8.1 Steady Computations

To illustrate the nature of the actuator line method, representative steady numerical solutions are presented for the Tjæreborg turbine. The calculations are performed on a grid comparable to that presented in [61] with cyclic boundaries in the azimuthal direction, three blocks in the axial direction, each with $N_b^3 = 64^3$ cell's where the actuator line is resolved with 32 equidistantly distributed points. Figure 8.1 displays the (r, θ) variation of the pressure and axial velocity in the rotor plane. The obtained pressure field show contours which is slightly asymmetric with

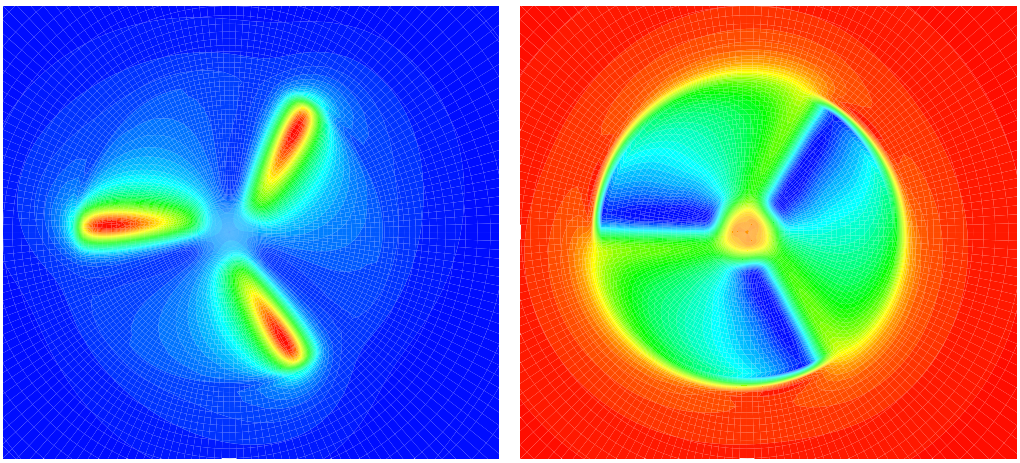

Figure 8.1: Pressure (left) and axial velocity (right) fields in the rotor plane for the Tjæreborg turbine, V_o=10m/s. Grid: 64-32 points, Re=2000. The high pressure region marked with red near the tip region has a slightly skewed shape. To the right, the axial velocity within the rotor area, is lowered drastically (green-blue) as compared to the freestream level (red).

respect to the actuator lines and for the axial velocity the contours show a sharp change near the lines. The observed fields were anticipated, however, the full three dimensional behaviour of the flowfield through the rotor is illustrated even better by displaying the shed vorticity from the blades, as shown in figure 8.2. The distinct vortex structures are preserved about $1R$ downstream

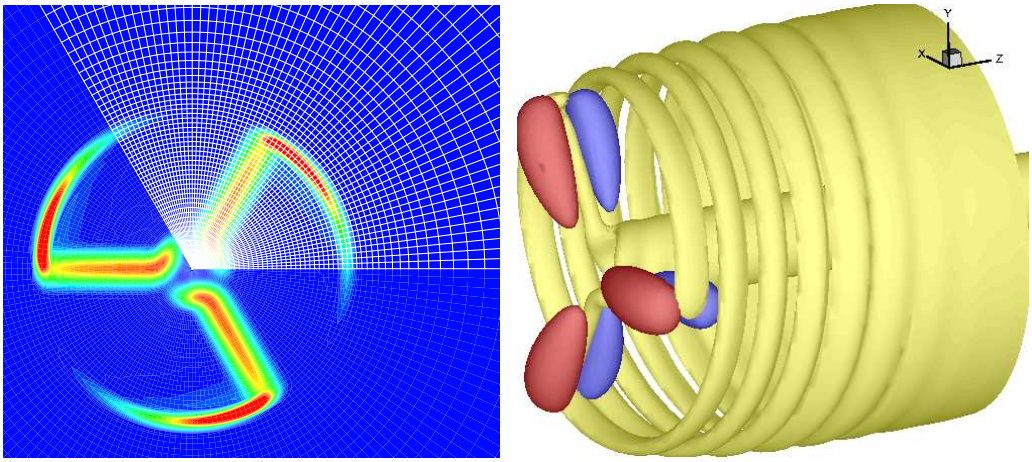

Figure 8.2: Vorticity in the rotor plane (left) and the wake vorticity structure shed from blade tip for the Tjæreborg turbine, V_o=10m/s. High and low pressure regions are marked with a red and blue contour surface infront and behind each line. Grid: 64-32 points, Re=2000

where after they smear out into a continuous vorticity sheet. The structures may be preserved even further but are smeared mainly due to grid stretching but also due to viscous diffusion. The expected expansion is also visual from figure 8.2 (right) as well as the high and low pressure regions marked with a red and blue contour surface infront and behind each line. The pressure regions represent in detail the usual pressure jump known from actuator disc methods.

8.1.1 2D-3D Regularization and Tip Correction

Calculated loadings along the lines, using the different smearing strategies discussed previously, are presented in figure 8.3. As mentioned earlier, tip correction should not be applied in connection with the actuator line concept, however, here the influence of the 2D and 3D regularization method is tested with and without the Prandtl tip correction. The 3D regularization without Prandtl correction, is seen to give a loading that increases all the way to the tip which is in contradiction to an expected continuous decreasing trend near the tip. The behaviour was explained in the previous chapter as the effect of smeared loading which extends beyond the tip and thereby alters the original spanwise loading. The 2D approach better agrees with the authors intuition that the forces should be distributed away from the lines only in the plane normal to the line. Applying the 2D approach results in a better trend near the tip, however, when comparing with results obtained with the generalized actuator disc method nearly the same results are found when the Prandtl tip correction factor is included. From the comparison it may seem obvious to include the Prandtl tip correction but since the purpose of the correction is to compensate for finite number of blades, it is inconsistent to include it as the number of blades are naturally represented by the method. Accordingly, it is chosen that the Prandtl tip correction not be included in the forthcoming results presented with the actuator line.

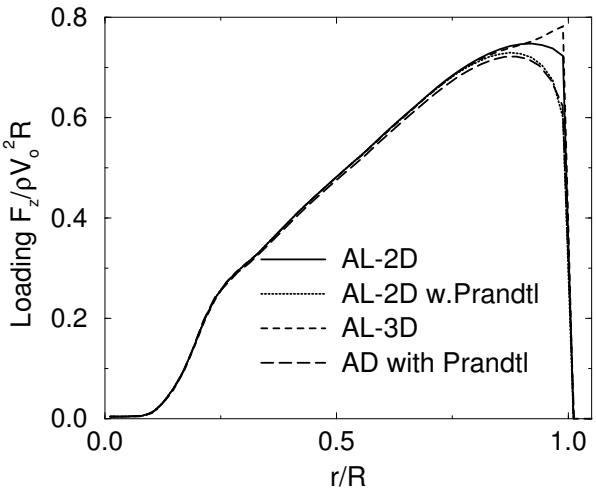

Figure 8.3: Axial loading F_z for the Tjæreborg turbine, V_o=10m/s. Grid: 64-32 points, Re=2000, $\epsilon_i = 2$

8.1.2 Simulation of the Tjæreborg

The local axial interference factor and loading displayed in figure 8.4 are compared with results obtained with the axisymmetric actuator disc model. It should be noted that the induction from the actuator disc is the circumferential averaged induction. Although the resolution is better for the actuator disc computations, the results generally compares well. The discrepancy in

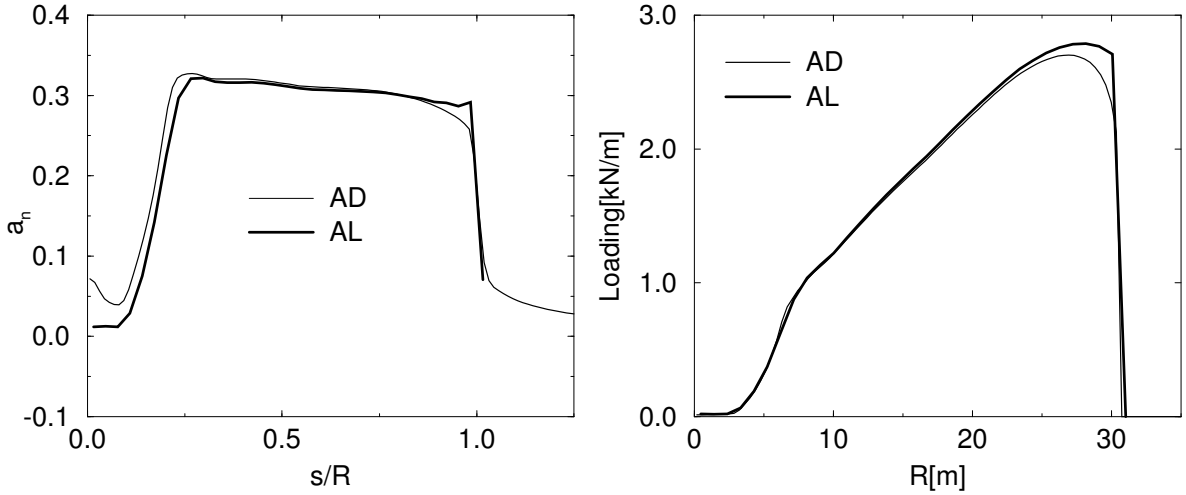

Figure 8.4: Normal interference a_n (left) and loading F_n (right) for the Tjæreborg turbine, V_o=10m/s, $\beta = 0^o$. Grid: 64-32 points, Re=2000

the tip region for the normal loading was addressed previously and is reflected in the obtained interference factor, figure 8.4 (left), which explains the differences between the to computations. The influence of the Reynolds number show similar tendencies for the two methods although the actuator line method needs a lowering in Reynolds number in order to get good convergence. A Reynolds number of Re=2000 is chosen for the presented results. The power and C_P, C_T curve (not shown) compares well with the actuator disc results but with some differences which is mainly attributed to the tip correction. An overall evaluation of the presented figures does leave the impression that a far more complicated method is not more accurate as compared with

simpler methods. The accuracy of the actuator line model is addressed in more detail later.

8.2 The Coned Rotor

Although the generalized actuator disc is able to handle coning, it is interesting to compare with a fully three dimensional analysis. Figure 8.5 depicts the vorticity contours shed from blades for a downstream coned rotor $\beta = -20^o$ (left) and an upstream coned rotor $\beta = +20^o$ (right). The high and low pressure regions marked with a red and blue contour surfaces, respectively,

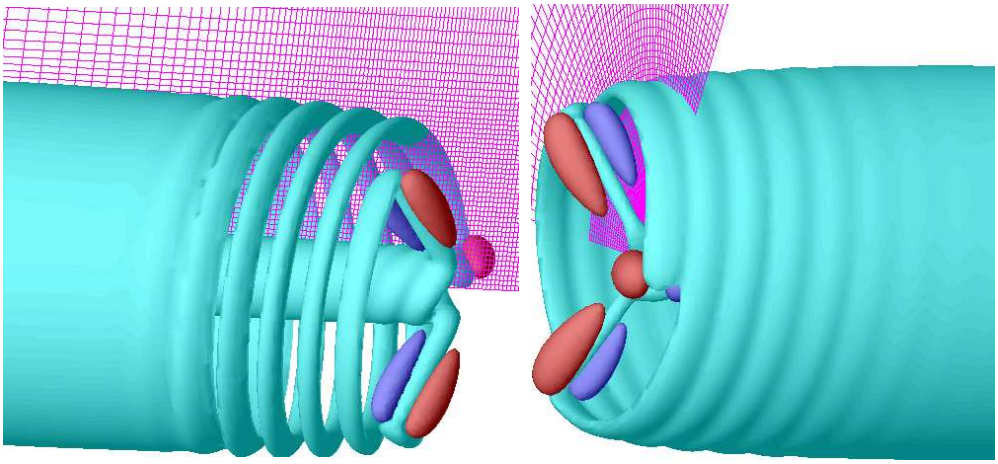

Figure 8.5: Vorticity contours shed from blades for the Tjæreborg turbine, V_o=10m/s, $\beta = -20^o$ (left) and $\beta = +20^o$ (right). High and low pressure regions are marked with a red and blue contour surface, Grid: 64-32 points, Re=2000

together with the vorticity contours give a clear impression of the flowfield through the coned rotor. Looking at the induction in figure 8.6 the trends compare, but the actuator line induction is local. Correspondingly, the normal loading, figure 8.6 (right) show resemblance between the

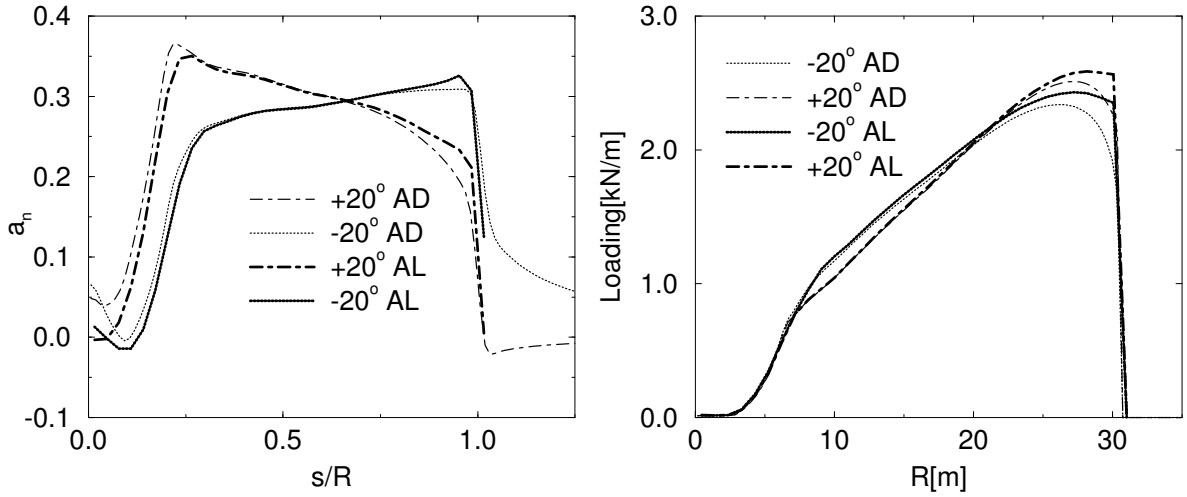

Figure 8.6: Normal interference a_n (left) and loading F_n (right) for the Tjæreborg turbine, V_o=10m/s, $\beta = \pm 20^o$, Grid: 64-32 points, Re=2000

two methods. The constant normal loaded rotor was analyzed in detail using the actuator disc

method, but as stated earlier the same analysis with a fully three dimensional method does not provide any new information. And as expected, the actuator disc method provides adequate insight to the behaviour of real turbines exposed to coning.

8.3 The Yawed Rotor

Three dimensional methods have now for some time been used to investigate skewed inflow for some time on helicopter rotors. Vortex or panel methods are are generally the first choice among researchers and designers (see Miller [41], Simoes and Graham [50], Bareiss et al. [1] or Voutsinas et al. [68]), but techniques like the asymptotic acceleration potential method by van Holten [66], adapted by van Bussel [65] to cope with flows about wind turbines, have also been used to analyze skewed inflow. The actuator line concept naturally facilitates yaw analysis (see Mikkelsen et al.[39], although no results were included) and in general 3D unsteady behaviour. Here the Tjæreborg turbine is exposed to yawed inflow for the same conditions as presented for the actuator disc using the sub models presented in appendix B. As a tradeoff between necessary computing time and resolution results in a grid composed by $9\text{x}48^3 \approx 10^6$ cells with 3 blocks in axial and 3 blocks in circumferential direction. Each rotor blade is represented by 20 spanwise points. As discussed in section 7.2 yawed inflow in connection with 3D Navier-Stokes methods may be approached in two ways, either by setting inflow boundary conditions or by yawing the rotor relative to the inflow direction which is chosen parallel to the z-axis. Initial tests to obtain numerical results by changing inflow boundary conditions did not give reliable solutions near the center axis. Furthermore convergence was bad with respect to velocity and pressure residuals. The main problem with controlling yawed inflow through boundary conditions is the degenerated grid cells at the center axis in the circumferential direction. Due to the polar grid structure the cells are extremely small in the circumferential direction and therefore sensitive to large cross flow components. It may be compensated for by using corresponding small time steps in order to obtain a reasonable CFL number (see Hirsch[27]), but as 3D methods in general are costly in computing time this is not an option. Therefore the lines are chosen to move in a fixed frame. Using the above grid and time steps of the order where the tip needs about 2-4 time steps to pass through each cell, a converged solution with a fully developed wake may be obtained with about 15000 time steps. Using one processor for each block on a SUN Fire 6800 machine, one computations takes in the order of 10-14 days. Referring to the yawed inflow conditions presented in table 5.1, figure 8.7 displays the wake vorticity structures for $\phi_y = -3$ (left) and $\phi_y = +32$ (right). The vorticity level is chosen arbitrarily to give a good visual impact of the flow through the rotor and the flow around the tower. At $\phi_y = -3^o$ the tip vorticity contours are fairly symmetrical although the tower wake disturbs the lower region. At $\phi_y = +32^o$, however, the wake region is clearly skewed and from the top and bottom of the rotor two large vortex structures are formed in the far wake. The two structures are equivalent to the well known wake behind a regular aeroplane wing, but will be even more visual at higher yaw angles. Figure 8.8 shows the calculated flap wise bending moment, Eq.(B.28), at the root section, compared with measurements and actuator disc computations. The general behaviour of the flap wise bending moment reveals an overall good prediction for the two yaw angles using both method. A slight phase shift is observed at the low point after the tower for $\phi_y = -3^o$ as compared with experimental measurements. At $\phi_y = +32^o$ the actuator line predicts slightly lower values than the corresponding actuator disc computation. Figure 8.9 displays the flowfield

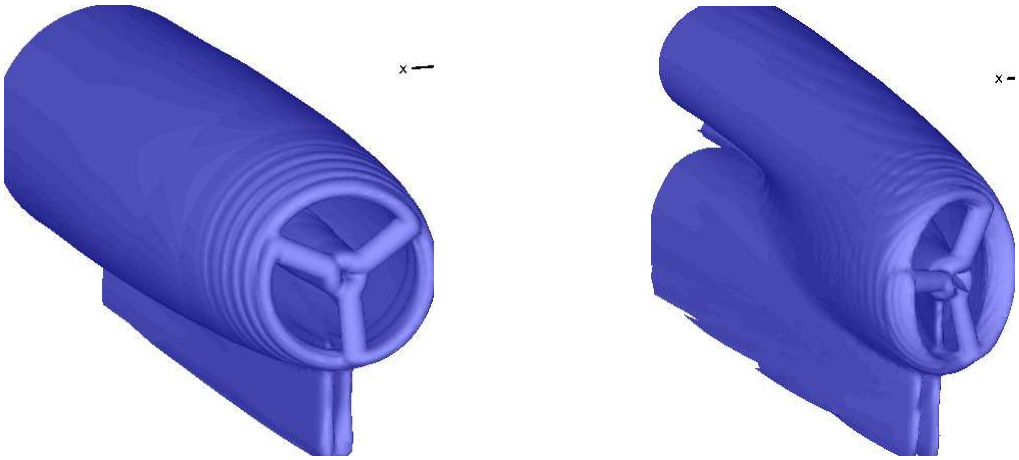

Figure 8.7: Tip vorticity contours from the Tjæreborg turbine, $\phi_y = -3^o$ (left) and $\phi_y = +32^o$ (right). Grid: 48-20 points, Re=2000

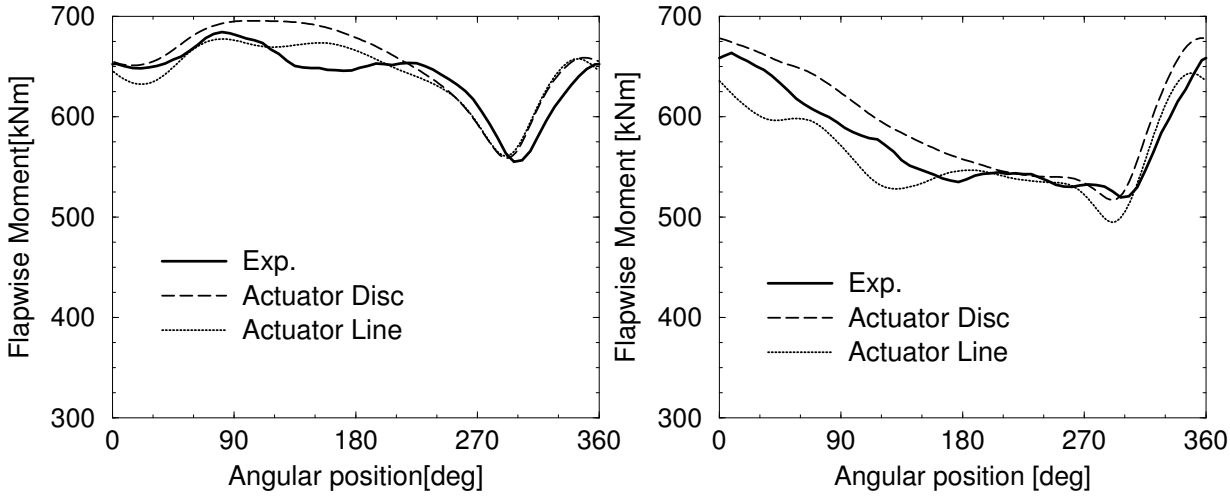

Figure 8.8: Flap wise bending moment at the root section (r=2.75) for the Tjæreborg turbine, $\phi_y = -3^o$ (left) and $\phi_y = +32^o$ (right). Grid: 48-20 points, Re=2000

at high yaw angles, $\phi_y = -51^o$ (left) and $\phi_y = +54^o$ (right). The wake region is clearly skewed in both cases with a complex structure on a local scale, however, with the two main vortex structures shed from the rotor top and bottom in the far wake. The computed structural loads are presented in figure 8.10 for the high yaw angles. For $\phi_y = -51^o$ the obtained variations capture the main behaviour as compared to experiments but no real improvement is found using the actuator line technique, which is seen to predict a somewhat lower level than the actuator disc computations. In fact, the actuator disc simulations appears to give a better prediction than the actuator line. However, at $\phi_y = +54^o$ the actuator disc over predicts by up to 30% for the main part, whereas the actuator line model generally is lower and displays better trends as compared with experiments. In [47] some discussion were addressed to the influence of the root vortex which is visible as a 'bump' in the experimental curve beginning at $\theta \simeq 160^o$. The trend is not present in the actuator disc computations but visible and somewhat exaggerated using the actuator line method. Similar observations were found using 3D free vortex wake methods [47]. Figure 8.11 shows vorticity contours for $\phi_y = +54^o$ seen from below (right)

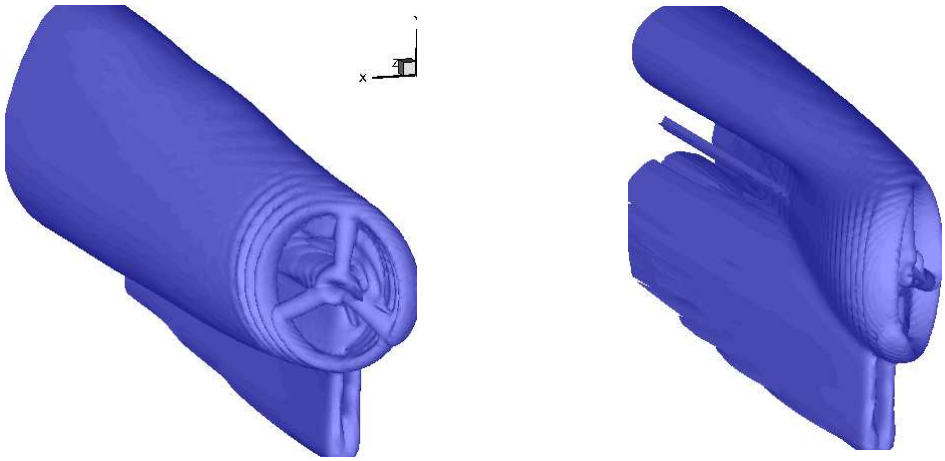

Figure 8.9: Tip vorticity contours from the Tjæreborg turbine, $\phi_y = -51^o$ (left) and $\phi_y = +54^o$ (right). Grid: 48-20 points, Re=2000

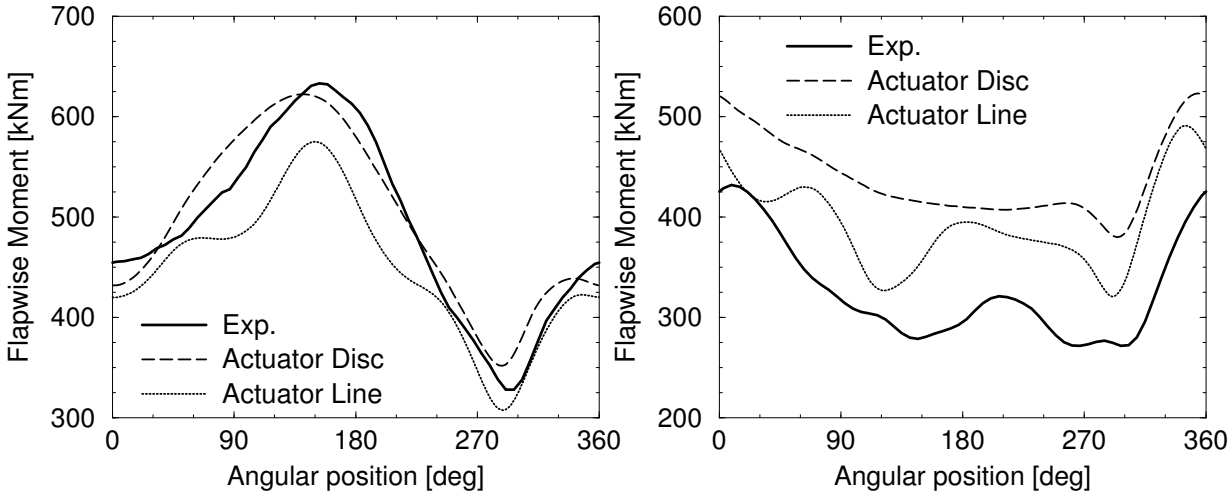

Figure 8.10: Flap wise moment at the root section for the Tjæreborg turbine, $\phi_y = -51^o$ (left) and $\phi_y = +54^o$ (right). Grid: 48-20 points, Re=2000

and infront (left). As mentioned, the wake region captured by the numerical solution tends to form two vortical structures shed from the top and bottom of highly yawed rotors, which is in accordance with the flowfield known from a wing section. Øye [75] uses skewed vortex rings distributed in the wake which in the extreme case of $\phi_y = 90^o$ yaw produces the well known downwash from an elliptic wing. The skew angle χ of the wake, which serves as an important parameter in many yaw models combined with BEM methods, is seen from below in figure 8.11 (right) but it is difficult to give a unique interpretation of χ from the calculated flowfield. Seen on the figures are also the shed vorticity from the tower. Although the tower wake resembles the flowfield abaft a cylinder, the near field is not sufficient modelled with a static actuator line applied with drag forces. As the blade lines passes the tower line, the potential flow solution around a cylinder is included into the local velocity projection.

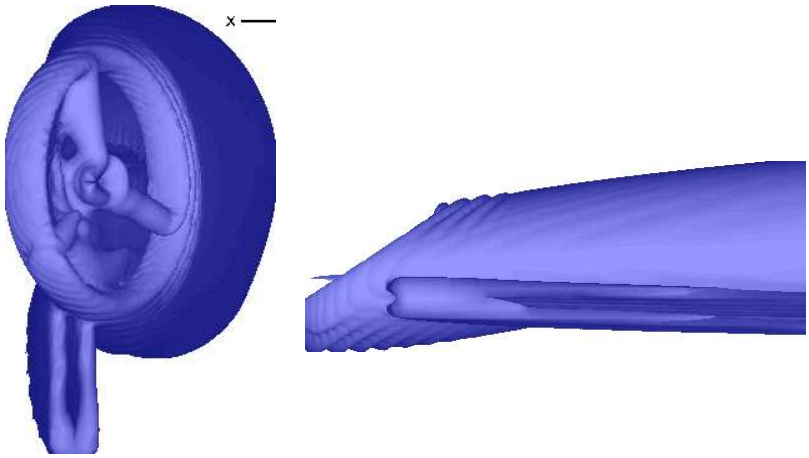

Figure 8.11: Vorticity contours for the Tjæreborg turbine, $\phi_y = +54^o$, front view (left) and from below (right).

8.3.1 Discussion

The actuator line method combined with sub models includes the full 3D behaviour of the flow through a yawed wind turbine rotor. The performance at low yaw angles are equivalent to axisymmetric aerodynamic methods, however, at the high yaw angles local trends in calculated structural loading, revealed a better resemblance at $\phi_y = +54^o$ with experiments than corresponding actuator disc simulations. The 3D behaviour of the complex wake structure is fully captured by the 3D Navier-Stokes solver, as well as local variations with respect to tower effects and aerodynamic loading. Some limitations in the accuracy can be referred to insufficient structural modelling and modelling of wind shear. Wind shear should in a future implementation be included naturally by using a Cartesian frame of reference rather than a polar. The structural modelling were limited to the blades (with some assumptions) but other components should also be included, like the movement of the tower. For the present computations the grid resolution were limited to 9 blocks with 48-20 points by the available computing capacity, but the sensitivity to grid resolution, Reynolds number and smearing of the force all have an influence which is addressed in detail later in connection with a tip correction study.

8.4 Tunnel Blockage

Tunnel blockage was treated earlier using the actuator disc method. The actuator line method facilitates investigations of rotors inserted into a tunnel to give new insight in the 3D behaviour of the flow. The effects of tunnel walls may be included using the no-slip condition but here a simple symmetry condition is used on the wall boundary equivalent to a slip condition. The present investigation is included in order to display the capabilities of the method and compare with actuator disc computations. Thus, the investigation is limited to a single case where $R_{tun}/R_{rot} = 2.5$ for the Tjæreborg turbine at $V_o = 10$m/s. The steady computation are performed on a grid equivalent to the one used for coned rotors adjusted in the radial direction to fit the tunnel aspect ratio. Figure 8.12 displays vorticity and high and low pressure contours. Whereas the vorticity field has a preserved nature the pressure contours are "reflected" on the wall thereby revealing a permanent static pressure drop across the rotor, in good accordance

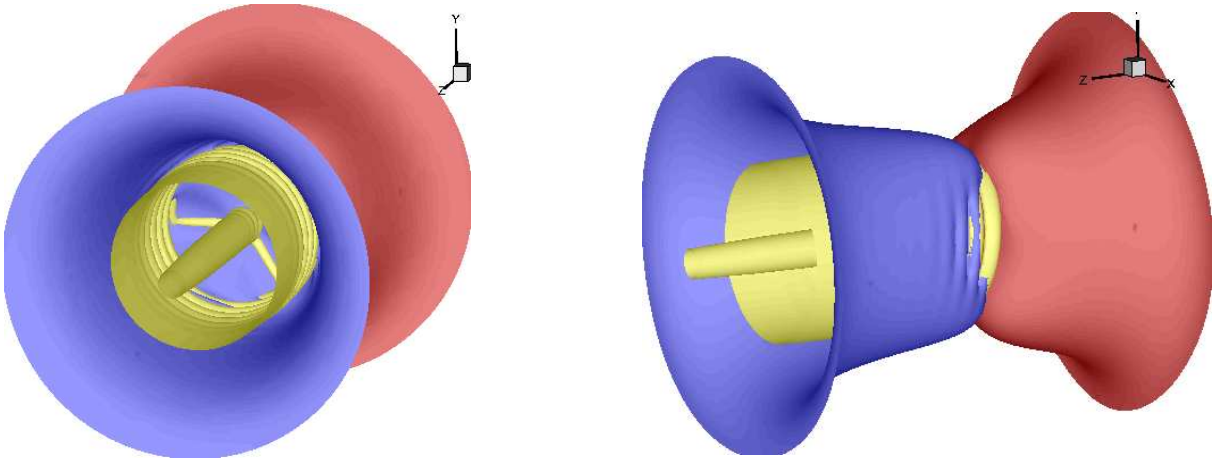

Figure 8.12: Vorticity and pressure contours from the Tjæreborg turbine inserted into a tunnel $R_{tun}/R_{rot} = 2.5$, $V_o = 10$m/s.

with actuator disc computations. The obtained force and velocity distribution are depicted in figure 8.13 compared with the actuator disc. In spite of the coarse resolution of the actuator line

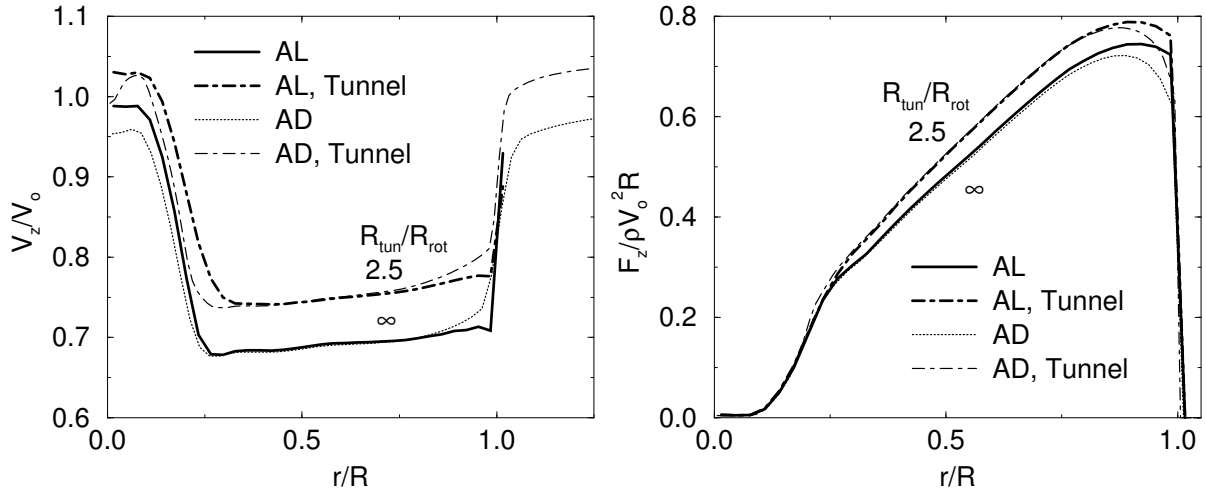

Figure 8.13: Axial Velocity (left) and force (right) distribution for the $R_{tun}/R_{rot} = 2.5$, $V_o = 10$m/s.

computations the trends resemble the axisymmetric predictions excellent. The main difference is attributed to the tip loading as seen on figure 8.13 (right).

Part D

Miscellaneous Investigations

Chapter 9

The Heavily Loaded Actuator Disc

The non-linear heavily loaded actuator disc by Wu is investigated. The formulation resembles the generalized actuator disc presented previously in many ways. The motivation for investigating the actuator disc by Wu is to develop a fast method where the entire wake is distributed without solving transport equations, however, preserving a finite difference approach.

9.1 A Distributed Wake Method

In the wake abaft an actuator disc, the angular momentum varies along a stream tube at a rate proportional to the moment of the tangential force. This result is used in the following to develop an actuator disc model where the tangential velocity is distributed in the wake combined with solution of the Possion equation (3.4) but with the right hand side derived by Wu [71], Eq.(A.51). The deduction given by Wu is presented in Appendix A.6. Restating the two governing equations, the axisymmetric, incompressible and inviscid flowfield around a heavily loaded actuator disc are governed by

$$\frac{\partial}{\partial s}(rV_\theta) = \frac{rf'_\theta}{V_s} \;\Rightarrow\; rV_\theta = f(\Psi) \text{ in the wake, } rV_\theta = 0 \text{ elsewhere} \tag{9.1}$$

$$\frac{\partial^2\Psi}{\partial r^2} - \frac{1}{r}\frac{\partial\Psi}{\partial r} + \frac{\partial^2\Psi}{\partial z^2} = (\Omega r^2 - rV_\theta)\frac{\partial}{\partial\Psi}(rV_\theta) - \frac{rf'_\Psi}{V_s}, \tag{9.2}$$

where $f'_\Psi = (V_z f'_r - V_r f'_z)/V_s$ and s refers to the stream wise coordinate in the axisymmetric plane i.e. $s \perp \Psi$. Since rV_θ is preserved along each stream tube passing through the disc it may be distributed in the wake, hence, for each stream function level in the wake the circulation is copied from the equivalent stream function level on the disc.

9.1.1 Numerical Method

Assuming that the flow is governed by the incompressible, inviscid Euler equations, the tangential momentum equation is restated from Eq.(A.24) as

$$\frac{\partial}{\partial r}(V_r V_\theta) + \frac{\partial}{\partial z}(V_z V_\theta) + \frac{2V_r V_\theta}{r} = f'_\theta, \tag{9.3}$$

where f'_θ is found from Eqs.(2.9) and (3.9). Equation (9.3) is resolved in the numerical space using the finite grid resolution $\Delta r, \Delta z$ to give the tangential velocity on the disc as

$$V_\theta \left[\frac{V_r}{\Delta r} + \frac{V_z}{\Delta z} + \frac{2V_r}{r} \right] = f'_\theta \;\; \Rightarrow \;\; V_\theta = \frac{f'_\theta}{V_r/\Delta r + 2V_r/r + V_z/\Delta z}. \tag{9.4}$$

The explicit differentiation is justified since the tangential velocity infront of the rotor is zero. Furthermore, from Eq.(9.1) the tangential velocity in the wake reads

$$rV_\theta|_\Psi^{\text{Disc}} = rV_\theta|_\Psi^{\text{Wake}} \quad \Rightarrow \;\; V_\theta^{\text{Wake}} = V_\theta^{\text{Disc}} \left. \frac{r^{\text{Disc}}}{r^{\text{Wake}}} \right|_{\Psi=\text{Const.}} \tag{9.5}$$

In order to make a fast distribution in the computational domain a transformation is introduced with the stream function as governing parameter. Assuming that the absolute value of the stream function increases continuously from the center axis to the tip of the rotor, a linearized stream function Ψ^l and corresponding radius r^l is introduced with a much veneer subdivision then Ψ and r which follow the grid size i.e $\Delta\Psi^l \ll \Delta\Psi, \;\; \Delta r^l \ll \Delta r$. Thus, the linearized stream function is designed to increase with an equidistant increment, $\Psi_i^l = i\Delta\Psi^l$. The transformation of V_θ is then basically an integration, marked with superscript ^{l}, given by

$$V_\theta^l = \int_0^R V_\theta d\Psi^l. \tag{9.6}$$

Remembering that a staggered arrangement is used, with V_θ, ω defined at cell centers and Ψ at vertices, the applied tangential velocity in the wake at a given grid cell i, j is given by the difference between equivalent stream function levels on the disc, hence

$$V_{\theta i,j} = \frac{r^l V_\theta^l(\Psi_{i+\frac{1}{2},j+1}) - r^l V_\theta^l(\Psi_{i+\frac{1}{2},j})}{\frac{1}{2}(r_{j+1} + r_j)}. \tag{9.7}$$

Since Ψ^l increase with an equidistant increment, the indices controlling the tangential velocity $V_\theta^l(\Psi)$ is identified fast by truncation of $\Psi/\Delta\Psi^l$. The same procedure is used for the case of an axially loaded rotor as the vorticity under such condition is preserved along each stream tube, which is discussed in the following section. In the computational domain the actual value of V_θ applied at the disc is set to half the value obtained from Eq.(9.4). Evaluations of the right hand side of Eq.(9.2) is performed with a second order accurate finite difference approximation of the non-linear term. The cell centered vorticity is evaluated in the wake from

$$-r\omega = (\Omega r^2 - rV_\theta)\frac{\partial}{\partial\Psi}(rV_\theta) - \frac{rf'_\Psi}{V_s} \Rightarrow \tag{9.8}$$

$$\omega_{i,j} = (V_{\theta i,j} - \Omega r_j^c)\left(\frac{r_{j+1}^c V_{\theta i,j+1} - r_{j-1}^c V_{\theta i,j-1}}{\Psi^c_{i+\frac{1}{2},j+1} - \Psi^c_{i+\frac{1}{2},j-1}} \right), \quad r_j^c = \tfrac{1}{2}(r_{j+1} + r_j), \tag{9.9}$$

where superscript ^{c} refer to the cell centered values. The last term of Eq.(9.8), $f'_\Psi = (V_z f'_r - V_r f'_z)/V_s|_{irot,j}$ has a non zero value only on the disc and is subtracted here accordingly.

9.1.2 The Axially Loaded Rotor - Constant Loading

For an axially loaded rotor $V_\theta \to 0$, $\Omega \to \infty$ and $\Omega V_\theta \to$ constant. From Eq.(A.41) with $f_r' = 0$ the r and z component reduces to

$$\frac{\partial H}{\partial r} = -V_z\omega, \quad \frac{\partial H}{\partial z} = f_z' + V_r\omega, \tag{9.10}$$

where $H = p/\rho + \frac{1}{2}V^2$ is the pressure head. By cross differentiation of Eq.(9.10) the inviscid vorticity transport equation is obtained

$$\frac{\partial f_z'}{\partial r} + \frac{\partial}{\partial r}\left(V_r\omega\right) + \frac{\partial}{\partial z}\left(V_z\omega\right) = \frac{\partial f_z'}{\partial r} + V_r\frac{\partial \omega}{\partial r} + V_z\frac{\partial \omega}{\partial z} + \omega\left(\frac{\partial V_r}{\partial r} + \frac{\partial V_z}{\partial z}\right) = 0, \tag{9.11}$$

where the expanded non-linear terms in the last bracket is reduced by using the continuity equation

$$\frac{\partial rV_r}{\partial r} + \frac{\partial rV_z}{\partial z} = 0, \quad \Rightarrow \quad \frac{\partial V_r}{\partial r} + \frac{\partial V_z}{\partial z} = -\frac{V_r}{r}. \tag{9.12}$$

Thereby Eq.(9.11) is reduced to

$$\frac{\partial f_z'}{\partial r} + V_r\frac{\partial \omega}{\partial r} + V_z\frac{\partial \omega}{\partial z} - \frac{\omega V_r}{r} = \quad \Rightarrow \quad \frac{\partial f_z'}{\partial r} + rV_r\frac{\partial}{\partial r}\left(\frac{\omega}{r}\right) + V_z\frac{\partial \omega}{\partial z} = 0. \tag{9.13}$$

Utilizing the s-transform, Eq.(A.43) gives the results

$$\frac{\partial f_z'}{\partial r} + rV_s\frac{\partial}{\partial s}\left(\frac{\omega}{r}\right) = 0 \quad \Rightarrow \quad \frac{\partial}{\partial s}\left(\frac{\omega}{r}\right) = -\frac{1}{rV_s}\frac{\partial f_z'}{\partial r}, \tag{9.14}$$

however, in the wake where there are no forces the vorticity is preserved as

$$\frac{\partial}{\partial s}\left(\frac{\omega}{r}\right) = 0. \tag{9.15}$$

This shows that the vorticity produced on the rotor disc divided with the local radius remains constant along a stream surface. Recalling figure 3.2 the vorticity produced on the edge of the disc was clearly preserved along the streamline passing through the edge. The same method applied to Eq.(9.1) is used for Eq.(9.15) to distribute vorticity in the wake where the superscript ^{l} refers to transformed values using Ψ^l. Figure 9.1 displays a schematic view of a point source at the tip of the rotor disc. The integration ensures a unique relation between the produced vorticity on the disc and the trailing vortices in the wake. The vorticity applied at cell i, j is simply found as the difference between two integrated vorticity levels as

$$\omega_{i,j} = r_j^c\left[\frac{\omega^l}{r^l}(\Psi_{i+\frac{1}{2},j+1}) - \frac{\omega^l}{r^l}(\Psi_{i+\frac{1}{2},j})\right], \quad r_j^c = \tfrac{1}{2}(r_{j+1} + r_j). \tag{9.16}$$

and since Ψ^l increases with an equidistant increment $\omega^l(\Psi)$ may be identified by truncation of $\Psi/\Delta\Psi^l$.

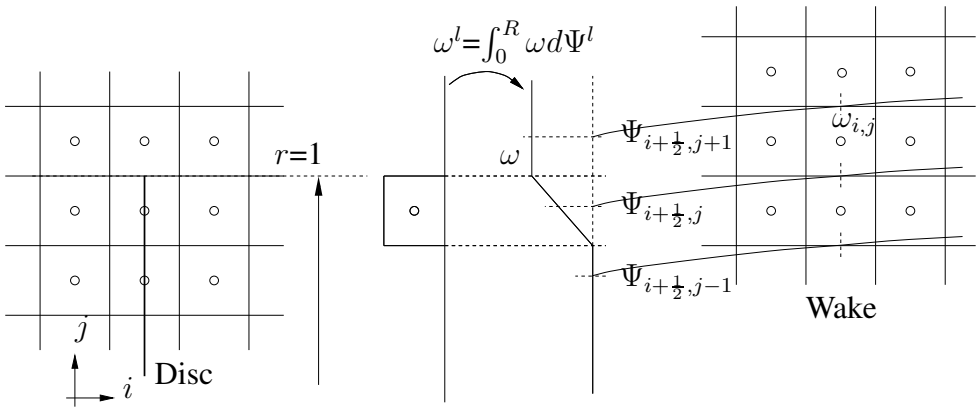

Figure 9.1: Scheme for distribution of vorticity in the wake

9.2 Numerical Results - The Axially Loaded Rotor

Considering the method of distributing vorticity as just presented, the vorticity on the disc for the constant loaded rotor disc with no rotation is evaluated from

$$\frac{\partial}{\partial r}(V_r\omega) + \frac{\partial}{\partial z}(V_z\omega) = -\frac{\partial f_z'}{\partial r}, \tag{9.17}$$

since $V_\theta = 0$. Applying explicit numerical differentiation of Eq.(9.17), since $\omega = 0$ infront of the disc, gives that the vorticity on the disc equals

$$\omega = -\frac{1}{V_r/\Delta r + V_z/\Delta z}\frac{\partial f_z'}{\partial r} \tag{9.18}$$

where the only non-zero value is at the tip. Here $\Delta r, \Delta z$ are the finite grid resolution of the disc and V_r, V_z are the cell-centered velocities through the tip. Applying the (B)-grid from section 3.2.2, figure 9.2 shows the distributed vorticity source ($C_T = 0.8$) from the tip which in the wake is divided on no more than two grid cells in the radial direction. The solution resembles

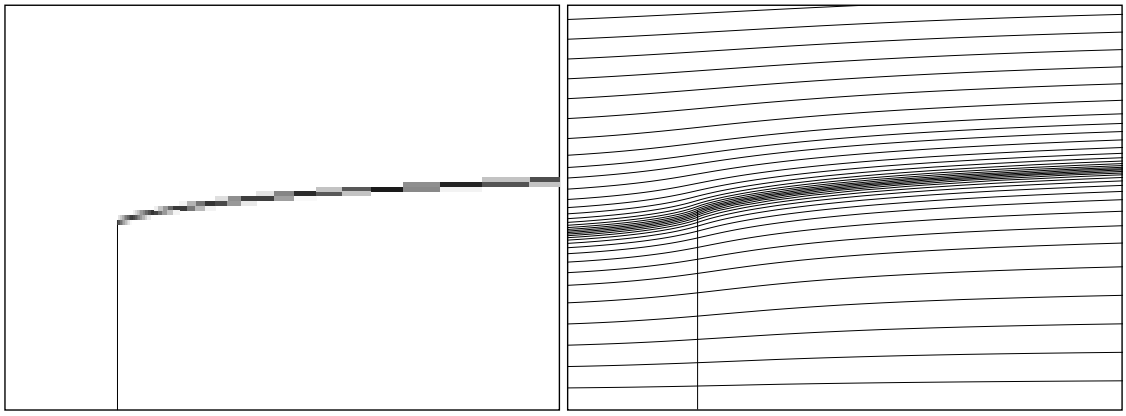

Figure 9.2: Tip-vorticity and Streamlines for a constantly loaded rotor disc, $C_T = 0.8$. The disc is inferred as a straight line

the solution displayed in figure 3.2 perfectly with the expanding wake region. Again, the disc is

inferred as a straight line. The axial interference factor shown in figure 9.3 depicts a continuous trend with increasing thrust coefficient. In the tip region the profiles change towards a peak with increasing C_T, in accordance with results obtained previously and by Sørensen et al.[58]. The

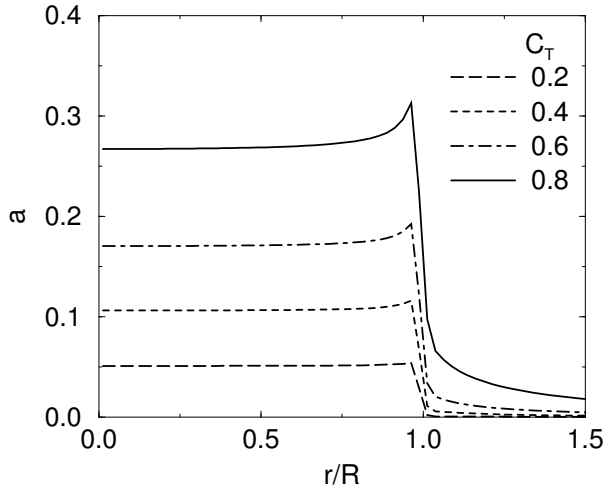

Figure 9.3: Axial interference factor a for $C_T = 0.2 - 0.8$.

integrated kinetic power coefficient for $C_T = 0.2 - 0.8$ is presented in table 9.1 and the observed results are in excellent agreement with axial momentum theory. The method, however,

C_T	0.2	0.4	0.6	0.8
Momentum theory	0.189	0.355	0.490	0.579
C_P, distributed ω	0.190	0.357	0.496	0.586

Table 9.1: Power coefficient for a constant loaded actuator disc at $C_T = 0.2 - 0.8$. The rotor disc resolved with 41 grid points.

has a limitation with respect to an upper limit on $C_T \approx 0.8$, after which converged solutions are difficult to obtain. The limit compares well with solutions obtained solving the differential transport equations presented in section (3.1). However, instead of diverging, solving the transport equations results in unsteady solutions within the range $0.89 \lesssim C_T \lesssim 1.15$, depending upon the Reynolds number. At higher C_T values separated regions begin to form behind the disc, thus the parabolized formulation begins to lose validity. Comparing the computational effort used to obtain solution with the two formulations both methods involve solution of the Possion equation. Solving the differential transport equation requires about half the effort of solving the Possion equation, whereas the method of distributing the wake is of no importance for the total computing time.

9.3 Distributed Wake Method - Numerical Results

When Wu presented his (landmark) paper numerical results were not included and to the authors knowledge numerical result for the heavily loaded actuator disc using nonlinear theory was first presented by Greenberg [22]. Streamlines for some representative loadings and the case of $C_T \rightarrow \infty$ were presented by Greenberg [22], along with profiles for the axial

velocity distribution. Here the technique of distributing the wake as presented in section (9.1) is considered for the 2MW Tjæreborg turbine. The distributed circulation field is displayed in figure 9.4 at a freestream velocity of $V_o = 12$m/s corresponding to a tip speed ratio of $\lambda_o = \Omega R/V_o = 5.89$. It is observed that on the disc the applied tangential momentum is half

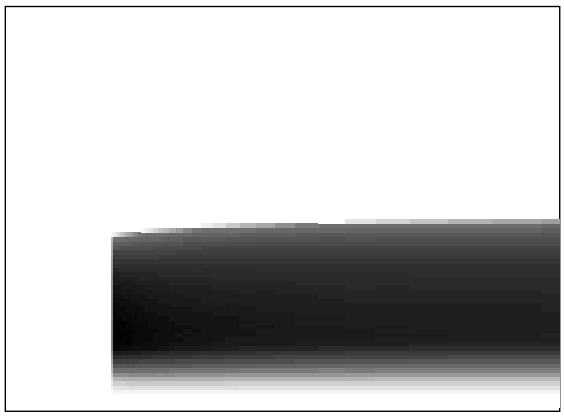

Figure 9.4: Wake distribution of circulation rV_θ, for the Tjæreborg turbine, $V_o = 12$m/s

the value applied in the wake. Evaluating Eq.(9.9) results in the vorticity field shown to the left of figure 9.5, which extends no further than the tangential velocity field in the radial direction. Figure 9.5 right, depicts the equivalent vorticity field including effects of diffusion. Comparing

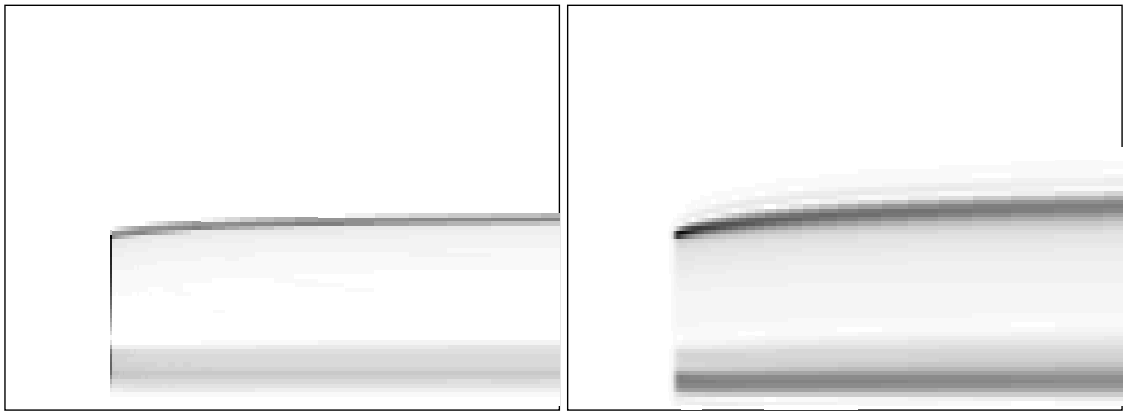

Figure 9.5: Vorticity distribution for the Tjæreborg turbine, $V_o = 12$m/s, distributed method (left) and solving the vorticity transport equation(right) where effect of diffusion is evident

the obtained a and $\lambda^2 a'$ distributions using the two methods, figure 9.6 displays an increasing difference towards the tip for a, but a far better agreement for $\lambda^2 a'$. Here the local tip speed ratio is defined as $\lambda = \frac{\Omega r}{V_o}$. Included into the plots are also a prediction computed with a "standard" BEM method which for a compares better with solving the transport equations $(\Psi - \omega)$. For $\lambda^2 a'$, however, a nearly perfect match between BEM and the distributed wake method is found. Obtained force distribution presented in figure 9.7 reveals increasing deviation near the tip between distributed wake method and the two other methods. Both the axial and tangential force distribution as well as the integrated thrust and torque, compares extremely well between

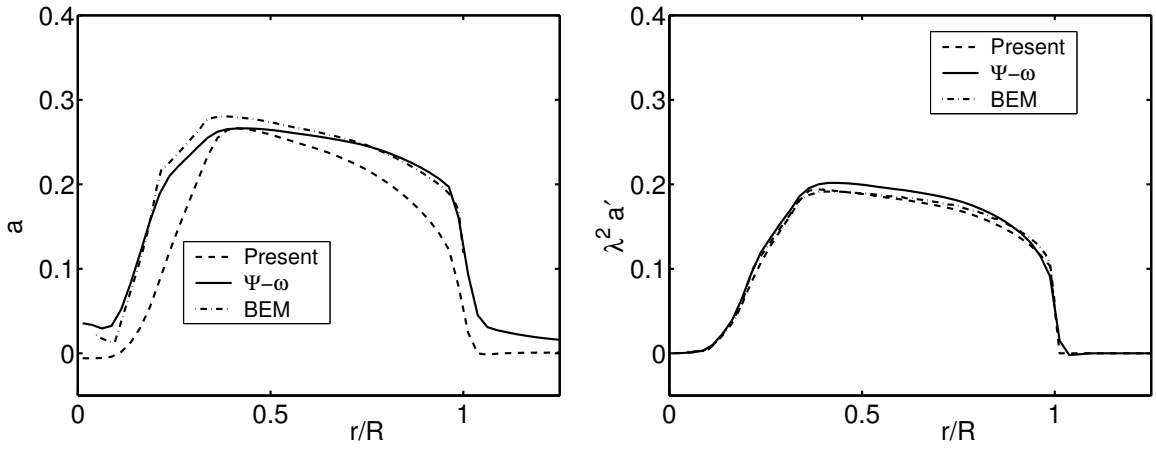

Figure 9.6: Axial interference a (left) and $\lambda^2 a'$ (right), Tjæreborg $V_o = 12$m/s, using BEM, the present distribution method and solving transport equations

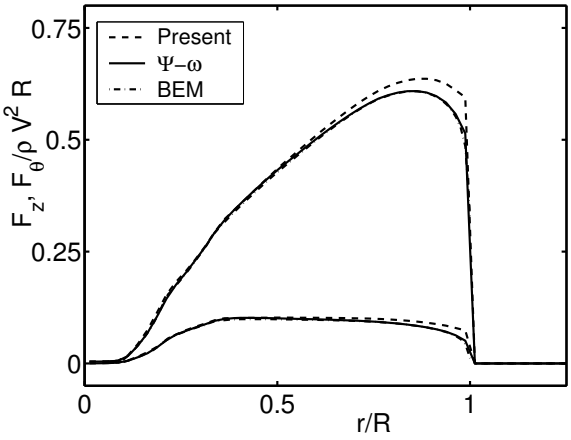

Figure 9.7: Normalized axial and tangential force distribution, Tjæreborg $V_o = 12$m/s, using BEM, the present distribution method and solving transport equations

the BEM method and $(\Psi - \omega)$.

Reviewing the result presented for the constant loaded rotor disc the method of distributing the wake is seen to have comparable accuracy to the method of solving transport equations for C_T values up to 0.8. It would have been preferable to compare the accuracy of first distributing the tangential velocity and then evaluating the right hand side of Eq.(9.2) with an analytical solution. However, the compared results for the Tjæreborg turbine at $V_o = 12$m/s together with simulation at other wind speeds (not shown) gives the clear impression that the method is less accurate than the implicit numerical formulation of the transport equations. Whether the method can be improved using numerical evaluations of higher order, has not been tested.

The two methods, which resembles each other in many ways, has comparable numerical convergence rate, although the method of distributing the wake is slightly faster. At the beginning of the study the idea of parabolizing the transport equations discussed in the previous section, had

not emerged, and as they were solved with a time consuming numerical scheme where huge time steps not were possible, the potential of distributing the wake was evident. If a choice were to be made between which method to use, the stability qualities and higher accuracy of the $(\Psi - \omega)$ formulation would be determining. Furthermore, whereas the method of distributing the wake has the limitations of finding steady solutions, the unsteady $(\Psi - \omega)$ formulation facilitates investigations of the dynamic behaviour of the developing wake.

Chapter 10

The Influence of Pressure Forces

Given the accuracy, presented in the previous chapters, of the axisymmetric Navier-Stokes formulation, the method facilitates investigations of certain basic assumptions, which form the foundation of BEM methods. Local variations are available as well as the global flow behaviour. The influence of the pressure field near the actuator disc is not taken into account in axial momentum balance, which is investigated in the following. As BEM methods are based on what happens far up- and downstream the rotor, effects of the local pressure field is neglected in contrast to the Navier-Stokes formulation, where the entire axisymmetric flowfield is determined.

10.1 Expanding Stream Tubes

Some of the basic assumptions behind BEM methods are to a certain degree incorrect, which Glauert [19] in his original work addressed explicitly. These unverified basic assumptions may be summarized as

- The flow can be divided into independent annular stream tubes
- The pressure in the ultimate wake equals the pressure far upstream
- The induced velocity in the rotor plane is equal to one half the induced velocity in the far wake
- Axial momentum theory can be applied in differential form, neglecting the resulting axial force of the pressure acting on the lateral boundaries of the stream tube
- Conservation of circulation can be ignored

The influence of pressure forces acting on the expanding stream tubes lead to the investigation presented by Sørensen and Mikkelsen [60] where the validity of the axial momentum theory was discussed, which is presented in the following. Returning to the unverified assumptions Goorjian [20] proved, in a technical note, that applying the equation of axial momentum in a simple differential form, is incorrect when the pressure acting on the lateral boundaries of the stream tubes is neglected. In most cases the inaccuracies display only negligible influence on the results when using a BEM technique, however, it is important to quantify the impact of the inconsistencies. Figure 10.1 depicts a stream surface through an actuator disc, with

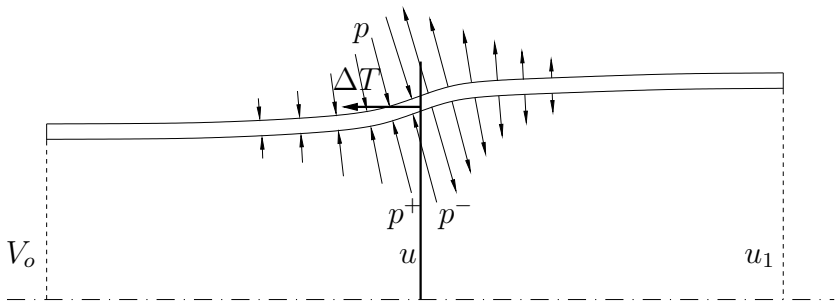

Figure 10.1: Stream tube through rotor with surface pressure acting on the control volume

the contributions from stream surface pressures acting on the control volume. As the loading increases the stream surfaces expands, causing a projected area normal to the rotor. Considering the axial momentum balance of a control volume with an axial loading ΔT on the rotor, the free stream conditions far upstream read $p = p_o, V_o = V_\infty$ and u_1, p_1 far downstream. The inviscid axial momentum balance for the control volume then reads

$$\Delta T \;=\; \Delta\dot{m}(V_o - u_1) + \Delta X, \tag{10.1}$$

where $\Delta\dot{m} = \rho u \Delta A_D$ is the mass flow and the contribution from the pressure forces, ΔX, is determined by integrating the pressure along each stream surface projected onto the axial direction as,

$$\Delta X \;=\; \int_{cs} p d\boldsymbol{S} \cdot \boldsymbol{e}_x. \tag{10.2}$$

Here $d\boldsymbol{S}$ is a differential stream surface area, $\boldsymbol{e}_x$ is the axial unit vector. The local thrust also equals $\Delta T = (p^+ - p^-)\Delta A$ and the kinetic energy converted by the rotor is given by

$$\Delta E = \tfrac{1}{2}\Delta\dot{m}(V_o^2 - u_1^2) = u\Delta T, \tag{10.3}$$

which combined with Eq.(10.1), leads to an equation for the velocity u at the disc

$$u = \tfrac{1}{2}(V_o + u_1)\left(1 - \frac{\Delta X}{\Delta T}\right). \tag{10.4}$$

The expression shows that there exist a direct relation between the error committed with Rankine-Froude theory and including pressure forces. In order to quantify the error by neglecting lateral forces, ΔX, the axisymmetric Navier-Stokes method is applied. As the pressure is absent at first in the stream function-swirl velocity-vorticity formulation, the pressure field is found by solving an additional pressure equation (see appendix A.5) based on the computed flowfield, in order to evaluate ΔX. Figure 10.2 displays the computed static pressure field for a constant loaded actuator disc, $C_T = 0.8$, in an infinite domain. In front of the disc the expected pressure build up is displayed as red contours and the negative pressure just behind the disc as blue. Towards the tip the pressure tends to zero and in the wake region the change in pressure across the vortex sheet is barely visible. Numerically, the integration of the pressure forces is evaluated, for distinct stream function levels at the disc $\Psi_{irot,j}$, and along each streamsurface as

$$P_\Psi = \int_{-\infty}^{+\infty} p d\boldsymbol{S} \cdot \boldsymbol{e}_x \Big|_\Psi \simeq \sum_{i=1}^{n-1} \tfrac{1}{2}\pi(p_{i+1,\Psi} + p_{i,\Psi})(r_{i+1,\Psi}^2 - r_{i,\Psi}^2)\;, \quad \Psi = \Psi_{irot,j} \tag{10.5}$$

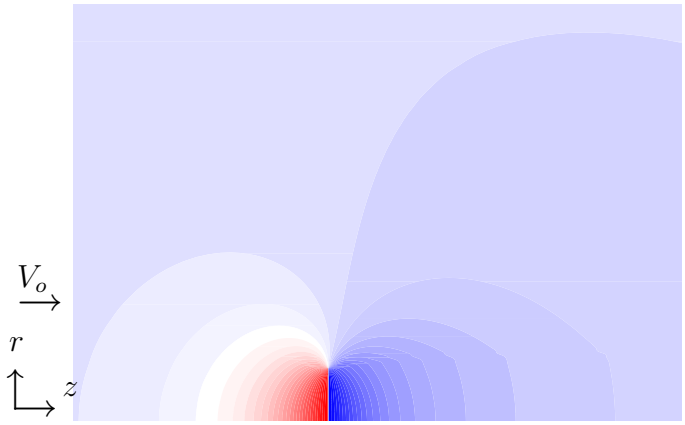

Figure 10.2: Static pressure field for a constant loaded actuator disc, $C_T = 0.8$

Figure 10.3 right depicts radial distribution of integrated axial pressure force along each stream surface for the constant loaded rotor disc, $C_T = 0.2 - 0.8$. As the stream tube surface normal has opposite direction for the upper and lower side, ΔX^s is determined as a simple difference between the two sides

$$\Delta X_j^s = -\Delta P_\Psi|_{\Psi_j} \simeq -(P_{\Psi_{j+1}} - P_{\Psi_j}). \tag{10.6}$$

Finally, the total axial pressure forces including end contributions amounts to

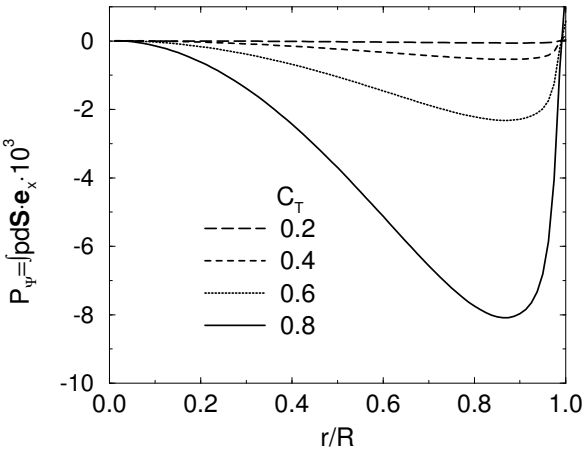

Figure 10.3: Radial distribution of integrated axial pressure force along each stream surface, $C_T = 0.2 - 0.8$

$$\begin{aligned}\Delta X_j = \Delta X_j^s \quad + \quad & \tfrac{1}{2}\pi[(p_{n,j+1} + p_{n,j})(r_{n,j+1}^2 - r_{n,j}^2) \\ & -(p_{1,j+1} + p_{1,j})(r_{1,j+1}^2 - r_{1,j}^2)] \ , \quad r, p|_{i,j} = r, p|_{i,\Psi_j}\end{aligned} \tag{10.7}$$

Returning to the axial velocity at the disc given by Eq.(10.4), the equations are rearranged and the following two error quantities introduced

$$\epsilon_1 = \frac{u}{\frac{1}{2}(V_o + u_1)} - 1 \ , \quad \epsilon_2 = \frac{\Delta X}{\Delta T}. \tag{10.8}$$

The error quantity ϵ_1 may be evaluated directly from the Navier-Stokes solution for each stream function level at the disc and in the far wake, whereas ϵ_2 is found from Eq.(10.7) divided by the local thrust ΔT. Figure 10.4 shows the distribution of ϵ_1, ϵ_2 for the constant loaded actuator disc, $C_T = 0.2, 0.4$ (left), $C_T = 0.6, 0.8$ (right). Away form the viscous layer at the tip, the

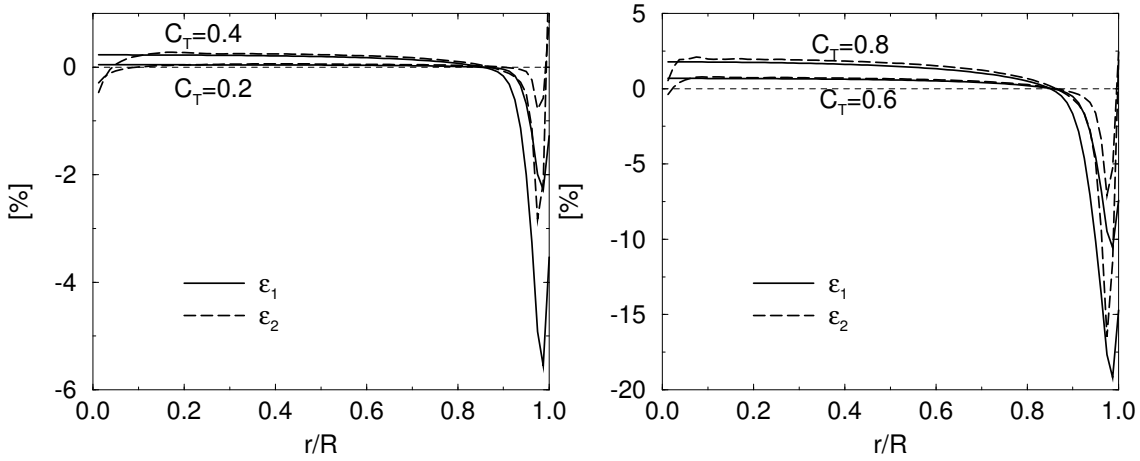

Figure 10.4: Distribution of error function along the plane for constant loaded actuator disc, $C_T = 0.2 - 0.8$

ϵ-values are close to zero. For $C_T = 0.6$ the error is less than 1% and for $C_T = 0.8$ the error amounts to about 2%. The ϵ-values are seen to match up for the main part of the actuator disc area. Viscous effects at the tip results, however, in some deviations and much higher values. With u_1 being evaluated in the far wake the Reynolds number is expected to display some influence. Here the Reynolds number is put equal to 50.000 which is relatively low. Thus, in the vorticity dominated region near the tip u_1 depends largely on the axial position. Near the center ϵ_2 is difficult to evaluate since P_Ψ is close to zero. In figure 10.5 the difference between the axial velocity and the corresponding velocity obtained from momentum theory is presented. It is observed that for $C_T = 0.8$ the difference over the most part of the rotor plane is less than

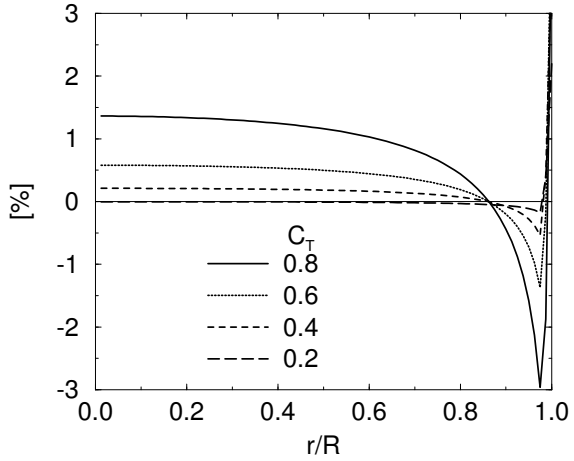

Figure 10.5: Difference between computed axial velocity and momentum theory along the plane for constant loaded actuator disc, $C_T = 0.2 - 0.8$

1.5%, although near the tip differences up to 3% exist. The presented results for the axially

loaded rotor may be extended to the general momentum theory as presented in [60]. With the introduction of the angular momentum, Eq.(10.4) may be rewritten to

$$u = \tfrac{1}{2}(V_o + u_1)\left(\frac{1-\epsilon_2}{1-\epsilon_3}\right) \ , \ \ \epsilon_3 = \frac{(p_1 - p_o) + \tfrac{1}{2}\rho(V_{\theta 1}^2 - V_\theta^2)}{p^+ - p^-}, \tag{10.9}$$

although, simulations on the Tjæreborg wind turbine revealed that ϵ_3 is negligible. The circulation, however, introduces vorticity everywhere in the wake due to the variable loading. Hence, depending on the Reynolds number, the far wake changes considerably resulting in relative high values of ϵ_1 and ϵ_2. Figure 10.6 shows velocity distributions in the rotor plane and in the far wake, for the Tjæreborg wind turbine at $V_o = 10m/s$. Included into the figure is

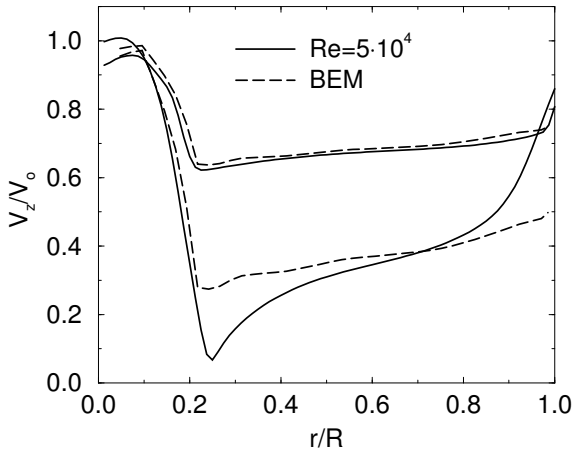

Figure 10.6: Velocity distribution for the Tjæreborg wind turbine at $V_o = 10m/s$, in the rotor plane and in the far wake

a corresponding BEM calculation which is seen to compare well at the rotor plane but rather bad in the far wake. The effect due to diffusion, is observed to change the velocity distribution continuously in the far wake.

In conclusion it has been shown that the influence of pressure forces may be analyzed in detail with good accuracy using the numerical actuator disc method. Although there are inherent inconsistencies in the BEM formulation, the errors are found to be negligible.

Chapter 11

Evaluation of Tip Correction

The tip loss effect for air-screws described by Prandtl [43] concerns the ideal rotor of Betz with optimal circulation on the blades. With the introduction of the BEM method by Glauert [19] for prediction of rotor performance, the analysis of Prandtl was adopted by Glauert. As the BEM method is based on axisymmetric momentum theory, it is inherent that the rotor disc has infinite number of blades, but since real rotors have finite number of blades real rotors have tip loss. The Glauert adoption of the Prandtl tip loss factor is generally accepted within the aerodynamic community as providing good accuracy, but as the upcoming analysis will show, some inconsistencies are inherent in the deduced expressions.

11.1 Modified Use of the Prandtl Tip Correction

To get realistic values for the performance of propellers Glauert included the tip loss effect into the BEM method as a correction to the induced velocities or interference factor, see section (4.2.1). The derived expressions for the axial and tangential interference factors by Glauert[1] are here restated as

$$\frac{a}{1-a} = \frac{\sigma C_n}{4F\sin^2\phi}\,, \quad \frac{a'}{1+a'} = \frac{\sigma C_t}{4F\sin\phi\cos\phi} \tag{11.1}$$

where F is given by Eq.(4.11). In order to satisfy the orthogonality of the induced velocity to the relative velocity, the mass flux is retained without any correction. Furthermore, a consequence of the F-function is that when approaching the tip, i.e. when $r \to R$, the axial interference factor tends to $a \to 1$, hence, the axial velocity is zero. This is inconsistent since the applied force is zero at the tip. The refined model by Wilson and Lissaman [70] applies the correction to the axial flow using the concept of circulation, but at the expense of the orthogonality between the relative and the induced velocity. The further refinement by De Vries [14] included the correction on the mass flux in the tangential momentum equation, however, the various models all lack rigorous consistency when the tip is approached. The new method by Shen, Mikkelsen, Sørensen and Bak [49] was proposed in order to overcome the inconsistency at the tip by considering the balance of momenta for a real rotor with finite number of blades, to the real aerodynamic forces. Here the real aerodynamic forces are corrected with a modified

[1] In [19] the factor F appears above the division line and not below, however, in the axial and tangential momentum equations F is multiplied which, following a rigorous deduction (see Hansen [25]), leads to Eq.(11.1).

tip correction factor F_1

$$C_n^r = F_1 C_n \ , \quad C_t^r = F_1 C_t. \tag{11.2}$$

which insures that the forces approach zero at the tip. In general, when applying 2D airfoil data, the angle of attack at the tip does not result in zero lift and drag, but physical intuition says that the forces should be zero at the tip. The proposed method is mathematically consistent and solves the problem of zero force at the tip, however, with the introduction of a new function F_1 which needs to be calibrated with experimental results. The outcome of the work presented in [49] showed some improvements in comparison with experimental results for the NREL [48] rotor. It should be noted that available experimental data generally don't have sufficient resolution[2] in the tip region to make a detailed comparison. The various methods discussed rely completely on the assumptions behind the Prandtl tip correction and in the different refinements his F function is more or less considered as a tool used to satisfy certain conditions. Whether or not the entire shape of the F function by Prandtl represents the actual physics is not an issue. In that sense it should not be forgotten that 2D airfoil data are corrected or tuned to match whatever few experimental results are available and in this process the tip correction function by Prandtl enters the tuning.

11.2 Inverse Computation of the Tip Correction Using the Actuator Line Model

The thorough treatments of the tip loss effect conducted by Prandtl, Glauert and Goldstein are based on assumptions which the proceeding analysis seeks to avoid. Using the actuator line method and solving the full 3D Navier-Stokes equations, loading is applied in an inverse manner with the results that the tip correction presents it self from the solution.

The keyword here is the free wake which is naturally inherent in the proposed method. Prandtl considered a wake structure of helical vortex sheets to be unfolded half infinite planes moving with the axial induced velocity aV_o relative to the freestream velocity. Due to the complexity, the problem was further simplified by considering the system of vortex sheets to be equidistant parallel flat plates with mutual distance $d = 2\pi R/B \sin\phi_R$ where ϕ_R is the flow angle at the tip. Based on these assumptions he deduced that the average induced velocity between two vortex sheets is reduced exponentially with the so-called Prandtl's tip loss factor F, later adopted by Glauert. The exact solution presented by Goldstein [21] to the problem where the wake has an inviscid screw surface geometry, has the inherent limitation of the fixed wake. The screw surface wake geometry, which Goldstein states is unstable, of the form

$$(r, \theta, z) = (r, \Omega t, Vt) \quad \text{or} \quad \theta - \frac{\omega z}{V} = 0 \text{ or } \pi \ , \quad 0 \leq r \leq R, \tag{11.3}$$

where V is the velocity of wake relative to the rotor, furthermore refers to lightly loaded propellers, hence, as with the Prandtl analysis, expansion is neglected. Although the optimal distribution results in angular velocities proportional to $\frac{1}{r}$ and thereby creates a spiraling vortex

[2]Experimental data obtained by the FFA [5, 46] are among the few which contain good resolution in the tip region.

with increasing strength towards the center axis, which contradicts the screw surface wake geometry, the swirl velocity is generally small for the main part of the rotor area. The solution derived by Goldstein is complicated to use in connection with BEM-formulations and for this reason rarely adopted.

With respect to the physical interpretation of the tip correction, the F factor derived by Prandtl represent a reduction factor which can be interpreted as expressing the fraction between the velocity of the trailing vortex sheets to the mean velocity of the fluid between the sheets. Thereby the F factor also represents the ratio between the circumferential averaged induced velocity to the local on the blade. The sheets applied in Prandtls analysis are half infinite vorticity sheets at a right angle which result in the well known exponential reduction function. Glauert states that in a corresponding analogy to the trailing vortex sheets from a propeller the F factor must be applied to the momentum equation. Thus, the corrected axial and angular momentum equation by Glauert are

$$\frac{dT}{dr} = 4\pi r\rho V_o^2(1-a)aF^z \ , \quad \frac{dQ}{dr} = 4\pi r^3\rho V_o\Omega(1-a)a'F^\theta, \tag{11.4}$$

where both equations formulated under the assumption of axial symmetry, include the tip loss factor $F = (F^z = F^\theta)$. As F only appears once in Eq.(11.4) the interpretation of the tip correction factor F appears to be the ratio between the circumferential averaged loading to the local blade loading i.e. assuming a uniformed induction is desired, which require a uniform loading, the loading on the blades must increase towards the tip proportional to $1/F$ i.e. $\frac{1}{F}\frac{dT}{dr} = BF_z$. This interpretation differs from initially stated. The distinction made in Eq.(11.4) between the two tip loss factors F^z, F^θ is made since the two momentum equations in principle are independent.

Here a method is proposed that seeks to find loadings which corresponds to the optimal rotor of Betz with infinite number of blades, but in principle any distribution could be applied. Thus a selected distribution of the axial induction a, number of blades B and the tip speed ratio $\lambda_o = \frac{\Omega R}{V_o}$ is chosen as reference loading. Rearranging Eq.(11.4) yields that

$$F^z = \frac{BF_z}{4\pi r\rho V_o^2(1-a)a} \ , \quad F^\theta = \frac{BF_\theta}{4\pi r^3\rho V_o\Omega a'(1-a)}, \tag{11.5}$$

where a, a' are chosen to fulfill conditions for the optimal the rotor with infinite number of blades and the loading, BF_z, BF_θ is then found from converged solutions. The conditions are governed by the orthogonality criteria of the induced velocity to the relative velocity, here given by the axial interference factors. Figure 11.1 displays the velocity triangle for a fast running rotor at the root section and near the tip region. The two figures combines to

$$\tan\phi = \frac{a'}{a}\frac{\Omega r}{V_o} = \frac{(1-a)}{(1+a')}\frac{V_o}{\Omega r}, \ \Rightarrow \ a'(1+a')\lambda^2 = a(1-a) \ , \quad \lambda = \frac{\Omega r}{V_o}. \tag{11.6}$$

Furthermore, the blade loading designed to give a minimum loss of energy E for given thrust T, is governed by the relation $dE = \Omega dQ - V_o dT$ where Q is the torque, represents the excess of the power absorbed by the rotor to the useful work done by the thrust. Thus, the best distribution (see Glauert [19]) of $a, a', B \to \infty$ giving minimum loss of energy is found from

$$\frac{\Delta(\Omega dQ)}{\Delta(V_o dT)} \Rightarrow \frac{1-a}{1+2a'} - \frac{a'\lambda^2}{1-2a} = C. \tag{11.7}$$

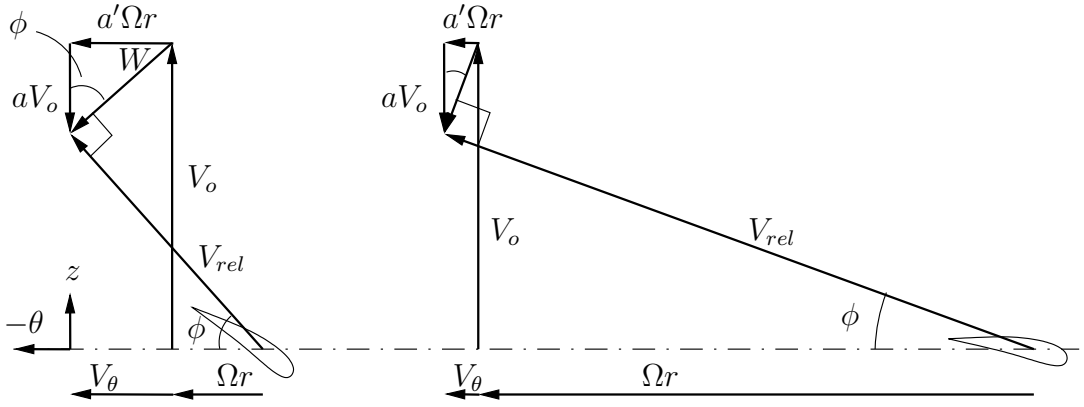

Figure 11.1: Velocity triangle for a fast running rotor near the tip region (right) and root section (left)

Equation (11.7) is solved for a by inserting Eq.(11.6) for a' and applying a Newton-Raphson method, where the constant C is fixed for a given value of a_o and λ_o at the tip. Figure 11.2 displays the radial distribution of a and $\lambda^2 a'$ obtained by solving Eq.(11.7) for $a_o = \frac{1}{10}, \frac{1}{3}$ and $\lambda_o = 3, 9$. The shape of $\lambda^2 a'$ corresponds to and approaches the level of $a(1-a)$ with

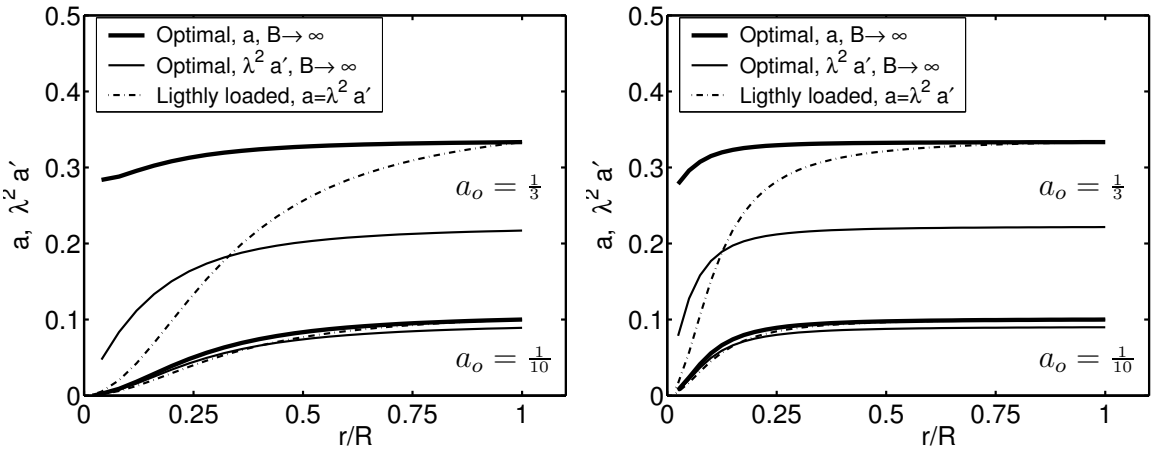

Figure 11.2: Axial interference a and $\lambda^2 a'$ for $a_o = \frac{1}{10}, \frac{1}{3}$ and $\lambda_o = 3$ (left) and $\lambda_o = 9$(right), $B \to \infty$.

increasing values of λ_o. As Goldstein [21] neglects effect of expansion the boundary conditions which govern lightly loaded rotor reduces to $a = \alpha_o \lambda^2/(1+\lambda^2) = \lambda^2 a'$ where α_o are fixed for a given value of a_o and λ_o at the tip. The agreement with the optimal distribution of Betz is reasonable good for $a_o = \frac{1}{10}$ and rather bad for $a_o = \frac{1}{3}$. Here the distribution of Betz is used in the inverse study of the tip-correction. In order to obtain solutions with the actuator line method fulfilling the above conditions, the loading is applied iteratively using a relaxation method

$$F_z^{k+1} = F_z^k + (a - \overline{a}) r K_z \,, \quad F_\theta^{k+1} = F_\theta^k + (a' - \overline{a}') \Omega r K_\theta \tag{11.8}$$

where K_z, K_θ represent relaxation parameters and $\overline{a}, \overline{a}'$ are the measured distributions along the line for each iteration. The method insures a smooth convergence.

The proposed method could be combined with other free wake methods based on first principles such as vortex methods. Fixed and free wake methods have been developed where the vorticity is distributed either as vortex line elements (Miller [41], Simoes and Graham [50], Bareiss et al. [1]) or as discrete vortices (Voutsinas et al. [68]). A fixed wake analysis would provide comparable results to that of Goldstein [21] whereas a free wake analysis would include expansion and the true dynamic behaviour of the wake. Free wake methods tends, however, to diverge owing to intrinsic singularities of the vortex panels in the developing wake.

11.3 Numerical sensitivity - The 2 Bladed Rotor

The numerical validation of the actuator line method presented in Sørensen and Shen [61], was performed using LM 19.5 blade data. The blade is shaped with a chord wise distribution that decreases continuously towards the tip to a peak, which result in a smooth decreasing loading at the tip and thereby less influence of the tip vortex. Some rotors, like the Tjæreborg turbine, has a more abrupt ending at the tip, hence producing a much stronger tip vortex. Thus, using the actuator line concept on a turbine with a high loading near the tip, results in a much stronger edge singularity at the tip, which is investigated in the following.

In [61] the forces were applied using the 3D-regularization function which smears the forces equally in all direction, and thereby also in the span wise direction. The 3D-function is not applicable in relation with a tip-correction study since when applying Eq.(11.8) a span wise smearing of the loading will results in solutions with peaks near the tip. This may be realized by considering a constantly loaded actuator line. Using the 3D-function the last point at the tip has less loading than the second point from the tip since each point shears loading with neighbouring points. On a local scale this is inconsistent in the tip region although on a global scale the total amount of applied force is preserved. The main drawback of using the 2D approach is the partly unknown influence of the spanwise singularity at the tip, however, as 2D-regularization only smears is in the direction normal to each actuator line, it is chosen for this analysis.

The two main parameters governing the numerical accuracy of the actuator line method are regularization parameter ϵ and grid resolution, as with any numerical method. Applied diffusion represented by the Reynolds number Re has a minor influence on the solution if the Reynolds number is big. The Reynolds number is set to Re=10.000, which in some cases gives an irregular convergence. Ideally forces should be distributed over an area comparable to the chord distribution and if possible resemble the chord wise pressure distribution. Presently realistic grid resolutions are by far to coarse to resolve the chord wise pressure distribution for a modern wind turbine blade, however, for rotors with higher solidity, like hydrodynamic propellers, it should be applied.

Considering a lightly loaded rotor with an optimal distribution for tip-speed-ratios $\lambda_o = 3,9$ and $a_o = 0.1$ at the tip, loading is applied according to Eq.(11.8). The domain extends about $10R$ upstream, $15R$ downstream and $8R$ in the radial direction. Figure 11.3 depicts the influence of ϵ on the average axial interference factor for a grid with 44 equidistantly distributes points resolving the rotor and 80 points in total in the span wise direction, stretched away from

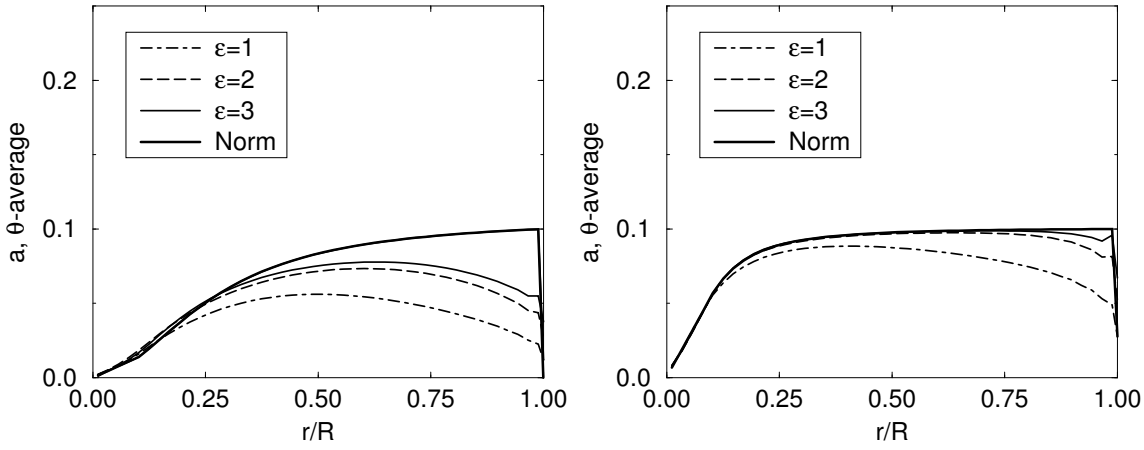

Figure 11.3: Axial interference on the line (norm) and circumferential average, for different ϵ values, $\lambda_o = 3$ (left), $\lambda_o = 9$ (right), $a_o = 0.1$, Grid: 80-44 points, Re=10^4

the tip. The obtained distributions displays a significant dependency on the smearing factor ϵ. Furthermore, the nominal loading on the actuator line compares reasonable with average values for $\lambda_o = 9$ but deviates considerable for $\lambda_o = 3$, thus illustrating a less axisymmetric behaviour at lower tip speed ratios, hence, a more pronounced tip effect at $\lambda_o = 3$. Evaluation of the tip loss is presented and compared with Prandtl and Goldstein in figure 11.4, keeping in mind that the comparison with Goldstein is not for the exact same distribution. Although the trends

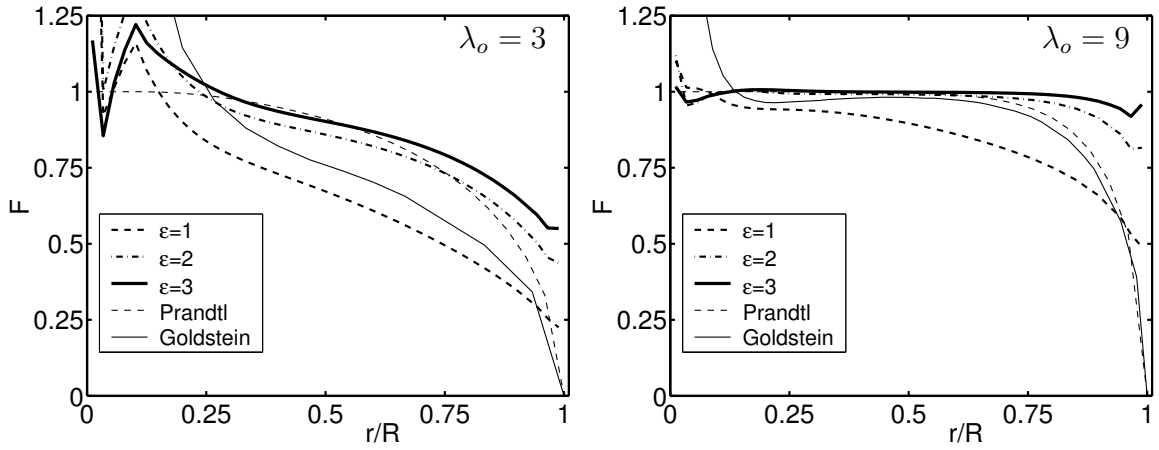

Figure 11.4: Tip loss distribution F, ratio between the circumferential average induction a and the local on the line for different ϵ values, $\lambda_o = 3$ (left), $\lambda_o = 9$ (right), $a_o = 0.1$, Grid: 80-44 points, Re=10^4

are captured, the results reveal significant discrepancies and dependent behaviour of the smearing function. Figure 11.5 depicts a different approach where loading is applied according to Eq.(11.4) with $F^z = F^\theta = 1$, $\lambda_o = 9$, $a_o = 0.1$. In this way a unique loading is insured. The interference along the line, shown to the left, deviates significantly for $\epsilon = 1$ as compared to higher values of ϵ and the circumferential average. The circumferential average, shown to the right, is nearly unaffected which suggest that the global balance is preserved for $\epsilon \geq 1$. Locally, however, the dependency must be taken into account. The nominal or optimal loading is also

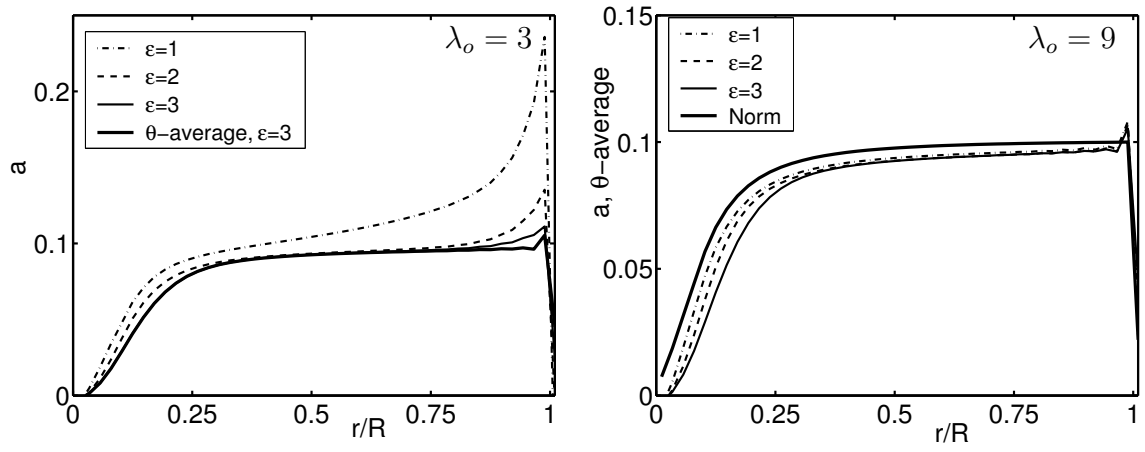

Figure 11.5: Axial interference a on the line (left) and circumferential average (right) for different ϵ values, $\lambda_o = 9$, $a_o = 0.1$, Grid: 80-44 points, Re=10^4

included into the plot which is slightly higher than the circumferential average. The tangential component displayed in figure 11.6 left, shows the same tendencies as for the axial component. The distributions tends towards the circumferential average with increasing ϵ and the same cir-

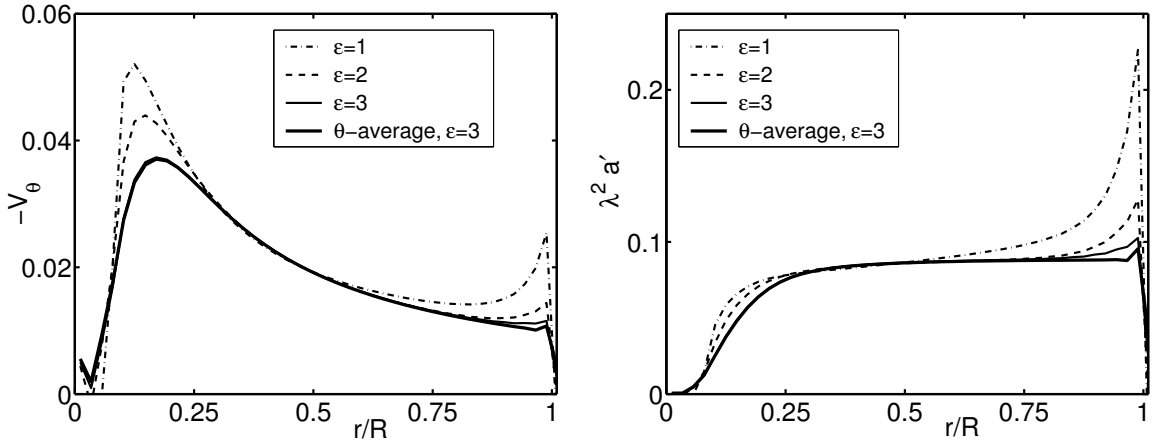

Figure 11.6: Tangential velocity (left) and $\lambda^2 a'$ (right) on the line for different ϵ values, Grid: 80-44 points, Re=10^4

cumferential average values for V_θ were obtained (not shown) for the considered ϵ-values, just as for the axial interference. The quantity $\lambda^2 a'$, shown to the right, displays the convergence even better although in the tip region there remains an effect for $\epsilon = 3$. Looking at the azimuthal variation of a and $-V_\theta$ at 80% radius figure 11.7, reveals a strong dependency near the actuator lines at $\theta = 90^o$ and 270^o for the axial interference, shown left. The variation of tangential velocity is more harmonic for $\epsilon = 2, 3$, however $\epsilon = 1$ produces spatial oscillations in the vicinity of the lines. Based on the presented figures $\epsilon \geq 2$ gives solutions without the oscillations and for $\epsilon = 3$ circumferential averaged profiles nearly match profiles extracted along the line. Next, the grid dependency is investigates for the same loading and using $\epsilon = 2$. Figure 11.8 shows the axial interference a on the line (left) and circumferential average (right) for grid resolutions 80-44, 64-32, 48-20 and 32-12 points in total and resolving the rotor, respectively. The tendency

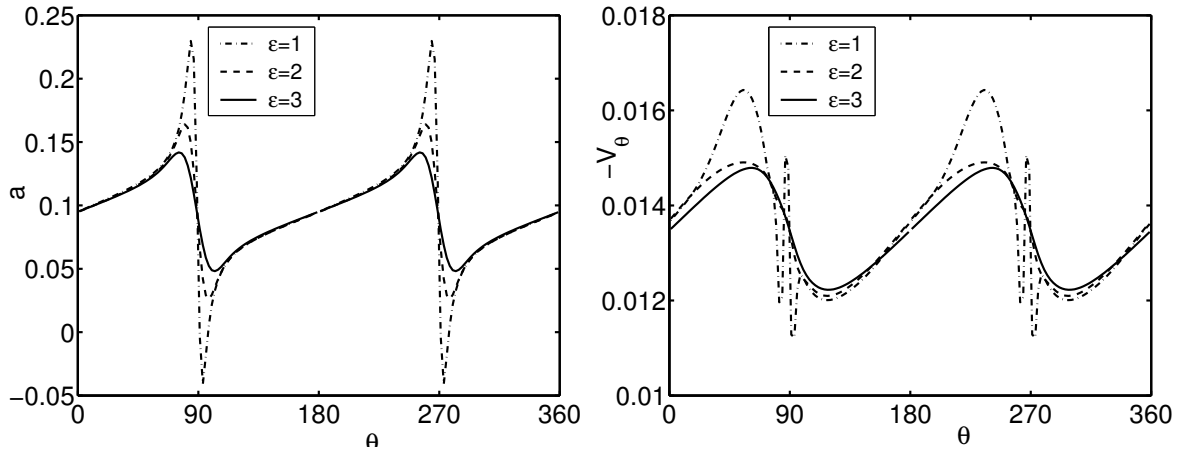

Figure 11.7: Axial interference a (left) and tangential velocity (right) at 80% radius for different ϵ values, Grid: 80-44 points, Re=10^4

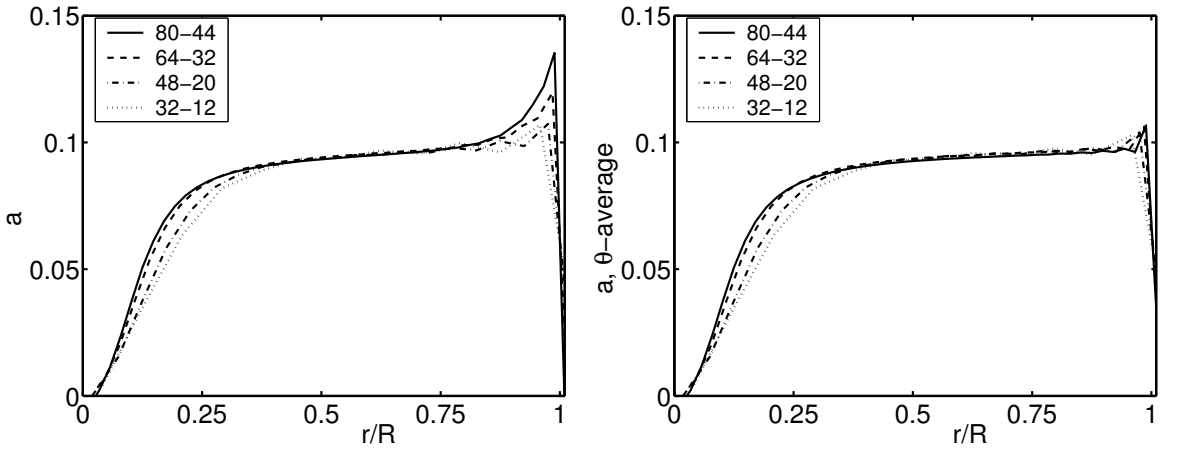

Figure 11.8: Axial interference a on the line (left) and circumferential average (right) for different grid resolutions, $\epsilon = 2$, Re=10^4

near the tip displays increasing spatial oscillations with decreasing grid resolution which is expected since the loading at the edge is singular with respect to the span wise direction. The peak in the solution near the tip will keep on increasing with better grid resolution which makes it difficult to interpret when or if adequate grid independence is obtained. The behaviour at the tip is critical to the study of tip correction since it governs the entire shape of the loading, and the solution procedure given by Eq.(11.8) will include the dependency of grid resolution and regularization parameter ϵ. The tangential component given in figure 11.9 reveals similar patterns to that of the axial interference in the tip region. The effect of refining the grid is comparable to decreasing the ϵ parameter which can be deduced from the presented figures. Figure 11.10 shows the effect even better. The azimuthal variation of a at 80% radius shows growing peaks with increasing resolution whereas V_θ converges towards a higher level. In terms of evaluating 3D grid independence, regularization parameter, the presented figures displays trends towards independent solutions with increasing resolution and ϵ. Using the current grid configuration, higher resolutions are possible but very time consuming and therefore not conducted. Choosing

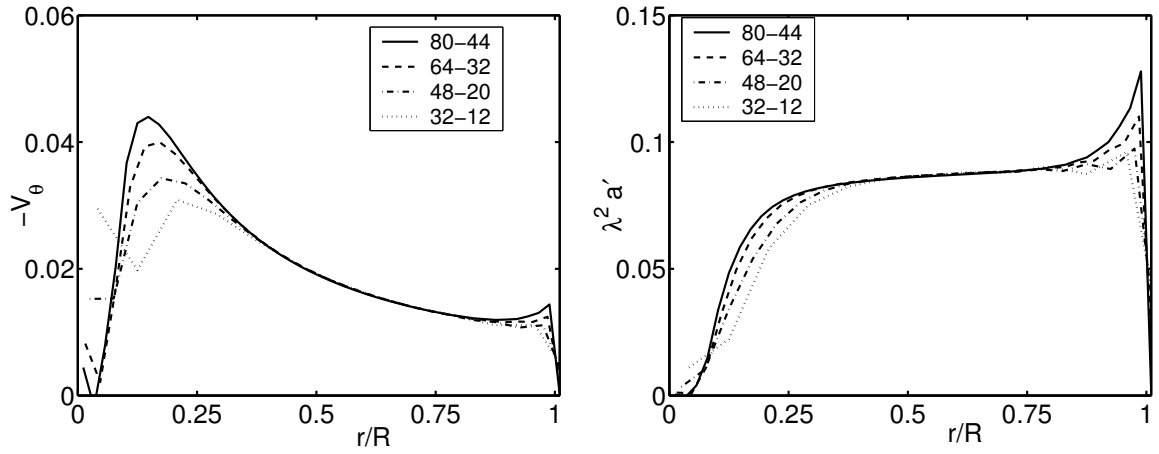

Figure 11.9: Tangential velocity (left) and $\lambda^2 a'$ (right) on the line for different grid resolutions, $\epsilon = 2$, Re=10^4

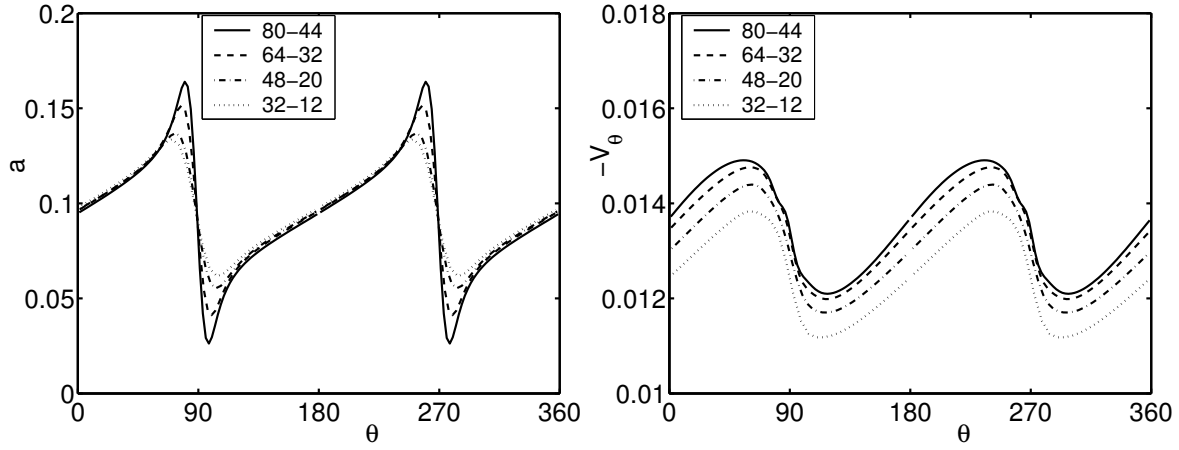

Figure 11.10: Axial interference a (left) and tangential velocity (right) at 80% radius for different grid resolutions, $\epsilon = 2$, Re=10^4

higher ϵ-values is non-desirable in terms of preserving the concept of actuator lines, but on the other hand smooth solutions are obtained with increasing ϵ. Presently, it is questionable whether sufficient accuracy may be obtained using the applied solver and distributions technique. The computations are, however, carried out in order to display what kind of trends can be expected by evaluating Eq.(11.5) using the finest grid and using $\epsilon = 3$.

11.4 Tip correction - The 2 Bladed Rotor

The 2 bladed rotor is considered for four different loadings. First, the lightly loaded rotor with optimal distribution for $\lambda_o = 3,9$ and $a_o = 0.1$ at the tip and second, the optimal rotor with optimal distribution $\lambda_o = 3,9$ and $a_o = \frac{1}{3}$ at the tip. Loading is applied iteratively according to Eq.(11.8). The derived solution by Goldstein is based on different types of Bessel functions.

Numerical results were included in [21] for the two and four[3] blade rotor for the quantity,

$$\frac{B\Gamma\Omega}{2\pi V_o v'} = \frac{\lambda^2 F}{1+\lambda^2} \tag{11.9}$$

for $\lambda_o = 2-10$, $B = 2$, where Γ is the circulation and v' the velocity of the trailing vortex system. Figure 11.11 depicts a comparison with Prandtl[4] and Goldstein for the lightly loaded rotor $a_o = 0.1$(left) and the optimal rotor $a_o = \frac{1}{3}$(right). Also $B \to \infty$ is included. For

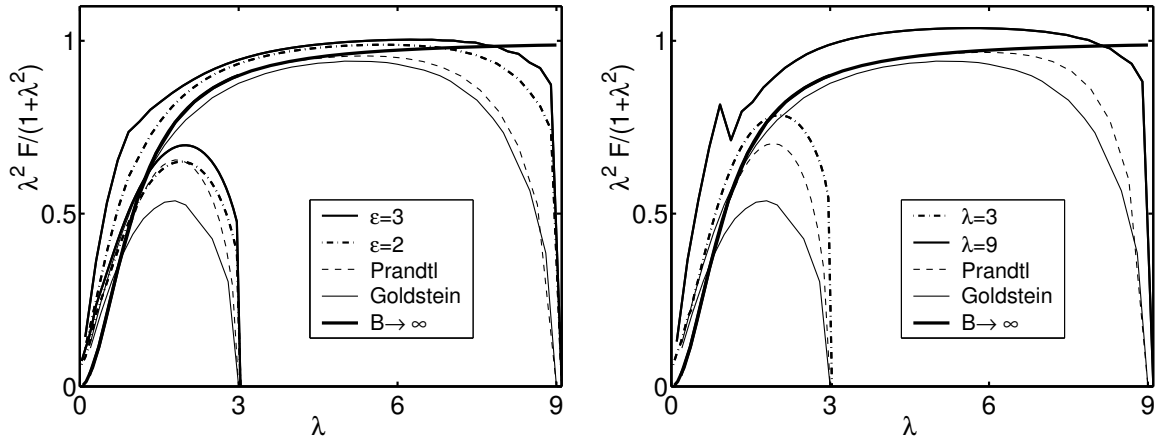

Figure 11.11: Relative blade loading $\lambda^2 F/(1+\lambda^2)$ for rotor with optimal distribution, $B = 2$, $a_o = 0.1$ at the tip to the left, $a_o = \frac{1}{3}$ to the right

$a = 0.1, \epsilon = 3$ the prediction is everywhere above both Prandtl and Goldstein. Although the wake geometry resembles the screw surface geometry, the disagreement is severe and whether a closer comparison to Goldstein can be expected is difficult to say since the foundation of the two methods are different. Using $\epsilon = 2$ lowers the prediction about 10% over the entire span, however, for $\lambda_o = 9$ the difference is confined to the tip region. Moreover, for $\lambda_o = 9$ the solution is above $B \to \infty$ for the main part. Figure 11.11 right, $a_o = \frac{1}{3}$, shows an increasing tendency which referred to an effect of the increasing expansion. Figure 11.12 and 11.13 displays the F-function directly for the same cases. The differences in level for $\lambda_o = 3$ are seen to be significant although the overall shape of the F-function for the actuator line method compares better with the Goldstein result. For $\lambda_o = 9$ the F-distribution approaches unity for both $a_o = 0.1$ and $a_o = \frac{1}{3}$, however, for a large part F is above unity. Near the tip F decreases as expected, but the comparison with Prandtl shows significant differences. The dependency or sensitivity to the ϵ parameters seen in figures 11.11 and 11.12 left, raises the question whether the method is suitable to accurately determined tip correction factors and what improvements are feasible to increase accuracy.

11.4.1 Uncertainty About Accuracy

The method of determining the tip-correction factor in an inverse manner is believed to be correct and will produce accurate results using an appropriate 3D Navier-Stokes solver. As the flow

[3] Table II and III in [21]

[4] In order to compare the Prandtl tip loss factor F without expansion to Goldsteins result the following notation was used $F = \frac{2}{\pi}\cos^{-1} e^{-f}$, $f = \frac{B}{2}(1-\frac{\lambda}{\lambda_o})\sqrt{1+\lambda_o^2}$ in [21].

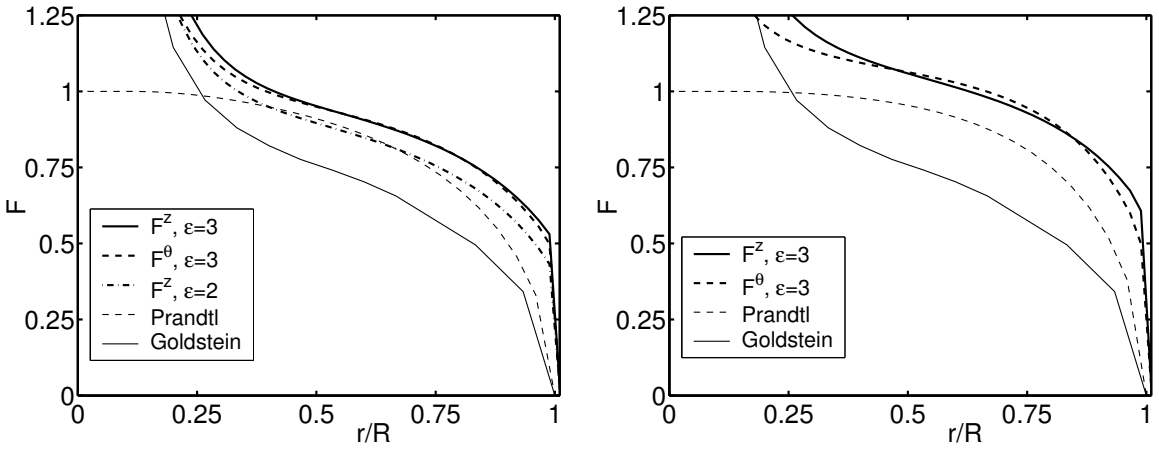

Figure 11.12: Tip correction factor F for a rotor with optimal distribution, $B = 2$, $\lambda_o = 3$, $a_o = 0.1$ (left), $a_o = \frac{1}{3}$ (right)

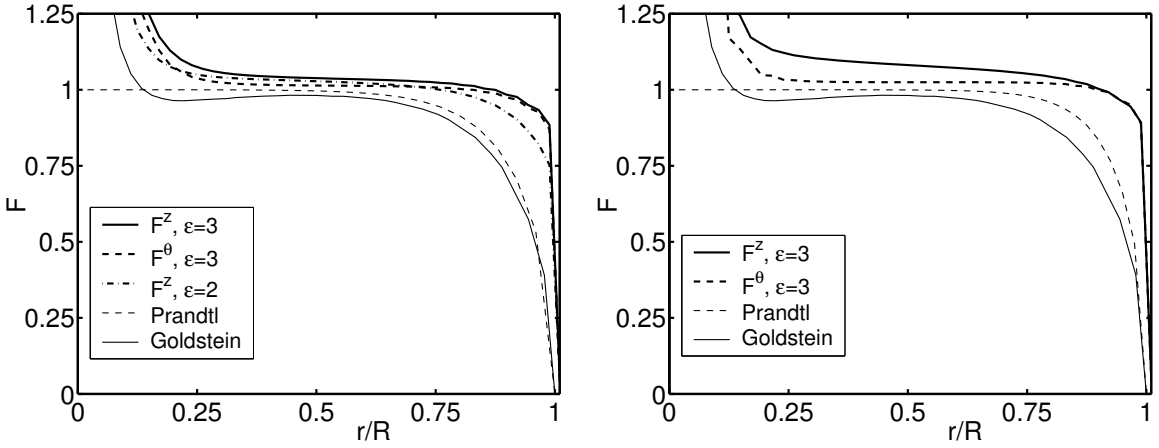

Figure 11.13: Tip correction factor F, $B = 2$, $\lambda_o = 9$, $a_o = 0.1$ (left), $a_o = \frac{1}{3}$ (right)

is a fully 3D flow and has a strong vortex structure it is anticipated that numerical independent solution may be difficult to obtain. The obtained results for the different cases clearly showed comparable trends but the levels compared rather bad with the theories of Prandtl and Goldstein. Although the shape of the presented distributions are comparable, the computed levels differs by up to 50% for the low tip speed ratios. At $\lambda_o = 9$, which corresponds to the values used for the yaw calculations presented in section 8.3, the F function is close to unity for the main part and therefore less influential on the solution. As the foundation of the method is a velocity-pressure formulation of the Navier-Stokes equations, questions arises whether the method is feasible for resolving the vortical tip structure which in principle is singular. From inviscid theory is well known the strength of the tip vortex should be preserved to the ultimate wake. It is, however, difficult to accurately measure how well they are preserved although a rough estimate of the integrated tip vorticity across an area which covers the concentrated tip vortex (not shown), reveals that the level is preserved about one turn whereafter the grid expands hence making it impossible to evaluate. Based on the presented results, the applied forces as distributed cell centered sources combined with a finite volume formulation of the Navier-Stokes equations does

not seem to insure sufficient accuracy in the vicinity of singularities. With respect to the applied pressure solver in the EllipSys3D, the implementation only allows assignment of cell centered sources, however, techniques based on distributed pressure discontinuities as discussed by Masson [34], could improve the results but remains to be implemented. Finally, when comparing with vortex methods it is inherent that the Kutta condition at the trailing edge is insured which the actuator line method, with the present technique, do not insure.

11.5 A Lifting Line Model for a Finite Wing with an Elliptic loading

Inspired by the uncertainty about the accuracy of applying forces along actuator lines, lead to test how the concept performed for finite wing with an elliptic loading. The test case satisfy the criteria of having true 3D analytical flow solution, see Katz [30] or Schlichting [51] which prescribe a constant downwash across the entire wing span. Figure 11.14 displays obtained distributions where the applied nominal loading should result in a constant downwash of $-0.1V_o$. The constant downwash prescribed by the solution should be evaluated at the 3/4 chord line

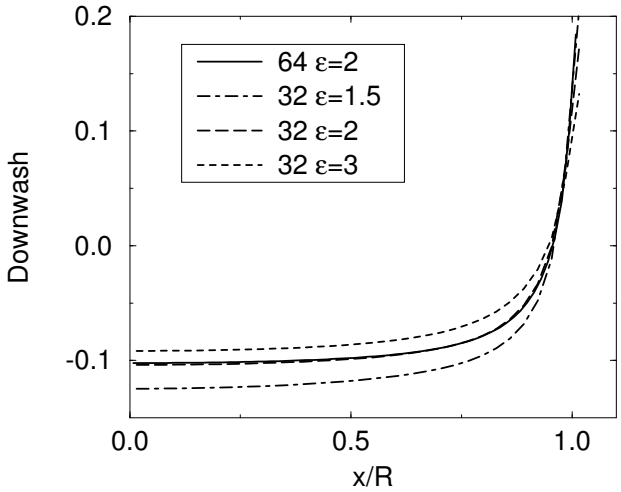

Figure 11.14: Downwash measured on a lifting (actuator) line, using 18 blocks with 32^3 and 64^3 cells, respectively. The line is resolved equidistantly within one block

whereas the loading is applied at the 1/4 chord line. Using panel methods the two positions are obvious, however, using the concept of a regularization parameter ϵ is a different mater. As can be seen from the figure the inner part agrees reasonable well but towards the tip the solution fails as compared with panel methods. Presently, a unique relation between the ϵ parameter and a wing with an elliptic loading cannot be derived. As accurate predictions in the tip region is of key interest for the analysis of tip-correction, it would be desirable if the actuator line method could reproduce the analytical solution better near the tip.

Conclusions and Future Work

The axisymmetric actuator disc and 3D actuator line technique combined with the incompressible Navier-Stokes equations have been applied to aerodynamic flows through wind turbine rotors at various conditions. Numerical result have been presented for the the coned rotor, rotors subjected to yawed inflow and rotors inserted into a tunnel.

Simulations of the coned rotor with constant normal loading reveal that the calculated interference factors a_n and a_z change considerable along the radius of the disc. A modified BEM method can not reproduce this and there seems no easy way to model it, without violating the radial independence of the annular streamtubes. Numerical simulations for a constant normal loaded rotor agrees with theoretical predictions for the calculated C_P and the invariant behaviour of such a rotor, as the flowfield is independent of cone angle and in general the shape of any rotor. The behaviour of flows through coned rotors is fully captured with the actuator disc method.

Yawed simulations using the actuator disc method, in combination with sub models, predicts structural loads with good accuracy, although computations on the Tjæreborg turbine at $\phi_y = +54^o$ over predicts as compared with experiments. At high yaw angles the actuator line method capture observed 3D effects from the root vortex structure, which axisymmetric methods is incapable of.

Computations on rotors inserted in into a tunnel, is modelled effectively using both methods. Furthermore, a new solution based one dimensional axial momentum theory compared excellent with numerical actuator disc computations.

The miscellaneous investigations reveal that the methods can be used to investigate fundamental issues like inherent assumptions connected to BEM methods. The heavily loaded actuator disc by Wu approached with a new method, is fast to run on computer and were found to agree reasonable with Navier-Stokes computations. The tip-corrections theories by Prandtl and Goldstein were investigated with the AL technique and an inverse method. The method is believed to be correct but the results remains inconclusive do to dependencies on grid and force-smearing resolution which affects the accuracy.

Future Work

Some of the ideas that emerged during the writing of this thesis, were impossible to pursue within this project. Some of the ideas are presented here as suggestions to further develop the

actuator disc and actuator line methods.

Although the actuator disc is solved efficiently, the method is not applicable as a design tool. It does, however, include the true axisymmetric physics of the flow which could be used to form the basis of a low-dimensional modelling by applying appropriate transformations. An accurate representations of the flow using normal modes would increase the calculation speed to a level where it could be used as a design tool.

Presently, the actuator line is formulated in polar frame of reference, but new development of the concept should be towards a Cartesian frame of reference. A Cartesian frame of reference naturally facilitates computations on real turbines fixed on the ground whereby effects from atmospheric boundary layer, several turbines (parks) and terrain could be included in a true manner with less model assumptions and projections. It furthermore facilitates computations on rotors inserted into rectangular wind tunnels in connections with experimental investigations. The structural model is somewhat simplified and further improvements could be to combine the AL technique with a well documented aero-elastic model which includes the structural behaviour of all the relevant parts like gearbox, generator, tower, foundation, etc. Fundamental issues related to the tip-correction is not fully understood with the present investigation which calls for new ideas to improve accuracy.

Appendix A

Derivation of the Governing Equations for the Actuator Disc

The basic equations of fluid mechanics are the Navier-Stokes equations and the continuity equation. For an incompressible fluid with constant viscosity they may by reduced to

$$\frac{\partial \boldsymbol{V}}{\partial t} + \boldsymbol{V} \cdot \boldsymbol{\nabla} \boldsymbol{V} = \boldsymbol{f}' - \boldsymbol{\nabla} \left(\frac{p}{\rho} \right) + \nu \nabla^2 \boldsymbol{V}, \tag{A.1}$$

$$\boldsymbol{\nabla} \cdot \boldsymbol{V} = 0, \tag{A.2}$$

where $\boldsymbol{f}'$ represent body forces. Here the Navier-Stokes equations are rewritten as vorticity transport equations on rotational form whereby the pressure is eliminated. Furthermore, the velocity field is represented by a stream function which insures that continuity is satisfied identically. For axisymmetric flow, using polar coordinates the calculation domain is restricted to an axial and radial r, z-plane and it is sufficient with the transport equations for the azimuthal vorticity and velocity components, together with a Poisson equation for the azimuthal stream function.

A.1 The Vorticity Transport Equation in Rotational Form

The Navier-Stokes equations and continuity equation are put into non-dimensional form with the free stream velocity V_o and the radius of the rotor R

$$\frac{\partial \boldsymbol{V}}{\partial t} + \boldsymbol{V} \cdot \boldsymbol{\nabla} \boldsymbol{V} = \boldsymbol{f}' - \boldsymbol{\nabla} (p) + \frac{1}{\mathrm{Re}} \nabla^2 \boldsymbol{V}, \tag{A.3}$$

$$\boldsymbol{\nabla} \cdot \boldsymbol{V} = 0, \tag{A.4}$$

where the Reynolds number is given by Re=$\frac{V_o R}{\nu}$ and p non-dimensional pressure. With the vector identities

$$\boldsymbol{V} \cdot \boldsymbol{\nabla} \boldsymbol{V} = \boldsymbol{\nabla} \left(\frac{V^2}{2} \right) - \boldsymbol{V} \times (\boldsymbol{\nabla} \times \boldsymbol{V}), \tag{A.5}$$

$$\nabla^2 \boldsymbol{V} = \boldsymbol{\nabla} (\boldsymbol{\nabla} \cdot \boldsymbol{V}) - \boldsymbol{\nabla} \times \boldsymbol{\nabla} \times \boldsymbol{V}, \tag{A.6}$$

the Navier-Stokes equations is, with the use of the continuity equation Eq.(A.4) rewritten to

$$\frac{\partial \boldsymbol{V}}{\partial t} - \boldsymbol{V} \times (\boldsymbol{\nabla} \times \boldsymbol{V}) = \boldsymbol{f}' - \boldsymbol{\nabla} H - \frac{1}{\mathrm{Re}} \boldsymbol{\nabla} \times (\boldsymbol{\nabla} \times \boldsymbol{V}), \tag{A.7}$$

where $H = p + \frac{1}{2}V^2$. With the usual definition of the vorticity, $\boldsymbol{\omega} = \boldsymbol{\nabla} \times \boldsymbol{V}$, the curl operator is applied to the Navier-Stokes equations to give the vorticity transport equations

$$\frac{\partial \boldsymbol{\omega}}{\partial t} - \boldsymbol{\nabla} \times (\boldsymbol{V} \times \boldsymbol{\omega}) \;\; = \;\; \boldsymbol{\nabla} \times \boldsymbol{f}' - \frac{1}{\mathrm{Re}} \boldsymbol{\nabla} \times (\boldsymbol{\nabla} \times \boldsymbol{\omega}). \tag{A.8}$$

In the operation the gradient of the pressure head $\boldsymbol{\nabla} H$ vanish since the curl of a gradient of a scalar is identically zero, thus, pressure do not appear in the governing equations of motion in this formulation. It is, however, nessesary to introduce constraints due to the information that has been lost in the curl operation. That is, for multiple connected domains one has to satisfy the original set of Navier-Stokes equations along closed circuits enclosing each body in the domain (See Sørensen and Nygreen [59]). According to Daube et al. [13], the following theorem holds

$$\boldsymbol{\xi} = \frac{\partial \boldsymbol{V}}{\partial t} - \boldsymbol{V} \times (\boldsymbol{\nabla} \times \boldsymbol{V}) - \boldsymbol{f}' + \frac{1}{\mathrm{Re}} \boldsymbol{\nabla} \times (\boldsymbol{\nabla} \times \boldsymbol{V}), \tag{A.9}$$

$$\left(\boldsymbol{\nabla} \times \boldsymbol{\xi} = 0 \,, \quad \int_{\Gamma_i} \boldsymbol{\xi} \cdot d\boldsymbol{l} = 0, \;\; i = 1, ..., p \right) \;\; \Leftrightarrow \;\; (\exists \phi \;:\; \boldsymbol{\xi} = \boldsymbol{\nabla} \phi) \,, \tag{A.10}$$

where Γ_i is the i'te boundary of p closed circuits and $\boldsymbol{l}$ is the tangential vector. Thus, the constraint reads

$$\int_{\Gamma_i} \left(\frac{\partial \boldsymbol{V}}{\partial t} - \boldsymbol{V} \times (\boldsymbol{\nabla} \times \boldsymbol{V}) - \boldsymbol{f}' + \frac{1}{\mathrm{Re}} \boldsymbol{\nabla} \times (\boldsymbol{\nabla} \times \boldsymbol{V}) \right) \cdot d\boldsymbol{l} = 0, \;\; i = 1, ..., p, \tag{A.11}$$

which ensures that the influence from pressure in the original set of Navier-Stokes equations (A.7) is satisfied.

A.2 The Conservative Vorticity Transport Equation

The vorticity vector was introduced as

$$\boldsymbol{\omega} = \boldsymbol{\nabla} \times \boldsymbol{V} = \frac{1}{r} \begin{vmatrix} \boldsymbol{e_r} & r\boldsymbol{e_\theta} & \boldsymbol{e_z} \\ \frac{\partial}{\partial r} & \frac{\partial}{\partial \theta} & \frac{\partial}{\partial z} \\ V_r & rV_\theta & V_z \end{vmatrix}, \tag{A.12}$$

and setting $\omega = \omega_\theta$ the inner part of the convective term from Eq.(A.8) yields

$$\boldsymbol{V} \times \boldsymbol{\omega} = \begin{vmatrix} \boldsymbol{e_r} & \boldsymbol{e_\theta} & \boldsymbol{e_z} \\ V_r & V_\theta & V_z \\ -\frac{\partial V_\theta}{\partial z} & \omega & \frac{1}{r}\frac{\partial}{\partial r}(rV_\theta) \end{vmatrix}. \tag{A.13}$$

Hence, the azimuthal component of the convective term is given by

$$-\boldsymbol{e_\theta} \cdot \boldsymbol{\nabla} \times (\boldsymbol{V} \times \boldsymbol{\omega}) = \frac{\partial}{\partial r} \left(V_r \omega + V_\theta \frac{\partial V_\theta}{\partial z} \right) - \frac{\partial}{\partial z} \left(-V_z \omega + \frac{V_\theta}{r} \frac{\partial}{\partial r}(rV_\theta) \right), \tag{A.14}$$

and put on conservative form

$$\frac{\partial}{\partial r} \left(V_r \omega + \frac{1}{2} \frac{\partial V_\theta^2}{\partial z} \right) + \frac{\partial}{\partial z} \left(V_z \omega - \frac{V_\theta^2}{r} - \frac{1}{2} \frac{\partial V_\theta^2}{\partial r} \right) = \frac{\partial}{\partial r}(V_r \omega) + \frac{\partial}{\partial z}(V_z \omega) - \frac{\partial}{\partial z} \left(\frac{V_\theta^2}{r} \right) \tag{A.15}$$

The curl operator applied to the vorticity vector yields

$$\boldsymbol{\nabla}\times\boldsymbol{\omega}=\frac{1}{r}\begin{vmatrix} \boldsymbol{e_r} & r\boldsymbol{e_\theta} & \boldsymbol{e_z} \\ \frac{\partial}{\partial r} & \frac{\partial}{\partial\theta} & \frac{\partial}{\partial z} \\ -\frac{\partial V_\theta}{\partial z} & r\omega & \frac{1}{r}\frac{\partial}{\partial r}(rV_\theta) \end{vmatrix}, \tag{A.16}$$

thus, the azimuthal component of the diffusive terms gives, with the use of Eq.(A.6)

$$\boldsymbol{e_\theta}\cdot\boldsymbol{\nabla}\times(\boldsymbol{\nabla}\times\boldsymbol{\omega})=-\nabla^2\omega=-\frac{\partial}{\partial r}\left(\frac{1}{r}\frac{\partial r\omega}{\partial r}\right)-\frac{\partial^2\omega}{\partial z^2}. \tag{A.17}$$

As the curl operator is applied to the body forces the azimuthal components may be represented by any orthogonal set of vectors in the r,z-plane. Hence, a set of orthogonal vectors in the span wise and normal directions to the rotor (s,n) is chosen, yielding

$$\boldsymbol{e}_\theta\cdot\boldsymbol{\nabla}\times\boldsymbol{f'}=\frac{\partial f'_r}{\partial z}-\frac{\partial f'_z}{\partial r}=\frac{\partial f'_s}{\partial n}-\frac{\partial f'_n}{\partial s}=-\frac{\partial f'_n}{\partial s}, \tag{A.18}$$

since $f'_s=0$ for any rotor. Inserting the convective terms (A.15), the diffusive terms (A.17) and the body forces Eq.(A.18) into azimuthal component of vorticity transport equations Eq.(A.8) gives the azimuthal vorticity transport equation on conservative form

$$\frac{\partial\omega}{\partial t}+\frac{\partial}{\partial r}(V_r\omega)+\frac{\partial}{\partial z}(V_z\omega)-\frac{\partial}{\partial z}\left(\frac{V_\theta^2}{r}\right)=-\frac{\partial f'_n}{\partial s}+\frac{1}{\mathrm{Re}}\left[\frac{\partial}{\partial r}\left(\frac{1}{r}\frac{\partial r\omega}{\partial r}\right)+\frac{\partial^2\omega}{\partial z^2}\right]. \tag{A.19}$$

A.3 The Conservative Azimuthal Velocity Transport Equation

The azimuthal component of the non-dimensional axisymmetric Navier-Stokes equations reads

$$\frac{\partial V_\theta}{\partial t}+V_r\frac{\partial V_\theta}{\partial r}+V_z\frac{\partial V_\theta}{\partial z}+\frac{V_rV_\theta}{r}=f'_\theta+\frac{1}{\mathrm{Re}}\left[\frac{\partial}{\partial r}\left(\frac{1}{r}\frac{\partial rV_\theta}{\partial r}\right)+\frac{\partial^2V_\theta}{\partial z^2}\right], \tag{A.20}$$

and the axisymmetric continuity equation is restated as

$$\boldsymbol{\nabla}\cdot\boldsymbol{V}=\frac{1}{r}\frac{\partial}{\partial r}(rV_r)+\frac{\partial V_z}{\partial z}=0. \tag{A.21}$$

The continuity equation (A.21) is expanded, multiplied with V_θ and added to the azimuthal component of the convective terms of Eq.(A.7), which is put on conservative form

$$\begin{aligned} -\boldsymbol{e}_\theta\cdot\boldsymbol{V}\times(\boldsymbol{\nabla}\times\boldsymbol{V}) &= V_r\frac{\partial V_\theta}{\partial r}+V_z\frac{\partial V_\theta}{\partial z}+\frac{V_rV_\theta}{r}+V_\theta\left(\frac{V_r}{r}+\frac{\partial V_r}{\partial r}+\frac{\partial V_z}{\partial z}\right), &\text{(A.22)}\\ &= \frac{\partial}{\partial r}(V_rV_\theta)+\frac{\partial}{\partial z}(V_zV_\theta)+\frac{2V_rV_\theta}{r}. &\text{(A.23)}\end{aligned}$$

The rewritten convective terms from Eq.(A.23) are inserted into Eq.(A.20) to give the azimuthal velocity transport equation on conservative form

$$\frac{\partial V_\theta}{\partial t}+\frac{\partial}{\partial r}(V_rV_\theta)+\frac{\partial}{\partial z}(V_zV_\theta)+\frac{2V_rV_\theta}{r}=f'_\theta+\frac{1}{\mathrm{Re}}\left[\frac{\partial}{\partial r}\left(\frac{1}{r}\frac{\partial rV_\theta}{\partial r}\right)+\frac{\partial^2V_\theta}{\partial z^2}\right]. \tag{A.24}$$

A.4 The Poisson Equation

The definition of the stream function vector $\boldsymbol{\Psi}$ in polar cylindrical coordinates is given by

$$\boldsymbol{V} = \boldsymbol{\nabla} \times \boldsymbol{\Psi} = \frac{1}{r} \begin{vmatrix} \boldsymbol{e_r} & r\boldsymbol{e_\theta} & \boldsymbol{e_z} \\ \frac{\partial}{\partial r} & \frac{\partial}{\partial \theta} & \frac{\partial}{\partial z} \\ \Psi_r & r\Psi_\theta & \Psi_z \end{vmatrix} . \tag{A.25}$$

Here the covariant stream function $\boldsymbol{\Psi} = \Psi_j \boldsymbol{e}^j$ is chosen where

$$\Psi_r = \Psi_1 \, , \quad r\Psi_\theta = \Psi_2 \, , \quad \Psi_z = \Psi_3 \, , \tag{A.26}$$

thus, the velocity field is given by

$$\boldsymbol{V} = \frac{1}{r} \begin{vmatrix} \boldsymbol{e_r} & r\boldsymbol{e_\theta} & \boldsymbol{e_z} \\ \frac{\partial}{\partial r} & \frac{\partial}{\partial \theta} & \frac{\partial}{\partial z} \\ \Psi_1 & \Psi_2 & \Psi_3 \end{vmatrix} . \tag{A.27}$$

For axial symmetry the r, z velocity components are, with $\Psi = \Psi_2$, given by

$$V_r = -\frac{1}{r}\frac{\partial \Psi}{\partial z} \, , \quad V_z = \frac{1}{r}\frac{\partial \Psi}{\partial r}, \tag{A.28}$$

Hence, the vorticity from Eq.(A.12) is restated

$$\boldsymbol{\omega} = \boldsymbol{\nabla} \times \boldsymbol{V} = \frac{1}{r} \begin{vmatrix} \boldsymbol{e_r} & r\boldsymbol{e_\theta} & \boldsymbol{e_z} \\ \frac{\partial}{\partial r} & \frac{\partial}{\partial \theta} & \frac{\partial}{\partial z} \\ -\frac{1}{r}\frac{\partial \Psi}{\partial z} & rV_\theta & \frac{1}{r}\frac{\partial \Psi}{\partial r} \end{vmatrix} , \tag{A.29}$$

where the azimuthal component, with $\omega = \omega_\theta$, yields

$$r\omega = -r\frac{\partial}{\partial r}\left(\frac{1}{r}\frac{\partial \Psi}{\partial r}\right) - r\frac{\partial}{\partial z}\left(\frac{1}{r}\frac{\partial \Psi}{\partial z}\right), \tag{A.30}$$

and

$$\omega_r = -\frac{\partial V_\theta}{\partial z} \, , \quad \omega_z = \frac{1}{r}\frac{\partial}{\partial r}(rV_\theta). \tag{A.31}$$

Combining Eq.(A.25) and Eq.(A.29) gives that $\boldsymbol{\omega} = \boldsymbol{\nabla} \times (\boldsymbol{\nabla} \times \boldsymbol{\Psi}) = -\nabla^2 \boldsymbol{\Psi} + \boldsymbol{\nabla}(\boldsymbol{\nabla} \cdot \boldsymbol{\Psi})$ where the azimuthal component reduces to

$$\omega = -\nabla^2 \Psi, \tag{A.32}$$

since $\boldsymbol{e}_\theta \cdot \boldsymbol{\nabla}(\boldsymbol{\nabla} \cdot \boldsymbol{\Psi}) = 0$. Thus, Eq. (A.30) is rewritten to

$$\frac{\partial^2 \Psi}{\partial r^2} - \frac{1}{r}\frac{\partial \Psi}{\partial r} + \frac{\partial^2 \Psi}{\partial z^2} = -r\omega. \tag{A.33}$$

and referred to as the Poisson equation.

A.5 The Pressure Equation

By applying the divergence operator to the Navier-Stokes equations, a pressure equations may be obtained. Equation (A.7) is first reduces to

$$-\boldsymbol{\nabla}\cdot(\boldsymbol{V}\times\boldsymbol{\omega}) = \boldsymbol{\nabla}\cdot\boldsymbol{f}' - \nabla^2 H \tag{A.34}$$

since $\frac{\partial}{\partial t}(\boldsymbol{\nabla}\cdot\boldsymbol{V}) = 0$ and with the use of the vector identity Eq.(A.6) the relation $\boldsymbol{\nabla}\cdot\boldsymbol{\nabla}\times\boldsymbol{\omega} \equiv 0$ removes the diffusion. Assuming axisymmetric conditions, the Laplace operator expands to

$$\nabla^2 H = \frac{\partial^2 H}{\partial r^2} + \frac{1}{r}\frac{\partial H}{\partial r} + \frac{\partial^2 H}{\partial z^2} = \omega^H, \tag{A.35}$$

which differs form the Ψ-equation with a positive sign on the first order term. The divergence of the force vector is conveniently resolved in the local stn coordinate system, thus, the convective part and forces expands to

$$\begin{aligned}
\omega^H &= \frac{1}{r}\frac{\partial}{\partial r}\left[V_\theta\frac{\partial rV_\theta}{\partial r} - rV_z\omega\right] + \frac{\partial}{\partial z}\left[V_r\omega + V_\theta\frac{\partial V_\theta}{\partial z}\right] + \frac{1}{r}\frac{\partial r f_r'}{\partial r} + \frac{\partial f_z'}{\partial z}, \\
&= \frac{3}{2r}\frac{\partial V_\theta^2}{\partial r} + \frac{1}{2}\left(\frac{\partial^2 V_\theta^2}{\partial r^2} + \frac{\partial^2 V_\theta^2}{\partial z^2}\right) - \frac{1}{r}\frac{\partial}{\partial r}(rV_z\omega) + \frac{\partial}{\partial z}(V_r\omega) + \frac{\partial f_n'}{\partial n},
\end{aligned} \tag{A.36}$$

where the boundary conditions at the far field, ie. $r \to \infty$ and $z \to -\infty$ are that $H = 0$, and at the center axis

$$\left.\frac{\partial H}{\partial r}\right|_{r=0} = \mu\frac{\partial}{\partial r}\left(\frac{1}{r}\frac{\partial rV_r}{\partial r}\right), \tag{A.37}$$

however, a Neumann conditions gives sufficient accuracy. Finally, in the far wake, $z \to +\infty$, we have that

$$\left.\frac{\partial H}{\partial z}\right|_{z\to+\infty} = 0. \tag{A.38}$$

The pressure field is determined from the velocity field during post processing by solving Eq.(A.35) for the pressure head H, thus, the static pressure field is found from

$$p = \rho(H - \tfrac{1}{2}V^2). \tag{A.39}$$

In the numerical space the individual terms are evaluated using second order central difference schemes with the pressure head H defined at vertices. With respect to the applied force the smoothing function from Eq.(4.23) is used to form the convolution whereby

$$\begin{aligned}
\boldsymbol{\nabla}\cdot\boldsymbol{f}_\epsilon' &= \frac{\partial f_n' \otimes \eta^{1D}}{\partial n} = \int_{-\infty}^{+\infty}\frac{F_n(s)}{\epsilon\sqrt{\pi}}\frac{\partial\eta^{1D}(p)}{\partial n}dn, \\
&= \int_{-\infty}^{+\infty}\frac{F_n(s)}{\epsilon\sqrt{\pi}}\frac{-2p}{\epsilon^2}\exp\left[-(p/\epsilon)^2\right]dn\,, \quad \frac{\partial p}{\partial n} = 1,
\end{aligned} \tag{A.40}$$

where p in Eq.(A.40) is the normal distance given by Eq.(4.25) and not the static pressure. The function η ensures a smooth, yet confined pressure jump across the actuator disc without spatial oscillations.

A.6 The Heavily Loaded Actuator Disc

The derivation made by Wu of the heavily loaded actuator disc is presented in the following. The deduction made by Wu contains many details not included in his paper, however, a description of mathematical details may be found in the book by Breslin and Andersen [6]. With the use of the vector identity (A.6) the Euler equations are written as

$$\boldsymbol{V}\cdot\boldsymbol{\nabla}\boldsymbol{V}=\boldsymbol{f}'-\boldsymbol{\nabla}\left(\frac{p}{\rho}\right)\quad\Leftrightarrow\quad\boldsymbol{V}\times\boldsymbol{\omega}=\boldsymbol{\nabla}H-\boldsymbol{f}', \tag{A.41}$$

where $H=p/\rho+\frac{1}{2}V^2$. Introducing orthogonal curvilinear coordinates (s,Ψ) in the meridional plane it is assumed that the ratio between distances correspond to velocity ratios in the

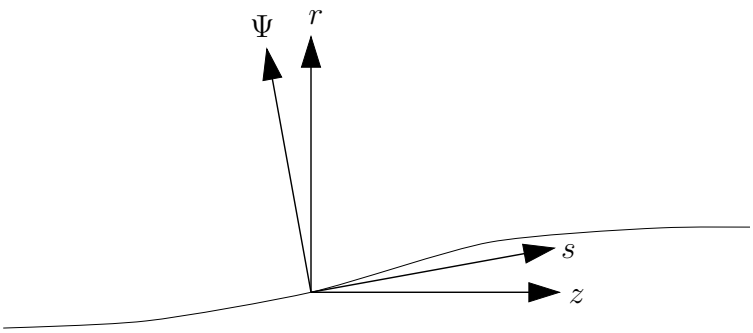

Figure A.1: Orthogonal curvilinear coordinates (s,Ψ) in the meridional plane.

corresponding directions i.e.

$$\frac{dr}{ds}=\frac{V_r}{V_s}\,,\quad\frac{dz}{ds}=\frac{V_z}{V_s}, \tag{A.42}$$

where $V_s^2=V_r^2+V_z^2$. The relation between the system of orthogonal curvilinear coordinates to the reference coordinates (r,z) can be written with the two transformations

$$\frac{\partial}{\partial s}=\frac{1}{V_s}\left(V_r\frac{\partial}{\partial r}+V_z\frac{\partial}{\partial z}\right)=\frac{1}{V_s}\boldsymbol{V}\cdot\boldsymbol{\nabla}, \tag{A.43}$$

$$\frac{\partial}{\partial\Psi}=\frac{1}{rV_s^2}\left(V_z\frac{\partial}{\partial r}-V_r\frac{\partial}{\partial z}\right)=\frac{1}{rV_s^2}\boldsymbol{e_\theta}\cdot\boldsymbol{V}\times\boldsymbol{\nabla}. \tag{A.44}$$

Thus, the θ-component of Eq.(A.41) reduces to

$$-\frac{V_r}{r}\frac{\partial}{\partial r}(rV_\theta)-\frac{V_z}{r}\frac{\partial}{\partial z}(rV_\theta)=-f'_\theta\quad\Leftrightarrow\quad\frac{\partial}{\partial s}(rV_\theta)=\frac{rf'_\theta}{V_s}, \tag{A.45}$$

which shows that the angular momentum varies along a stream tube at a rate proportional to the moment of tangential blade force. Hence, outside the blade row where $f'_\theta=0$, rV_θ is a function of Ψ only. Knowing that $V_\theta=0$ in the free stream, it follows that

$$\begin{aligned} rV_\theta &= f(\Psi) && \text{in the wake}\\ &= 0 && \text{elsewhere,}\end{aligned} \tag{A.46}$$

and if known on the disc, it may be distributed along each stream tube in the wake. Taking the dot product of Eq.(A.41) and $\boldsymbol{V}$, (using that $\boldsymbol{V} \perp \boldsymbol{V} \times \boldsymbol{\omega}$) yields

$$0 = \boldsymbol{V} \cdot \boldsymbol{\nabla} H - \boldsymbol{V} \cdot \boldsymbol{f}' \quad \Leftrightarrow \quad \frac{\partial H}{\partial s} = \frac{\boldsymbol{V} \cdot \boldsymbol{f}'}{V_s}. \tag{A.47}$$

The force $\boldsymbol{f}'$ acting on a perfect fluid are bound to be perpendicular to the local velocity relative to the solid surface. This conditions is obtained through the dot product

$$(\boldsymbol{V} - \boldsymbol{e_\theta} \Omega r) \cdot \boldsymbol{f}' = 0 \quad \Leftrightarrow \quad \boldsymbol{V} \cdot \boldsymbol{f}' = \Omega r f'_\theta, \tag{A.48}$$

hence, using Eq.(A.45) yields

$$\frac{\partial H}{\partial s} = \frac{\Omega r f'_\theta}{V_s} = \Omega \frac{\partial}{\partial s}(r V_\theta), \tag{A.49}$$

and integrating gives that $H = \Omega r V_\theta + H_o,\ H_o = p_o/\rho + \frac{1}{2} V_o^2,\ H_o$ being the free stream pressure head. Furthermore by taking the cross product between $\boldsymbol{V}$ and Eq.(A.41) the θ-component and using of the Ψ-transformation (A.44) yields

$$-\omega r = r^2 \frac{\partial H}{\partial \Psi} - (r V_\theta) \frac{\partial}{\partial \Psi}(r V_\theta) - r \frac{V_z f'_r - V_r f'_z}{V_s^2}. \tag{A.50}$$

Finally inserting H and ω from Eq.(3.4) the Ψ-equation derived by Wu is obtained

$$\frac{\partial^2 \Psi}{\partial r^2} - \frac{1}{r} \frac{\partial \Psi}{\partial r} + \frac{\partial^2 \Psi}{\partial z^2} = (\Omega r^2 - r V_\theta) \frac{\partial}{\partial \Psi}(r V_\theta) - \frac{r f'_\Psi}{V_s}, \tag{A.51}$$

where $f'_\Psi = (V_z f'_r - V_r f'_z)/V_s$ is the Ψ-component of the blade force, a term which Wu neglects as he in general considered it to be small. The boundary conditions are the same as presented in section (3.1).

Appendix B

Sub Models

The effects from tower, dynamic blade deflection, dynamic stall and wind shear is described in the following. The purpose of including these models is to make a more realistic comparisons with experimental data. Here the analysis is limit to these four aspect of wind turbine rotor aerodynamics but other sub models could equally as well have been included.

B.1 Elastic Model - A Modal Method

The elastic behaviour of the blades are modelled with a "standard" modal method (see Craig, Clough and Hansen [10, 11, 25]) where deflection in the flap- and chord wise directions are considered. The continuous vibrating blades (or system) is approximated by a number of normal modes that describes a deflected shape of the entire blade or structure and a time dependent amplitude as

$$v(x,t) = \sum_{i=1}^{N} \psi_i(x)\nu_i(t), \tag{B.1}$$

where $v(x,t)$ is the deflection, $\psi_i(x)$ are the normal modes and $\nu_i(t)$ are the time dependent amplitudes for each mode. The obtained modes ψ_i are used to create a generalized-parameter model of the continuous beam. Using the principle of virtual work and assuming that the deflection may be approximated by the normal modes, a system of equations are obtained as

$$\boldsymbol{M}\ddot{\boldsymbol{\nu}} + \boldsymbol{D}\dot{\boldsymbol{\nu}} + \boldsymbol{K}\boldsymbol{\nu} = \boldsymbol{p}, \tag{B.2}$$

where the mass $\boldsymbol{M}$, damping $\boldsymbol{D}$ and stiffness $\boldsymbol{K}$ matrices are determined as

$$\boldsymbol{M} = m_{ij} = \int_0^R m(s)\psi_i\psi_j ds, \tag{B.3}$$

$$\boldsymbol{D} = d_{ij} = \int_0^R d(s)\psi_i\psi_j ds, \tag{B.4}$$

$$\boldsymbol{K} = k_{ij}(t) = \int_0^R EI(s)\psi_i''\psi_j'' ds + \int_0^R T_s(s,t)\psi_i'\psi_j' ds, \tag{B.5}$$

$$\boldsymbol{p} = p_j(t) = \int_0^R \overline{\boldsymbol{F}}_{stn}(s,t)\psi_i ds. \tag{B.6}$$

The loading is also transformed with the normal modes and it is seen to vary in time. Also the stiffness matrix is time dependent as the force in the span wise direction contributes by gravity and centrifugal loading. The mass and damping matrices are seen to be diagonal, since the modes are orthogonal. The time integration of the system of equations is done by means of an explicit Runge-Kutta-Nystrøm method (see Appendix (B.5)).

B.1.1 Structural Blade Damping

The structural damping characteristics of the blade are best determined from measurements of the logarithmic decrement, δ_j, which then can be used to get a correct damped vibration of the blade. A simple way to apply viscous damping is by multiplying the generalized mass and stiffness matrices by a fraction proportional to the logarithmic decrement. Here the generalized mass matrix is used as suggested by Øye [74], resulting in a matrix equal to

$$d_{ii} = m_{ii}\frac{\omega_i}{\pi}\delta_i, \tag{B.7}$$

where δ_i corresponds to the i'te eigenfrequency ω_i and mode ψ_i. For the Tjæreborg wind turbine the damping amounts approximately to 5 $\%$ in the flap wise direction and 3% in the chord wise direction (Øye [76]).

B.1.2 Integration of Structural Loads

The structural loads i.e. shear forces, normal force and bending moments, $\boldsymbol{T}, \boldsymbol{M}$ are first estimated as the (s,t,n)-projections of gravitational, centrifugal and aerodynamic contributions.

$$\boldsymbol{T} = \boldsymbol{T}^g + \boldsymbol{T}^c + \boldsymbol{T}^a\ , \quad \boldsymbol{M} = \boldsymbol{M}^g + \boldsymbol{M}^c + \boldsymbol{M}^a, \tag{B.8}$$

Referring to the coordinate system previously introduced a beam element of the blade is depicted in figure B.1. Assuming the mass to vary linearly across a small element of the blade between points j and $j+1$ (see Hansen [25]), the gravitational force component is found to

$$T^g_j = T^g_{j+1} - \tfrac{1}{2}(m_j + m_{j+1})\Delta s\overline{g}, \tag{B.9}$$

hence, T^g is determined from the tip to the hub with $T^g_N = 0$ at the tip. The gravitational force component is affected by tilt, coning/deflection and azimuthal angle variations i.e. $\boldsymbol{T}_{stn} = \boldsymbol{B}(\beta_f)\boldsymbol{\Theta}^{\boldsymbol{T}}\boldsymbol{\Phi_t}\boldsymbol{T}_{xyz}$, $\boldsymbol{T}_{xyz} = \{0, T^g, 0\}$. Correspondingly the flap- and edgewise moments M_t, M_n, respectively, are found as

$$\boldsymbol{M}^g_j \ = \ \boldsymbol{M}^g_{j+1} + \boldsymbol{e}_s \times \left[\boldsymbol{T}^g_{j+1}\Delta s + \tfrac{1}{6}(2m_{j+1} + m_i)\overline{g}\Delta s^2 \cdot \boldsymbol{B}(\beta_f)\boldsymbol{\Theta}^{\boldsymbol{T}}\boldsymbol{\Phi_t}\boldsymbol{e}_y\right]. \tag{B.10}$$

The centrifugal loading contributes to the flapwise bending moment through coning and the flapwise deflection. Thus we have that the centrifugal loading p^c from a differential element dr is

$$dp^c = r\Omega^2 m dr\ , \quad r \simeq s\cos\beta + v_n\sin\beta. \tag{B.11}$$

Again the deflection and mass is assumed to vary linearly across each element as

$$s = s_{j+1} - \hat{s}\ , \quad v_n = (v_{nj} - v_{nj+1})\frac{\hat{s}}{\Delta s} + v_{nj+1}, \tag{B.12}$$

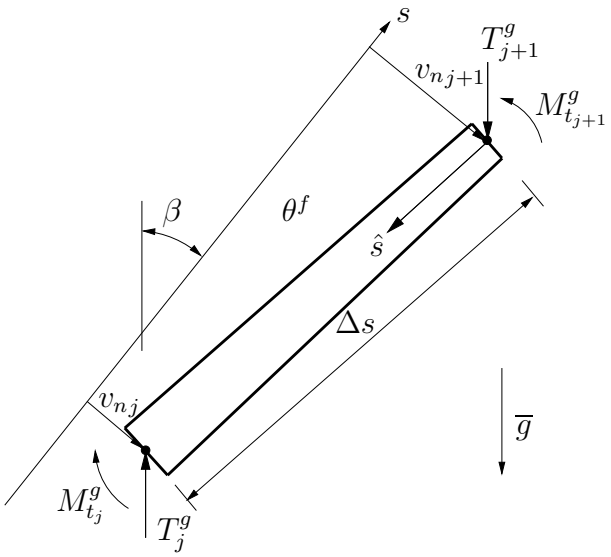

Figure B.1: Element of blade, $\hat{s}$ is a local coordinate in opposite direction to s from $j+1$ to j. Coning/deflection is given by $\beta_f = \beta - \theta^f$ where v_n is the flapwise deflection and $\theta^f = v_n' = \sum_{i=1}^{N} \psi_i'(x)\nu_i(t)$. The moments M_{stn} are defined using the right hand rule.

where

$$\frac{dr}{d\hat{s}} = -\cos\beta + (v_{nj} - v_{nj+1})\frac{\sin\beta}{\Delta s}. \tag{B.13}$$

Inserting in Eq.(B.11) gives that for a small element Δs the centrifugal force T^c is

$$\begin{aligned} T^c_j = T^c_{j+1} &- \Omega^2 \int_0^{\Delta s} \left[(s_{j+1} - \hat{s})\cos\beta + \left\{ \frac{\hat{s}}{\Delta s}(v_{nj} - v_{nj+1}) + v_{nj+1} \right\} \sin\beta \right] \\ &\cdot \left[\frac{\hat{s}}{\Delta s}(m_j - m_{j+1}) + m_{j+1} \right] \left[-\cos\beta + \frac{(v_{nj} - v_{nj+1})}{\Delta s}\sin\beta \right] d\hat{s}, \\ = T^c_{j+1} &+ T^{cm}_j. \end{aligned} \tag{B.14}$$

The normal and shear force projections T^c_s and T^c_n reads

$$T^c_{s_j} = T^c_j \cos\beta_f \ , \quad T^c_{n_j} = T^c_j \sin\beta_f, \tag{B.15}$$

and the corresponding moments

$$M^c_{t_j} = M^c_{t_{j+1}} - T^c_{n_{j+1}}\Delta s + \int_0^{\Delta s} T^{cm}_j d\hat{s} \sin\beta_f. \tag{B.16}$$

The aerodynamic loading p, projected onto the normal and tangential directions (T^a_n, T^a_t), respectively, also varies linearly between the points $j+1$ and j, hence

$$T^a_{n_j} = T^a_{n_{j+1}} + \tfrac{1}{2}(F_{n_j} + F_{n_{j+1}})\Delta s, \tag{B.17}$$

$$T^a_{t_j} = T^a_{t_{j+1}} + \tfrac{1}{2}(F_{t_j} + F_{t_{j+1}})\Delta s. \tag{B.18}$$

Likewise, integration of the aerodynamic forces gives corresponding contributions to the moments as

$$M^a_{t_j} = M^a_{t_{j+1}} - T^a_{n_{j+1}}\Delta s - \tfrac{1}{6}(F_{n_j} + 2F_{n_{j+1}})\Delta s^2, \tag{B.19}$$

$$M^a_{n_j} = M^a_{n_{j+1}} + T^a_{t_{j+1}}\Delta s + \tfrac{1}{6}(F_{t_j} + 2F_{t_{j+1}})\Delta s^2. \tag{B.20}$$

The total flapwise bending moment is found as the sum of gravitational, centrifugal and aerodynamic contributions. The loading that is applied in Eq.B.6 is found as the gradient of the forces given by

$$\overline{F}_{t_j} = \frac{T_{t_{j+1}} - T_{t_{j-1}}}{2\Delta s}\,, \quad \overline{F}_{n_j} = \frac{T_{n_{j+1}} - T_{n_{j-1}}}{2\Delta s}. \tag{B.21}$$

Next, the dynamic loads from the damped vibrating blade is determined from the acceleration and velocity of the blade found as

$$\ddot{\boldsymbol{v}}(s,t) = \sum_{i=1}^{n} \boldsymbol{\psi}_i(s)\ddot{\boldsymbol{\nu}}_i(t)\,, \quad \dot{\boldsymbol{v}}(s,t) = \sum_{i=1}^{n} \boldsymbol{\psi}_i(s)\dot{\boldsymbol{\nu}}_i(t). \tag{B.22}$$

The contribution from acceleration reads

$$\boldsymbol{T}^{acc}_j = \boldsymbol{T}^{acc}_{j+1} + \tfrac{1}{2}(\ddot{\boldsymbol{v}}_j m_j + \ddot{\boldsymbol{v}}_{j+1} m_{j+1})\Delta s_j, \tag{B.23}$$

$$\boldsymbol{M}^{acc}_j = \boldsymbol{M}^{acc}_{j+1} + \boldsymbol{e}_s \times \left[\boldsymbol{T}^{acc}_{j+1}\Delta s_j + \tfrac{1}{6}(\ddot{\boldsymbol{v}}_j m_j + 2\ddot{\boldsymbol{v}}_{j+1} m_{j+1})\Delta s_j^2\right], \tag{B.24}$$

and correspondingly from damping

$$\boldsymbol{T}^{d}_j = \boldsymbol{T}^{d}_{j+1} + \tfrac{1}{2}(\boldsymbol{d}_j + \boldsymbol{d}_{j+1})\Delta s_j, \tag{B.25}$$

$$\boldsymbol{M}^{d}_j = \boldsymbol{M}^{d}_{j+1} + \boldsymbol{e}_s \times \left[\boldsymbol{T}^{d}_{j+1}\Delta s_j + \tfrac{1}{6}(\boldsymbol{d}_j + 2\boldsymbol{d}_{j+1})\Delta s_j^2\right], \tag{B.26}$$

where $\boldsymbol{d}(s,t) = \sum_{i=1}^{N} \frac{\omega_i}{\pi}\delta_i m(s)\psi_i(s)\dot{\boldsymbol{v}}_i(t)$. The shear forces and bending moments are with the dynamic contributions subtracted given as

$$\boldsymbol{T} = \boldsymbol{T}^g + \boldsymbol{T}^c + \boldsymbol{T}^a - \boldsymbol{T}^{acc} - \boldsymbol{T}^d, \tag{B.27}$$

$$\boldsymbol{M} = \boldsymbol{M}^g + \boldsymbol{M}^c + \boldsymbol{M}^a - \boldsymbol{M}^{acc} - \boldsymbol{M}^d. \tag{B.28}$$

Using simple beam theory the sectional structural data for wind turbine blade may be defined with respect to a reference co-ordinate system (s,t,n) and the principal bending axis $(1,2)$, as displayed in figure B.2. The moments (M_t, M_n) are projected onto the cross sectional principal axis of blade, including the spanwise force, T_s

$$M'_t = M_t - T_s \cdot x_E \sin\gamma\,, \quad M'_n = M_n - T_s \cdot x_E \cos\gamma, \tag{B.29}$$

where $\gamma = \gamma_l + \gamma_t$ is the pitch (sum of twist and total pitch). With the principal axis aligned with an angle $\gamma + \xi$ the principal moments (M_1, M_2) are

$$M_1 = -M'_t\cos(\gamma+\xi) \;+\; M'_n\sin(\gamma+\xi), \tag{B.30}$$

$$M_2 = \;\; M'_t\sin(\gamma+\xi) \;+\; M'_n\cos(\gamma+\xi). \tag{B.31}$$

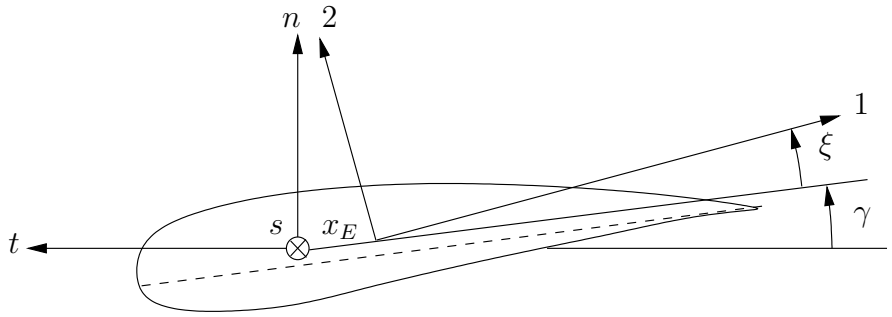

Figure B.2: Principal axis $(1, 2)$ *in relation to reference system* (s, t, n).

Simplifications - The Tjæreborg Structural Data

The structural stiffness data, EI, for the Tjæreborg wind turbine presented in [25], are defined with respect to the principal axis also referred to as structural pitch, however, the calculated eigenmodes as well as the loading were assumed to be aligned with the local reference system (s, t, n) for all the presented results. The inconsistency is proportional to the angle $(\gamma + \xi)$, which in general is small, hence, some inaccuracy may be referred to this simplification.

B.2 Tower

The tower of the wind turbine has an influence on the flow that consist of two contributions, the tower it self and the wake behind the tower as depicted in figure (B.3). A model that consist of a dipole and a source as described by Björck [4] is used together with the axisymmetric actuator disc model. Considering the cross section of the tower to be equivalent with a cylinder the flow

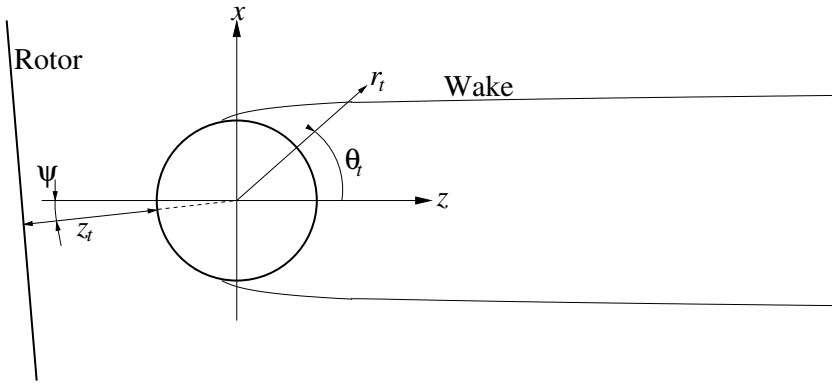

Figure B.3: Tower and wake

may be modelled by potential flow. By superposition of a dipole and a source combined with a free stream a reasonable modelling is achieved. The stream function for the dipole and free stream is

$$\psi \;=\; U_o r_t \left(1 - \frac{R_t^2}{r_t^2}\right) \sin\theta_t, \tag{B.32}$$

where r_t is the radius away from the tower and R_t is the radius of the tower. The radial and tangential velocities are found as

$$(U_r^t,\ U_\theta^t) \ = \ \left(\frac{1}{r}\frac{\partial \psi}{\partial \theta},\ -\frac{\partial \psi}{\partial r}\right) \ = \ U_o\left[\left(1-\frac{R_t^2}{r_t^2}\right)\cos\theta_t,\ -\left(1+\frac{R_t^2}{r_t^2}\right)\sin\theta_t\right]. \quad \text{(B.33)}$$

Projecting gives that

$$(U_x^t,\ U_z^t) \ = \ (U_\theta^t\cos\theta_t + U_r^t\sin\theta_t,\ -U_\theta^t\sin\theta_t + U_r^t\cos\theta_t), \quad \text{(B.34)}$$

and inserting yields

$$(U_x^t,\ U_z^t) \ = \ U_o\left[\frac{2R_t^2xz}{(x^2+z^2)^2},\ 1+\frac{R_t^2(x^2-z^2)}{(x^2+z^2)^2}\right], \quad \text{(B.35)}$$

where $r_t^2 = x^2 + z^2$. From figure B.3 and the transformations given for the 3D kinematics, the blade positions relative to the tower $\boldsymbol{x}_{xyz}^{i_B}$ are given by Eq.(7.2), the blade deflection $\boldsymbol{v}_{stn}^{i_B}$ and (R_t, z_t) as

$$\boldsymbol{x}_{xyz}^{i_B} = \boldsymbol{\Phi_y^T\Phi_t^T\Theta B^T}(\boldsymbol{x}+\boldsymbol{v})_{stn}^{i_B} - \boldsymbol{e}_z(R_t+z_t)\boldsymbol{\Phi_y}. \quad \text{(B.36)}$$

The dipole gives the correct disturbance due to a 2D cylinder in an inviscid flow. The wake however, also influence the flowfield upstream the cylinder. A source is introduced proportional to the wake size and thereby the drag $D = \frac{1}{2}\rho U_o^2 \cdot 2R_t \cdot C_D = q\rho U_o$, thus $q = U_o C_D R_t$ and

$$(U_x^w,\ U_z^w) \ = \ \frac{q}{2\pi r_t}(\sin\theta_t,\ \cos\theta_t) \ = \ \frac{U_o C_D R_t}{2\pi r_t}\left(\frac{x}{r_t},\ \frac{z}{r_t}\right). \quad \text{(B.37)}$$

The combined influence reads

$$(U_x,\ U_z) \ = \ U_o\left[\frac{2R_t^2xz}{(x^2+z^2)^2}+\frac{C_DR_tx}{2\pi(x^2+z^2)},\ 1+\frac{R_t^2(x^2-z^2)}{(x^2+z^2)^2}+\frac{C_DR_tz}{2\pi(x^2+z^2)}\right], \quad \text{(B.38)}$$

and the influence referred to the local coordinate system (s, t, n) reads

$$\boldsymbol{V}_{stn}^{\text{Tower}} = \boldsymbol{B\Theta\Phi_t\Phi_y}\cdot\left\{\begin{array}{c} U_x \\ 0 \\ U_z - U_o \end{array}\right\}. \quad \text{(B.39)}$$

The velocity U_o is set equal to V_z at the disc position where V_z is corrected for wind shear as presented in appendix B.4. Björck [4] states that the source is not an ideal way to represent wake influence, which may be realized by considering the front surface point of the tower where the U_z should be zero. However, far enough away from the cylinder it is a reasonable approximation. It should be noted that the influence of the dipole decays as $1/r^2$ whereas the source influence only decays as $1/r$.

B.3 Dynamic Stall

The dynamic stall model by Øye [78] is presented in the following. The basic idea of the model is to interpolate the lift coefficient C_L between a $C_{L2\pi} = 2\pi(\alpha - \alpha_o)$ dependency and a fully separated C_{Lsep} dependency, with a dynamic time delay τ. The method may be summarized in the following steps :

- Define $C_{L2\pi}(\alpha) = 2\pi(\alpha - \alpha_o)$
- Define fully separated $C_{Lsep}(\alpha)$
- Define f_{st} from static lift curve : $C_{Lst}(\alpha) = f_{st}(\alpha)C_{L2\pi}(\alpha) + [1 - f_{st}(\alpha)]\, C_{Lsep}(\alpha)$
- Find $\frac{df}{dt} = \frac{1}{\tau}(f_{st} - f)$, Euler method is sufficient i.e. $f_i = f_{i-1} + [f_{st}(\alpha) - f_{i-1}]\, \frac{\Delta t}{\tau}$
- Finally, dynamic lift coefficient is found as : $C_L(\alpha) = f_i C_{L2\pi}(\alpha) + [1 - f_i]\, C_{Lsep}(\alpha)$

The fully separated C_{Lsep} dependency is defined somewhat arbitrarily, although with a starting slope of the order one half of the unseparated curve and with a maximum value fitting the assumed static $C_{Lst}(\alpha)$ at approximately 30^o degrees angle of attack. The transition between $C_{Lsep}(\alpha)$ and $C_{Lst}(\alpha)$ is usually fitted with a smooth curve. Here a smoothing function is applied which combine a definition of C_{Lsep} and the transition to $C_{Lst}(\alpha)$ summarized in the following steps :

- Define $C_{L2\pi}(\alpha) = 2\pi(\alpha - \alpha_o)$
- $C_{Lsep}(\alpha) = G \cdot C_{Lst}(\alpha)$, where $G = (1 - A_o) + A_o \frac{1}{2}\{1 + \tanh[B_o(|\alpha - \alpha_o| - \alpha_1)]\}$, $A_o \simeq 0.3 - 0.5$, $B_o \simeq 5 - 15$, $\alpha_1 \simeq \alpha(C_{Lst,max})$
- $f_{st}(\alpha) = \frac{C_{Lst}(\alpha) - C_{Lsep}(\alpha)}{C_{L2\pi}(\alpha) - C_{Lsep}(\alpha)}$

The dynamic time delay τ should be chosen to give the best fit to experimental data, but of the order proportional to the reduced time c/V. Øye suggest a value of the order $\tau = \frac{4c}{V_{rel}}$ and he states that the resulting response is relative insensitive to variations in the time constant.

B.4 Wind Shear

In order to include wind shear effects, the exponent law used in [47] is applied

$$V_z(H) = V_z(H_{hub}) \left(\frac{H}{H_{hub}}\right)^{\alpha_s}, \tag{B.40}$$

where H is the height from the ground, H_{hub} the hub height, $V_z(H_{hub})$ the velocity at hub height in the free stream direction and α_s the wind shear coefficient. When using the actuator disc and the actuator line method, the flowfield is given and therefore the local component in the free stream direction is corrected using the local velocity, i.e.

$$V_z(H) = V_z(H) \left(\frac{H}{H_{hub}}\right)^{\alpha_s}. \tag{B.41}$$

Consequently, the aerodynamic forces and influence of the tower is based on the projection of the corrected component in the free stream direction $V_z(H)$.

B.5 Runge-Kutta-Nystrøm Method

The Runge-Kutta-Nystrøm method is used to integrate the dynamic system (see Øye,[74] or Collatz [7])

$$\boldsymbol{M}\ddot{\boldsymbol{x}} + \boldsymbol{D}\dot{\boldsymbol{x}} + \boldsymbol{K}\boldsymbol{x} = \boldsymbol{p}(t, \boldsymbol{x}, \dot{\boldsymbol{x}}), \tag{B.42}$$

in time. The system is solved with respect to $\ddot{\boldsymbol{x}}$ given as

$$\ddot{\boldsymbol{x}} = \boldsymbol{f}(t, \boldsymbol{x}, \dot{\boldsymbol{x}}), \quad \boldsymbol{f} = \boldsymbol{M}^{-1}\left[\boldsymbol{p}(t, \boldsymbol{x}, \dot{\boldsymbol{x}}) - \boldsymbol{K}\boldsymbol{x} - \boldsymbol{D}\dot{\boldsymbol{x}}\right]. \tag{B.43}$$

Since $\boldsymbol{M}$ is diagonal the inverse $\boldsymbol{M}^{-1}$ is easily found. With the initial conditions that

$$t = t^n, \quad \boldsymbol{x} = \boldsymbol{x}^n, \quad \dot{\boldsymbol{x}} = \dot{\boldsymbol{x}}^n, \quad \ddot{\boldsymbol{x}} = \ddot{\boldsymbol{x}}^n, \tag{B.44}$$

and time step Δt we first calculate

$$\begin{aligned}
\boldsymbol{A} &= \tfrac{1}{2}\Delta t\ddot{\boldsymbol{x}}^n, \quad \boldsymbol{a} = \tfrac{1}{2}\Delta t\left(\dot{\boldsymbol{x}}^n + \tfrac{1}{2}\boldsymbol{A}\right), \\
\boldsymbol{B} &= \tfrac{1}{2}\Delta t\boldsymbol{f}\left(t^n + \tfrac{1}{2}\Delta t,\ \boldsymbol{x}^n + \boldsymbol{a},\ \dot{\boldsymbol{x}}^n + \boldsymbol{A}\right), \\
\boldsymbol{C} &= \tfrac{1}{2}\Delta t\boldsymbol{f}\left(t^n + \tfrac{1}{2}\Delta t,\ \boldsymbol{x}^n + \boldsymbol{a},\ \dot{\boldsymbol{x}}^n + \boldsymbol{B}\right), \quad \boldsymbol{c} = \Delta t\left(\dot{\boldsymbol{x}}^n + \boldsymbol{C}\right), \\
\boldsymbol{D} &= \tfrac{1}{2}\Delta t\boldsymbol{f}\left(t^n + \Delta t, \boldsymbol{x}^n + \boldsymbol{c},\ \dot{\boldsymbol{x}}^n + 2\boldsymbol{C}\right).
\end{aligned}$$

Hereafter the real time step is performed yielding

$$t^{n+1} = t^n + \Delta t, \tag{B.45}$$

$$\boldsymbol{x}^{n+1} = \boldsymbol{x}^n + \Delta t\left[\dot{\boldsymbol{x}}^n + \tfrac{1}{3}\left(\boldsymbol{A} + \boldsymbol{B} + \boldsymbol{C}\right)\right], \tag{B.46}$$

$$\dot{\boldsymbol{x}}^{n+1} = \dot{\boldsymbol{x}}^n + \tfrac{1}{3}\left(\boldsymbol{A} + 2\boldsymbol{B} + 2\boldsymbol{C} + \boldsymbol{D}\right), \tag{B.47}$$

$$\ddot{\boldsymbol{x}}^{n+1} = \boldsymbol{f}\left(t^{n+1}, \boldsymbol{x}^{n+1}, \dot{\boldsymbol{x}}^{n+1}\right). \tag{B.48}$$

The right hand side $\boldsymbol{p}(t, \boldsymbol{x}, \dot{\boldsymbol{x}})$ and the stiffness matrix $\boldsymbol{K}$ should be evaluated at the "half step" in the evaluation of $\boldsymbol{B}, \boldsymbol{C}, \boldsymbol{D}$ in order to obtain a true high order time integration. In combination with the numerical actuator disc/line models, this would require new solutions of the flowfield at equivalent time steps. For simplicity, however, $\boldsymbol{p}, \boldsymbol{K}$ are based on the latest flowfield solution.

Appendix C

Thrust and Power Coefficients for the Coned Rotor

The thrust is determined by integration of the resulting axial force across the disc,

$$T = \int_{A_n} f_z dA_n = \int_{A_n} f_n \cos\beta dA_n = 2\pi \cos^2\beta \int_0^R f_n s ds. \tag{C.1}$$

For the constant loaded rotor $\Omega \rightarrow \infty$ and $\Omega V_\theta \rightarrow$ constant. Hence, the kinetic power is integrated as

$$P_{kin} = \int_{A_n} f_n V_n dA_n = 2\pi \cos\beta \int_0^R f_n V_n s ds. \tag{C.2}$$

For the real rotor the rotational power is determined directly from the tangential moment and rotational speed given by

$$P_{rot} = \Omega \int_{A_n} f_\theta (s\cos\beta) dA_n = 2\pi\Omega \cos^2\beta \int_0^R f_\theta s^2 ds. \tag{C.3}$$

The corresponding dimensionless coefficients are obtained by normalization with the projected area in the axial direction. Thus, the thrust coefficient is defined as

$$C_T = \frac{T}{\frac{1}{2}\rho V_o^2 \pi R^2 \cos^2\beta}, \tag{C.4}$$

and the power coefficients as

$$C_{P_{kin}} = \frac{P_{kin}}{\frac{1}{2}\rho V_o^3 \pi R^2 \cos^2\beta}, \quad C_{P_{rot}} = \frac{P_{rot}}{\frac{1}{2}\rho V_o^3 \pi R^2 \cos^2\beta}. \tag{C.5}$$

Bibliography

[1] Bareiss R, Guidati G, Wagner S. Wake simulations for wind turbines with a free, prescribed and hybrid wake method. Proc. 10th IEA Symp. on the *Aerodynamics of Wind Turbines*, Edinburgh, 1996; 23–28.

[2] Berkman ME, Sankar LN, Berezin CR, Torok MS. A Navier-Stokes/full potential/free wake method for rotor flows. *AIAA Paper 97-0401*, 1997.

[3] Betz A. Das maximum der theoretisch möglichen ausnützung des windes durch windmotoren. *Zeitschrift für das gesamte Turbinewessen*, 1920; 307–309.

[4] Björck A. Aerodynamic engineering calculations of blade tower interaction. Proc. of Int. Energy Agency, IEA 13th Symposium on *Aerodynamics of Wind Turbines*, Stockholm, Sweden, 1999; 173–186.

[5] Björck A, Ronsted G, Mongtgomerie B. Aerodynamic section characteristics of a rotating and non-rotating 2.375m wind turbine blade. FFA report, TN-1995-03, The Aeronautical Research Institute of Sweden, Sweden, 1995.

[6] Breslin JP and Andersen P. *Hydrodynamics of ship propellers*. Cambridge Uni. Press, U.K., 1994.

[7] Collatz L. *The numerical treatment of differential equations.* 3rd. ed., Springer Verlag, Berlin, 1966;537.

[8] Conway JT. Analytical solutions for the actuator disc with variable radial distribution of load. *J. Fluid Mech.*, 1995; **297**: 327–355.

[9] Conway JT. Exact actuator disc solutions for non-uniform heavy loading and slipstream contraction. *J. Fluid Mech.*, 1998; **365**: 235–267.

[10] Craig Jr., Roy R. *Dynamics of Structures, an introduction to computer methods*. John Wiley & Sons, 1981.

[11] Clough, RW. & Penzien J. *Structural Dynamics*. McGraw Hill, 1975.

[12] Corten, GP. Flow separation on wind turbine blades. *PhD Dissertation*. Universiteit Utrecht, Nederland, 2001.

[13] Daube O, Guermond JL, Sellier A. Sur la formulation vitesse-tourbillon des équation de Navier Stokes en écoulement incompressible. *C.R.Acad.Sci.Paris t.313* . Série II, Including abridged english version titled: On the velocity vorticity formulation of the Navier Stokes equations in incompressible flow, 1991; 377-382

[14] De Vries O. Fluid dynamic aspects of wind energy conversion. *AGARD-AG-243*. 1979.

[15] Duque EPN, Van Dam CP, Hughes S. Navier-Stokes simulations of the NREL combined experiment phase II rotor. *AIAA Paper 99-0037*, 1999.

[16] Ekaterinaris JA. Numerical simulation of incompressible two-bladed rotor flow field. *AIAA Paper 97-0398*, 1997.

[17] Fejtek I, Roberts L. Navier-Stokes computation of wing/rotor interaction for a tilted rotor in hover. *AIAA Paper 91-0707*, 1991.

[18] Froude RE. On the part played in propulsion by difference in pressure. *Transaction of the Institute of Naval Architects*, 1889; **30**: 390–423.

[19] Glauert H. Airplane propellers. In Durand WF(ed.). *Aerodynamic Theory*. Dover, New York, 1963; **4**(Division L): 169-269

[20] Goorjian PM. An invalid equation in the general momentum theory of the actuator disc. *AIAA J.*, 1975; **10**(4): 543–544.

[21] Goldstein S. On the vortex theory of screw propellers. *Proc. Royal Soc.*, 1929; **123** A: 440–465.

[22] Greenberg MD. Nonlinear actuator disc theory. *Zeitschrift für Flugwissenschaften*, 1972; **20**(3): 90–98.

[23] Hackett JE, Ashill PR, Mokry M. Wall correction methods for powered models of conventional take off and landing Aircraft. *Wind Tunnel Wall Correction, AGRAD-AG-336*, 1998; 7.1-7.27.

[24] Hansen MOL, Sørensen JN, Michelsen JA, Sørensen NN. A global Navier-Stokes rotor prediction model. *AIAA Paper 97-0970*, 1997.

[25] Hansen, MOL. *Aerodynamics of Wind Turbines*. James & James, London, 2000.

[26] Hansen, MOL. *LM19.1m aerofoil characteristics corrected for 3-D effects*. Private communication, 2000.

[27] Hirsch C. *Numerical Computation of Internal and External Flows, Vol 2: Computational Methods for Inviscid and Viscous Flows*. Wiley Series in Numerical Methods in Engineering, John Wiley & Sons, 1990.

[28] Hough GR, Ordway DE. The generalized actuator disc. *Developments in Theoretical and Applied Mechanics*, ed. Shaw WA, Pergamon Press, Oxford, 1965; **2**: 317–336.

[29] Johansen J, Sørensen NN, Michelsen JA, Schreck S. Detached-eddy simulation of flow around the NREL phase VI blade. *Wind Energy*, 2002; **5**: 185–197.

[30] Katz J, Plotkin A. *Low-Speed Aerodynamics: From Wing Theory to Panel Methods* McGraw Hill Series in Aeronautical and Aerospace Engineering, McGraw Hill Inc. 1991.

[31] Lanchester FW. A contribution to the theory of propulsion and the screw propeller. *Transaction of the Institution of Naval Architects*, 1915; **56**: 98–116,135–153.

[32] Madsen HA. A CFD analysis of the actuator disc flow compared with momentum theory results. Proc. 10th IEA Symp. on the *Aerodynamics of Wind Turbines*, Edinburgh, 1996; 109–124.

[33] Madsen HA, Rasmussen F. The influence on energy conversion and induction from large blade deflections. *European Wind Energy Conf.*, Nice, France, 1999; 138–141.

[34] Masson C, Smaïli A, Leclerc C. Aerodynamic analysis of HAWTs operating in unsteady conditions. *Wind Energy*, 2001; **4**: 1–22.

[35] Michelsen JA. Basis3D – a platform for development of multiblock PDE solvers. *Report AFM 92-05*, Dept. of Fluid Mechanics, Technical University of Denmark, DTU, 1992.

[36] Michelsen JA. Block structured multigrid solution of 2D and 3D elliptic PDE's. *Report AFM 94-06*, Dept. of Fluid Mechanics, Technical University of Denmark, DTU, 1994.

[37] Mikkelsen R, Sørensen JN, Shen WZ. Modelling and analysis of the flow field around coned rotors. *Wind Energy*, 2001; **4**: 121–135.

[38] Mikkelsen R, Sørensen JN. Yaw Analysis Using a Numerical Actuator Disc Model. Proc. 14th IEA Symp. on the *Aerodynamics of Wind Turbines*, Boulder, Col, USA, 2000; 53–59

[39] Mikkelsen R, Sørensen JN, Shen WZ. Yaw Analysis Using a 3D Actuator Line Model. *European Wind Energy Conf.*, Copenhagen, Danmark, 2001; 478–480

[40] Mikkelsen R, Sørensen JN. Modelling of Wind Tunnel Blockage. *Global Windpower Conf.*, Paris, France, 2002; on CD-ROM

[41] Miller RH. The aerodynamic and dynamic analysis of horizontal axis wind turbines. *J. Wind Eng. Ind. Aerodyn.*, 1983; **15**: 329–340.

[42] Paulsen US. Konceptundersøgelse Nordtank 500/41 Strukturelle laster (in Danish). *Risø-I-936(DA)*, Risø Nat. Lab., Roskilde, Denmark, 1995.

[43] Prandtl L, Betz A. *Vier abhandlungen zur hydrodynamik und aerodybamik*. Göttingen, 1927: 88–92.

[44] Rankine, WJM. On the mechnical principles of the action of propellers. *Transaction of the Institute of Naval Architects*, 1865; **6**: 13–39.

[45] Rajagopalan RG, Mathur SR. Three dimensional analysis of a rotor in forward flight. *J. American Helicopter Society*, 1993; **38**(3): 14–25.

[46] Ronsted G, Dahlberg J, Meijer S, He DX, Chen M. Pressure measurements on a 5.35m HAWT in CARDC 12m x 16m wind tunnel compared to theoretical pressure distributions. *Proceedings of the European Wind Energy Conference (EWEC 89)*, Glasgow, Scotland, 1989; 729–735.

[47] Schepers JG and Snel H. Dynamic inflow: Yawed conditions and partial span pitch control. *Report ECN-C–95-056*, Netherlands Energy Research Foundation, ECN, 1995.

[48] Schreck S, Hand M, Fingersh L, Robinson M, Simms D. NREL unsteady aerodynamics experiment wind tunnel test: Flow field characterization and model predictions. *European Wind Energy Conf.*, Copenhagen, Danmark, 2001; 35–47

[49] Shen WZ, Mikkelsen R, Sørensen JN, Bak C. Evaluation of the Prandtl Tip Correction for Wind Turbine Computations. *Global Windpower Conf.*, Paris, France, 2002; –

[50] Simoes FJ, Graham JMR. Prediction of loading on a horizontal axis wind turbine using a free vortex wake model. *Proc. of the 13th BWEA Conf.*, Swansea, 1991; 247–253.

[51] Schlichting H, Truckenbrodt E. *Aerodynamik des Flugzeuges, Teil II.* Springer-Verlag, Berlin, 1960.

[52] Schmidt GH, Sparenberg JA. On the edge singularity of an actuator disk with large constant normal load. *J. Ship Research*, 1977; **21**(2): 125–131.

[53] Spera DA. *Wind Turbine Technology*. ASME Press, New York, 1994.

[54] Sørensen JN. Three-level, viscous-inviscid interaction technique for the prediction of separated flow past rotating wing. *PhD Dissertation, AFM 86-03*, Dept. of Fluid Mechanics, Technical University of Denmark, DTU, 1986.

[55] Sørensen JN, Myken A. Unsteady actuator disc model for horizontal axis wind turbine. *J. Wind Eng. Ind. Aerodyn.*, 1992; **39**: 139–149.

[56] Sørensen JN, Kock CW. A model for unsteady rotor aerodynamics. *J. Wind Eng. Ind. Aerodyn.*, 1995; **58**: 259–275.

[57] Sørensen JN, Gervang B, Madsen HA. Vindmølle aerodynamik: Status og perspektiver (in danish). *Report ET-AFM97-01*, Fluid Mechanics, DTU, 1997.

[58] Sørensen JN, Shen WZ, Munduate X. Analysis of wake states by a full-field actuator disc model. *Wind Energy*, 1998; **1**: 73–88.

[59] Sørensen JN, Nygreen PJ. Unsteady vorticity-stream function algorithm for external flows. *Computer & Fluids*, 2001; **30**: 69–87.

[60] Sørensen JN, Mikkelsen R. On the Validity of the Blade Element Momentum Method. *European Wind Energy Conf.*, Copenhagen, Danmark, 2001; 362–366

[61] Sørensen JN, Shen WZ. Numerical modeling of wind turbine wakes. *J. Fluids Engineering, ASME Trans.*, June 2002; **124**: 393–399.

[62] Sørensen NN. General purpose flow solver applied to flow over hills. *PhD Dissertation, Risø-R-827(EN)*, Risø National Laboratory, Roskilde, Denmark, 1995.

[63] Sørensen NN, Michelsen JA. Aerodynamic predictions for the unsteady aerodynamics experiment phase-II rotor at the National Renewable Energy Laboratory. *AIAA Paper 2000-0037*, 2000.

[64] Sørensen NN, Michelsen JA, Schreck S. Navier-Stokes predictions of the NREL phase-VI rotor in the NASA Ames 80ft x 120 ft wind tunnel. *Wind Energy*, 2002; **5**: 151–169.

[65] Van Bussel GJW. The aerodynamics of horizontal axis wind turbine rotors explored with asymptotic expansion methods. *PhD Dissertation*, Technische Universiteit Delft, The Netherlands, 1995.

[66] Van Holten T. The computation of aerodynamic loads on helicopter blades in forward flight using the method of the acceleration potential. *Report VTH-189*, Technische Universiteit Delft, The Netherlands, 1975.

[67] Van Kuik GAM. On the limitations of the Froude's actuator disc concept. *PhD Dissertation*, Technische Universiteit Eindhoven, 1991.

[68] Voutsinas SG, Belessis MA, Rados KG. Investigation of the yawed operation of wind turbines by means of a vortex particle method. In *Aerodynamics and Aeroacoustics of Rotorcraft*, AGARD-CP-552, 1994; 11.1–11.11.

[69] Wachspress EL. *Iterative solutions of elliptic systems*. Prentice Hall, Englewood Cliffs, New Jersey, 1966

[70] Wilson RE, Lissaman PBS. Applied aerodynamics of wind powered machines. *Report NSF/RA/N-74113*. Oregon State University, 1974.

[71] Wu TY. Flow through a heavily loaded actuator disc. *Schifftechnik*, 1962; **9**: 134–138.

[72] Xu G, Sankar LN. Computational study of horizontal axis wind turbines. *AIAA Paper 99-0042*, 1999.

[73] Øye S. CBEAM4 Beregning af egensvingninger m.v. for centrifugalbelastede bjælker. *Report AFM83-04*, Fluid Mechanics, DTU, 1983.

[74] Øye S. FIX Dynamisk, aeroelastisk beregning af vindmøllevinge. *Report AFM83-08*, Fluid Mechanics, DTU, 1983.

[75] Øye S. Induced velocities for rotors in yaw Proc. 6th IEA Symp. on the *Aerodynamics of Wind Turbines* at ECN, Petten, NL, 1992.

[76] Øye S. Tjæreborg Wind Turbine, structural dynamics data. *AFM-Notat*, Fluid Mechanics, DTU, 1991.

[77] Øye S. Tjæreborg Wind Turbine: Dynamic flow measurement. *AFM Notat VK-233*, Dept. of Fluid Mechanics, Technical University of Denmark, DTU, 1992.

[78] Øye S. Dynamic stall, simulated as time lag of separation. Proc. 4th IEA Symp. on the *Aerodynamics of Wind Turbines* at ENEA Casaccia Research Laboratory, Rome, Italy, Nov. 1990.

Recent Ph.D.-dissertations in Fluid Mechanics

Sørensen, J.N. Three-Level, Viscous-Inviscid Interaction Technique for the Prediction of Separated Flow Past Rotating Wing, AFM 86-03, 1986

Michelsen, J.A. Modelling of Laminar Incompressible Rotating Fluid Flow, AFM 86-05, and Modelling of Turbulent Incompressible Rotating Fluid Flow, AFM 86-07, 1986

Sørensen, L.S. Three-Dimensional Electro-Fluid-Dynamics in Tuft Corona Wire-Plate Precipitators, AFM 89-03, 1989

Gervang, B. Numerical Simulations of 3-Dimensional Flow in Straight and Curved Ducts of Rectangular Cross Section, AFM 89-09, 1989

Andresen, E. Statistical Approach to Continuum Models for Turbulent Gas Particles Flows, AFM 90-04, 1990

Nielsen, N.F. Low Reynolds Number Fluid Dynamics with Applications to Suspending Feeding Animals, AFM 91-10, 1991

Zamany, J. Modelling of Particle Transport in Commercial Electrostatic Precipitators, Ph.D under ATV, EF316, 1992

Christensen, E.A. Laminar-Turbulent Transition in the Rotating Driven Cavity Problem, AFM 93-12, 1993

Trinh, C.M. Turbulence Modelling of Confined Swirling Flows, Risø-R-647,1993

Mayer, K.E. Experimental and Numerical Modelling of Turbulent Flows and Heat Transfer in Staggered Tube Bundles, AFM 94-03, 1994

Mayer, S. Particle Motion in Unsteady Three-Dimensional Flow at Low Reynolds Numbers , AFM 94-04, 1994

Hansen, M.O.L. Vorticity-Velocity Formulation of Navier-Stokes Equations for Aerodynamic Flows, AFM 94-07, 1994

Hvid, S.L. Curvature Based Smoothing of Plane Cubic B-spline Curves, AFM 93-08, Surface Description using Bicubic B-splines, AFM 93-10, QM3D, 3D Netgenerering, Brugermanual, AFM 94-02 and Three-Dimensional Algebraic Grid Generation, AFM 94-08 1993-94

Walther, J.H. Discrete Vortex Method for Two-Dimensional Flow past Bodies of Arbitrary Shape Undergoing Prescribed Rotary and Translational Motion, AFM 94-11, 1994

Nim, E. Energidissipation og Masseoverførsel af Gas i og Omkring Statiske Miksere med Boblestrømning, Ph.D. under ATV, EF410, 1994

Sørensen, N.N. General Purpose Flow Solver Applied to Flow over Hills, Risø-R-827(EN), 1995

Filippone, A. Interaction of Potential Flow Model with the Navier-Stokes Equations for Rotor Aerodynamics, AFM 95-07, 1995

Jensen, E. Optimization of the Electromagnetic Flowmeter, AFM 95-09, 1995

Schmidt, J.J. Experimental and Numerical Investigation of Separated Flows, ET-PHD 97-01 1997

Nygreen, P. A Vorticity-Streamfunction Formulation of the Navier-Stokes Equations for Predicting Unsteady Flow past Bodies in Arbitrary Movement, ET-PHD 97-02, 1997

Sørensen, D.N. Aerodynamic Modelling and Optimization of Axial Fans, ET-PHD 98-01, 1998

Lennart, A.S. Experimental and Theoretical/Numerical Study of Evaporation from Shallow Pools of Organic Liquids, at Simulated Work Conditions, ET-PHD 98-02, 1998

Johansen, J. Unsteady Airfoil Flows with Application to Aeroelastic Stability, Risø-R-1116(EN), 1999

Ullum, U. Imaging Techniques for Planar Velocity and Concentration Measurements, ET-PHD 99-03,1999

Jørgensen, B.H. Low-Dimensional Modelling and Dynamics of the Flow in a Lid Driven Cavity with a Rotating Rod, ET-PHD 2000-02, 2000

Myllerup, L. Turbulence Models for Complex Flows, ET-PHD 2000-03, 2000

Pedersen, N. Experimental Investigation of Flow Structures in a Centrifugal Pump Impeller using Particle Image Velocimetry, ET-PHD 2000-05, 2000

Voigt, L.P.K. Navier-Stokes Simulations of Airflows in Rooms and Around a Human Body, ET-PHD 2001-00, 2001

Gaunaa, M. Unsteady Aerodynamic Forces on NACA 0015 Airfoil in Harmonic Translatory Motion, MEK-FM-PHD 2002-02, 2002

Pedersen, J.M. Analysis of Planar Measurements of Turbulent Flows, MEK-FM-PHD 2003-01, 2003

Mikkelsen, R. Actuator Disc Methods Applied to Wind Turbines, MEK-FM-PHD 2003-02, 2003

Ullum, T.U. Investigation of Turbulence and Flow Structures in Electrostatic Precipitator, MEK-FM-PHD 2003-03, 2003

Hjort, S. Incompressible Boundary Layer Instability and Transition, MEK-FM-PHD 2004-01, 2004